qdjj_solver

Physics manual

Superconducting quantum impurities and quantum-dot Josephson junctions,
static and periodically driven

The qdjj_solver developers

Software version 0.3.0

Development snapshot d0fa801df2b8

Energies in units of the superconducting gap Δ and $\hbar = 1$, unless stated otherwise.
This manual is updated together with the code and describes the features of the version stated above.

Preface

This manual presents the physical models and methods implemented in qdjj_solver. Each method is introduced through its Hamiltonian, governing equations, approximations and physical interpretation. Code examples connect the equations to the public Python interface. They are tested regularly, in the order in which they appear; an example may therefore use variables defined earlier.

Three documents. This physics manual is one of three documents that are kept consistent with each other:

- the *physics manual* explains what is computed and what it means;
- the *user and developer manual*, the Markdown pages in `docs/` (also built as a website), explains how to install the code and how to run, check and save calculations; it lists every option, result field and command-line argument, and describes how to extend the code;
- the *tutorials* in `examples/` are runnable calculations with checked results that accompany the worked examples of Part III.

Each worked example names its tutorial, and the "In the code" boxes name the relevant page of the user manual.

Who should read what. The opening chapters introduce superconducting impurities starting from basic BCS theory and second quantisation. Chapter 2 develops the Andreev-reflection picture and the interpretation of quasiparticle occupations; Chapter 3 introduces the interacting dot. Chapter 4 explains YSR states, Kondo physics and screening, and Chapter 5 connects them to spectroscopy and qubits. Short interpretation exercises accompany the figures. Chapter 6 compares solution methods before describing the two numerical backends. Readers familiar with quantum-dot Josephson junctions can start with the conventions and Chapter 7, which explains how to set up a calculation, assess its accuracy and save the results before introducing periodic driving. Chapter 8 introduces the physics of periodically driven quantum systems and develops Floquet theory from its basic principles. Chapters 9 and 10 explain how drives enter the junction model and how the code computes quasienergies; Chapter 11 explains how a weak probe induces transitions between Floquet states. Part III then builds up the physics step by step. An isolated dot, a driven two-level system, the high-frequency limit and a chapter on numerical convergence come first. They are followed by the phase-driven and the gate-driven junction, two-tone spectroscopy of the pair transition, photon-assisted tunnelling, and electron spin resonance of the Zeeman-split doublet. Chapter 21 maps the equations onto the code, and Appendix A contains the derivations that would interrupt the main text.

Conventions in brief. Energies are in units of the gap Δ and $\hbar = 1$; Ω is then also an energy. The bandwidth parameter is the normal-state *half*-bandwidth D. The hybridization Γ is the *total* hybridization summed over leads. Phases are in radians, and the reference junction carries the phases $\mp\phi/2$ on its left and right leads. Periodic Hamiltonians are expanded as $H(t) = \sum_k H_k \, \mathrm{e}^{\mathrm{i}k\Omega t}$. Table 1.1 on page 4 lists all conventions.

Boxes. Three kinds of boxes appear throughout:

Physical picture

These boxes explain the physical interpretation of a result, using equations where needed.

In the code

These boxes identify the functions, options and result fields associated with a concept.

Caution

These boxes highlight limitations and common numerical or interpretational errors.

Reproducibility. Every figure in Part III is produced by a script in `docs/manual/scripts`. The scripts store the numerical results, together with the code version and numerical environment, in `docs/manual/data`; the figures are then rendered from these records. Section 21.1 explains how to rebuild the figures and this document.

Scope and status. The Floquet part of the code computes quasienergies, harmonic weights and Floquet modes. It also computes the matrix elements of probe operators between static or Floquet states, within one symmetry sector or between sectors, and the resulting spectral lines. Two extensions are planned: the populations of the Floquet states in the presence of dissipation, and a treatment of the continuum beyond the finite bath. The manual is extended together with the code.

Contents

Preface ii

I The model and its static solution 1

1 Introduction 2
- 1.1 Superconducting quantum impurities . . . 2
- 1.2 Why drive the junction? . . . 2
- 1.3 What the package computes . . . 3
- 1.4 A physics-first reading route . . . 3
- 1.5 Conventions . . . 3

2 Andreev reflection and subgap states 5
- 2.1 Three devices, one superconducting environment . . . 5
- 2.2 What is inside the gap? . . . 6
- 2.3 Andreev reflection: exchanging a pair with the condensate . . . 7
- 2.4 One Andreev orbital, four many-body states . . . 8
- 2.5 Why a bound state carries supercurrent . . . 9

3 The model 11
- 3.1 The impurity . . . 11
- 3.2 Superconducting reservoirs . . . 12
- 3.3 Tunnelling, phases and the reference junction . . . 13
- 3.4 Observables and the energy zero . . . 13
- 3.5 Symmetries and sectors . . . 14
- 3.6 Subgap states: singlet and doublet . . . 14
- 3.7 From a parity crossing to Josephson behaviour . . . 17
- 3.8 General impurities and models . . . 18

4 Magnetic impurities, Kondo physics and screening 20
- 4.1 How a dot becomes a magnetic impurity . . . 20
- 4.2 Physical mechanisms of screening . . . 20
- 4.3 Why a superconducting gap competes with Kondo screening . . . 21
- 4.4 The classical Yu–Shiba–Rusinov limit . . . 22
- 4.5 Quantum YSR states and the singlet–doublet transition . . . 23
- 4.6 A residual doublet can have a reduced local spin . . . 25

5 Subgap spectroscopy and Andreev qubits 26
- 5.1 From an eigenstate to a measured signal . . . 26
- 5.2 Superconducting quantum point contacts and atomic contacts . . . 28

5.3 Reading a quantum-dot tunnelling spectrum . . . 28
5.4 The even-parity Andreev-level qubit . . . 29
5.5 The odd-parity Andreev spin qubit . . . 30
5.6 Embedding the junction in a quantum circuit . . . 31
5.7 Lifetimes, poisoning and the limits of a level diagram . . . 32

6 Static solution methods **34**
6.1 Which approximation answers which question? . . . 34
6.2 Canonical coordinates . . . 36
6.3 The quasiparticle expansion . . . 37
6.4 Bath representations . . . 38
6.5 Density-matrix renormalization group . . . 38
6.6 Validation . . . 39

7 From a Hamiltonian to a checked calculation **40**
7.1 State the question and the approximation . . . 40
7.2 A first calculation . . . 40
7.3 Interpret observables and matrix elements . . . 41
7.4 Sweep a parameter and retain the results . . . 41
7.5 Ask three separate convergence questions . . . 42
7.6 Save states and prepare for driving . . . 42

II Periodic driving **44**

8 Floquet theory for periodically driven systems **45**
8.1 Periodic Hamiltonians and the Floquet theorem . . . 45
8.2 Fourier space: the Sambe picture . . . 46
8.3 An exactly solvable example . . . 47
8.4 The photon picture . . . 47
8.5 Gauge freedom and the energy zero . . . 48
8.6 Regimes . . . 48
8.7 Floquet states coupled to a continuum . . . 49
8.8 What is observable . . . 50

9 Driving the junction **51**
9.1 Which parameters can be driven . . . 51
9.2 Phase drive, voltage and the Josephson relation . . . 52
9.3 Harmonics of the phase drive . . . 52
9.4 From laboratory parameters to drive amplitudes . . . 53
9.5 Fixed canonical coordinates . . . 53
9.6 Selection rules . . . 53
9.7 The driven proximitized dot . . . 54

10 Numerical methods for driven problems **55**
10.1 From a drive to harmonics . . . 55
10.2 Sambe-space diagonalization . . . 55
10.3 The one-period propagator . . . 56

10.4 The high-frequency expansion . . . 57
10.5 The rotating-wave model . . . 57
10.6 Choosing a method . . . 58
10.7 Validation . . . 58

11 Probing the driven junction **59**
11.1 The Floquet golden rule . . . 59
11.2 Probes . . . 60
11.3 Initial states, degeneracies and line shapes . . . 60
11.4 Computing the harmonics . . . 61
11.5 Mollow triplet and Autler–Townes doublet . . . 61

III Worked examples **63**

12 Example: the gate-driven isolated dot **64**
12.1 Exact solution . . . 64
12.2 Gauge and the meaning of the charge . . . 65
12.3 Floquet zones and replicas . . . 65
12.4 In the code . . . 65

13 Example: the proximitized dot as a driven two-level system **67**
13.1 Rabi splitting and the rotating-wave approximation . . . 67
13.2 Strong driving and multiphoton resonances . . . 68

14 Example: the high-frequency limit **70**
14.1 Accuracy of the van Vleck expansion . . . 70
14.2 Renormalized coupling and coherent destruction of tunnelling . . . 70

15 Example: numerical convergence **72**
15.1 The Floquet cutoff . . . 72
15.2 The static basis . . . 72
15.3 The discretized continuum . . . 72
15.4 A practical workflow . . . 74

16 Example: the phase-driven junction **75**
16.1 The pair transition . . . 75
16.2 The Floquet spectrum versus frequency and amplitude . . . 75
16.3 The adiabatic limit . . . 76
16.4 Continuum, multiphoton processes and experiments . . . 76

17 Example: the gate-driven junction **79**
17.1 Complementary selection rules . . . 79
17.2 The Floquet spectrum . . . 79
17.3 Two-photon transitions . . . 80

18 Example: two-tone spectroscopy of the pair transition **82**
18.1 Dressed-state lines versus pump detuning . . . 82

18.2 The Mollow triplet . . . 82
18.3 The Autler–Townes doublet . . . 82

19 Example: photon-assisted tunnelling into a driven junction 84
19.1 Tien–Gordon and its generalization . . . 84
19.2 Results . . . 84

20 Example: electron spin resonance of the doublet 86
20.1 The model . . . 86
20.2 Rabi splitting and the effective g-factor . . . 86
20.3 Probing the driven spin . . . 87

IV From equations to code 89

21 From the equations to the code 90
21.1 Reproducing the figures and this manual . . . 91

A Derivations 93
A.1 Harmonics of the phase drive . . . 93
A.2 The residual bound . . . 93
A.3 The high-frequency expansion . . . 93
A.4 The commutator-free Magnus integrator . . . 94

References 95

Part I

The model and its static solution

1 Introduction

1.1 Superconducting quantum impurities

A quantum dot, a molecule or a magnetic adatom coupled to superconductors is the simplest system in which electron–electron interaction, superconducting pairing and quantum coherence compete on an equal footing. The impurity level is described by the Anderson model [1]: a single orbital that can hold zero, one or two electrons, with charging energy U for double occupancy. Coupled to a BCS superconductor, the impurity binds Andreev or Yu–Shiba–Rusinov (YSR) states inside the gap [2–5]. In the simplest spin-symmetric, single-orbital junction, the low-energy competition is between a spin *singlet* and a spin *doublet*. A singlet can arise from proximity pairing or from screening of a local moment; a doublet retains total spin 1/2 even when its dot-local polarization is reduced. Their crossing changes the ground-state fermion parity. In a Josephson junction it is closely associated with the change between 0- and π-junction behaviour, defined by the phase dependence of the ground-state energy and current: the 0–π transition [6–14]. Reviews of the theory and of the experiments are given in Refs. [15–18].

Quantum-dot Josephson junctions have been realized in carbon nanotubes, semiconductor nanowires and two-dimensional heterostructures, and the 0–π transition, the singlet–doublet level crossing and the subgap spectrum have been measured by transport, tunnelling spectroscopy and circuit quantum electrodynamics techniques [19–25]. The same physics governs magnetic adatoms on superconducting surfaces probed by scanning tunnelling microscopy [26–29].

1.2 Why drive the junction?

The subgap states of a junction are the levels of a solid-state artificial atom, and like the levels of an atom they are probed and controlled by oscillating fields. Microwave radiation applied through the phase difference excites pairs of quasiparticles into the Andreev levels of atomic contacts and nanowires [30–34]. The even-parity pair transition is used in Andreev-level qubits; Andreev spin qubits instead use two states within an odd-parity manifold, with spin-dependent control matrix elements [35–40]. Microwave probes also resolve the excitation spectra of interacting quantum-dot junctions [41–45]. Strong periodic driving creates new states, the Floquet–Andreev states observed in graphene junctions [46], and microwave-assisted tunnelling through YSR states has been observed with a scanning tunnelling microscope [47–49]. Periodic driving is, more generally, a tool to engineer effective Hamiltonians, a programme known as Floquet engineering [50–54].

These experiments raise several common questions. How are the many-body subgap states dressed by the drive? Where do resonances occur and how large are the resulting splittings?

Which transitions are allowed by symmetry? How does the interaction modify the answers obtained for non-interacting Andreev levels? Answering them requires the spectrum of the *periodically driven* many-body Hamiltonian, calculated by the Floquet methods in qdjj_solver.

1.3 What the package computes

qdjj_solver treats a finite version of the model: each superconducting reservoir is represented by a finite set of levels chosen to approximate its hybridization function. The static solvers find low-lying many-body eigenstates in each symmetry sector, using either a truncated quasiparticle (QP) expansion or the density-matrix renormalization group (DMRG). Both solvers work with the same Hamiltonian and the same physical conventions.

When parameters are driven periodically, the code computes the *quasienergies* ε_α, the time-periodic *Floquet modes*, their decomposition into harmonics (photon sidebands) and their overlaps with the static eigenstates. Four methods are available: diagonalization in the extended (Sambe) space, the one-period propagator, a high-frequency effective Hamiltonian and a few-level rotating-wave model. Their results agree where their regimes of validity overlap, and the manual uses these comparisons throughout.

1.4 A physics-first reading route

Begin with the device sketches, Andreev trajectories and occupation diagrams in Chapter 2. Then use the four-state dot in Chapter 3 to understand the role of charging energy. Chapter 4 distinguishes proximity pairing from Kondo screening, and Chapter 5 explains which transitions an experiment can detect and how the states can be used as qubits. The first executable calculation is in Section 7.2, after the singlet and doublet states have been defined. Chapter 6 explains the approximations needed to compute them.

1.5 Conventions

Table 1.1: Physical and numerical conventions of qdjj_solver.

Quantity	Convention
Units	Energies use the units of the Hamiltonian parameters, usually with $\Delta = 1$; $\hbar = 1$, so Ω and $1/t$ have energy units
Impurity	$H_d = \frac{U}{2}(n_d - 1)^2 + \epsilon(n_d - 1) + B\, S_d^z$; the detuning $\epsilon = \epsilon_d + U/2$ vanishes at half filling; $B > 0$ raises the spin-up level
Reservoirs	BCS leads with the real pairing term $-\Delta_l \sum_i (c_{li\uparrow}^\dagger c_{li\downarrow}^\dagger + \text{h.c.})$, $\Delta_l > 0$, and normal-state half-bandwidth D; normal-state density of states per spin $\rho = 1/(2D)$
Hybridization	$\Gamma = \sum_l \Gamma_l$ is the total hybridization, $\Gamma_l = \pi\rho\lvert t_l\rvert^2$ with t_l the hopping between the dot and the contact orbital of lead l
Phases	Factors $\mathrm{e}^{\mathrm{i}\phi_l/2}$ on the tunnelling terms $C_{l\sigma}^\dagger d_\sigma$, i.e. the physical pair potential $\Delta_l \mathrm{e}^{-\mathrm{i}\phi_l}$ and the pair amplitude $\langle c_{li\uparrow}^\dagger c_{li\downarrow}^\dagger\rangle \propto \mathrm{e}^{\mathrm{i}\phi_l}$; the reference junction uses $\phi_{L,R} = \mp\phi/2$, $\phi = \phi_R - \phi_L$
Energy zero	The isolated BCS vacuum energies are subtracted: at $\Gamma = 0$ the energies are the atomic energies of H_d, with the reservoirs in their quasiparticle vacuum
Current	$I = (2e/\hbar)\, \partial E/\partial\phi = (2e/\hbar)\langle \partial H/\partial\phi\rangle$, the electric current from the left to the right lead (electron charge $-e$, $e > 0$); reported as $\langle \partial H/\partial\phi\rangle$ in units of Δ
Voltage	$V = V_L - V_R$, the electric potential of the left lead relative to the right one, so $eV = \mu_R - \mu_L$; Josephson relation $\dot\phi = 2eV/\hbar$; IV is the power supplied by the source
Sectors	Fermion parity (0 even, 1 odd), $2S_z$, optional eta parity and particle number
Drives	$p(t) = p_0 + \sum_n A_n \cos(n\Omega t + \theta_n)$; A for a monochromatic drive, A_ϕ (radians) for the phase and A_ϵ (energy) for the detuning
Harmonics	$H(t) = \sum_k H_k \mathrm{e}^{\mathrm{i}k\Omega t}$, $H_{-k} = H_k^\dagger$, time origin $t = 0$
Floquet states	$\psi(t) = \mathrm{e}^{-\mathrm{i}\varepsilon t} \sum_m \mathrm{e}^{\mathrm{i}m\Omega t} u_m$ with quasienergy ε; Sambe matrix $H_{m-m'} + m\Omega\delta_{mm'}$, truncated at the Floquet cutoff $\lvert m\rvert \le M$

2 Andreev reflection and subgap states

2.1 Three devices, one superconducting environment

A superconducting weak link is a small region through which two superconductors exchange electrons and Cooper pairs. Its microscopic structure matters. A clean constriction is described by transmission channels, a confined quantum dot by orbitals and charging energies, and a magnetic adatom by its exchange coupling to the host. All can bind excitations below the superconducting gap, but the mechanism and the appropriate approximations differ. Figure 2.1 compares these devices before we introduce their energy levels.

In a *quantum point contact* (QPC), transverse confinement leaves a few conducting channels. A channel has a normal-state transmission probability $0 \leq \tau_n \leq 1$ and is defined as an eigenmode of the scattering problem. An atomic contact is a particularly short constriction, and even a single atom can support several channels through its valence orbitals. A gate-defined semiconductor QPC allows the channels to be tuned electrostatically. A *quantum dot* instead confines charge sufficiently strongly that the energy cost of adding a second electron must be included explicitly. Its contact transmissions generally depend on energy, occupation and correlations. The distinction is determined by the physical regime and applies across different device materials.

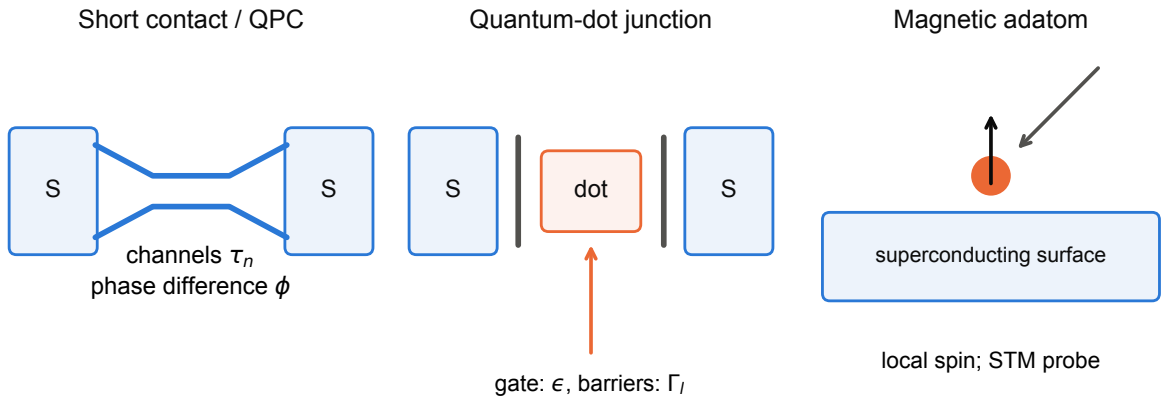


Figure 2.1: Three routes to localized superconducting excitations: a short constriction between superconductors, a gate-controlled dot with tunnel barriers, and a magnetic adatom on a superconducting surface. The arrows identify control or probe couplings; the device sizes and shapes are schematic.

The phase difference $\phi = \phi_R - \phi_L$ controls interference between pair amplitudes. A gate changes the dot energy and often also the tunnel barriers. A magnetic field can split a spin doublet and, in a real device, also affect the superconducting leads. The principal energies are the gap

Δ, charging energy U, total hybridization Γ, detuning ϵ, Zeeman energy B and thermal energy k_BT. Ratios of these scales determine which physical picture is useful. Chapter 3 defines the model parameters precisely; the present chapter develops the non-interacting reference picture.

2.2 What is inside the gap?

Recall that a BCS condensate is a coherent paired state, whereas a Bogoliubov quasiparticle is an excitation above it. For a homogeneous s-wave superconductor, $E_k = \sqrt{\xi_k^2 + \Delta^2}$, so propagating single-quasiparticle excitations begin at Δ. For a constant normal-state density of states ρ_0 per spin, the ideal bulk electron density of states is

$$\rho_{\mathrm{BCS}}(E) = \rho_0 \frac{|E|}{\sqrt{E^2 - \Delta^2}} \Theta(|E| - \Delta). \tag{2.1}$$

Here E is measured from the chemical potential and can be positive or negative because an electron probe can add or remove an electron. The positive quasiparticle excitation energy must be distinguished from this signed probe energy.

A local defect or weak link changes the Hamiltonian and can produce discrete spectral poles inside this bulk gap. Their wavefunctions decay into the leads; they are *bound states*. Thus an ideal hard bulk gap and local subgap peaks are compatible. A soft gap instead describes appreciable spectral background inside the nominal gap, which can have several microscopic origins. A population of nonequilibrium quasiparticles specifies the occupations of the available states.

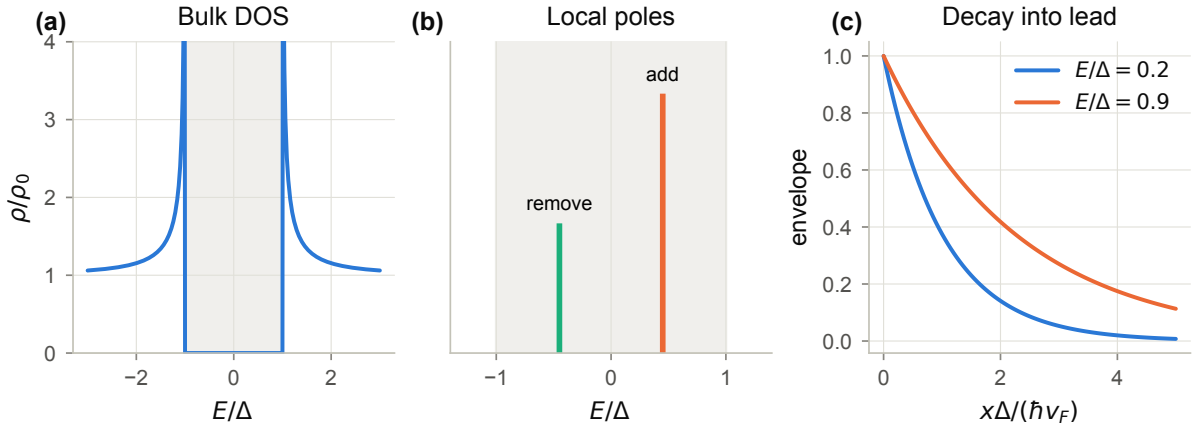


Figure 2.2: (a) Ideal, unbroadened BCS density of states, with the gap edges marked. The plotting range truncates the divergences. (b) Schematic local spectral poles of a bound state, with unequal electron-addition and removal weights, represented by the pole heights. (c) Illustrative decay envelopes: a state nearer the gap edge extends farther into the superconductor.

For a clean lead in the Andreev approximation, an envelope has the characteristic length

$$\xi_E = \frac{\hbar v_F}{\sqrt{\Delta^2 - E^2}}, \qquad |E| < \Delta, \tag{2.2}$$

where v_F is the Fermi velocity. Oscillations on the Fermi-wavelength scale and geometric prefactors are omitted in this envelope picture. A level approaching the gap edge spreads into the reservoir and eventually merges with its continuum. Thus a subgap wavefunction generally extends over both dot and leads. Its dot spectral weight can change substantially while its total normalization remains one.

A gap is a statement about excitations

The condensate can carry a stationary supercurrent without creating a population of quasiparticles. A single bulk quasiparticle costs at least Δ; creating two from an even-parity vacuum costs at least 2Δ. Localized states change the corresponding thresholds. Whenever a diagram shows a shaded continuum, ask which final states and which parity sector it represents.

2.3 Andreev reflection: exchanging a pair with the condensate

Consider an electron incident from a normal region on an ideal transparent normal–superconductor interface, with excitation energy below Δ, the threshold for bulk quasiparticle propagation. It can be reflected as a hole while a Cooper pair is transferred into the condensate. For singlet pairing, the electron and the missing electron represented by the hole have opposite spin. The reflected hole approximately retraces the incident path when the Fermi energy is much larger than Δ and the excitation energy. This is *Andreev reflection*. A barrier also permits ordinary electron reflection; the relative amplitudes are part of the scattering problem.

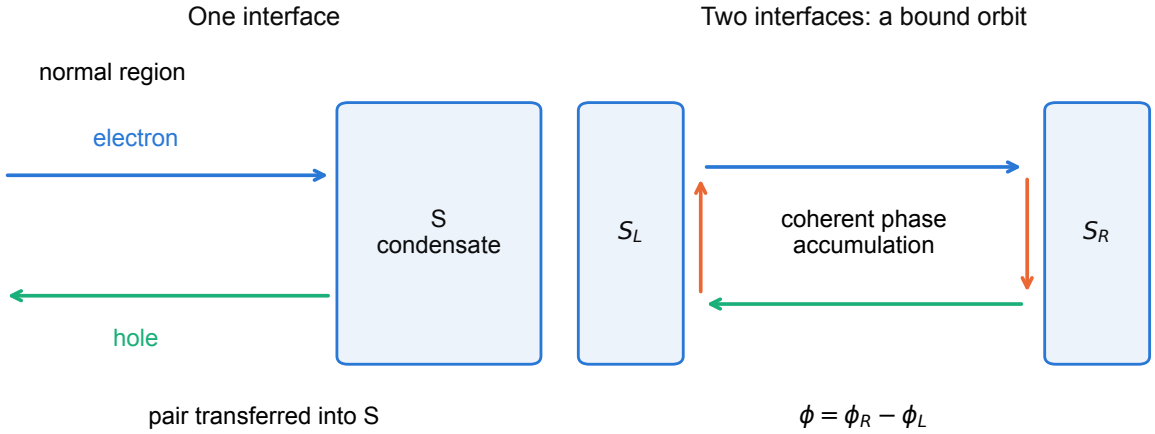


Figure 2.3: Andreev conversion at one interface and an electron–hole round trip between two superconductors. Electron and hole arrows denote group-velocity directions of coherent amplitudes. Pair transfer accompanies conversion; the trajectory describes the phase quantization of coherent electron–hole amplitudes. The short-junction limit neglects the energy-dependent phase accumulated while traversing the normal region.

Two interfaces can confine a coherent electron–hole orbit. Each conversion adds an energy-dependent phase involving $\arccos(E/\Delta)$ and the phase of the condensate. For an ideally transmitting short link, a round trip requires $2\arccos(E/\Delta) = \pm\phi + 2\pi m$ for an integer m,

with the sign distinguishing the two propagation directions. This produces a discrete phase-dependent level. Normal reflection mixes the trajectories. The resulting expression for one spin-degenerate channel is [55, 56]

$$E_A(\phi) = \Delta\sqrt{1 - \tau\sin^2(\phi/2)}, \qquad E_A \geq 0. \tag{2.3}$$

The two leads have equal conventional gaps, the normal scattering matrix is effectively energy independent over that gap, and Coulomb interaction is omitted. The short-junction condition is a dwell-time condition, $\Delta t_{\mathrm{dwell}}/\hbar \ll 1$. Assess it through the dwell time: even a geometrically small dot can have a narrow resonance and a long dwell time.

At zero phase the level reaches the gap edge. Near $\phi = \pi$, increasing transmission lowers its energy; for $\tau < 1$ a finite minimum remains. The zero-energy touching at perfect transmission is sensitive to reflection and occupation. Establishing topological protection or a protected 4π-periodic equilibrium Josephson effect requires additional evidence.

2.4 One Andreev orbital, four many-body states

The Bogoliubov–de Gennes (BdG) equation is a one-particle eigenvalue problem in an enlarged electron–hole space. Its $+E_A$ and $-E_A$ partners describe a particle–hole redundancy of the same physical excitation. After choosing the positive-energy modes, the many-body Hamiltonian of a spin-degenerate Andreev orbital can be written

$$H_A = E_A\left(\gamma_\uparrow^\dagger\gamma_\uparrow + \gamma_\downarrow^\dagger\gamma_\downarrow - 1\right). \tag{2.4}$$

The four Fock states are

$$\begin{aligned} |g\rangle &= |0_A\rangle, & E_g &= -E_A, & P_g &= +1, \\ |o_\sigma\rangle &= \gamma_\sigma^\dagger|0_A\rangle, & E_{o_\sigma} &= 0, & P_{o_\sigma} &= -1, \\ |e\rangle &= \gamma_\uparrow^\dagger\gamma_\downarrow^\dagger|0_A\rangle, & E_e &= +E_A, & P_e &= +1. \end{aligned} \tag{2.5}$$

The notation 0_A counts *bound quasiparticles*, while $|0\rangle$ denotes the empty electron dot. The state $|0_A\rangle$ already includes superconducting pairing and all filled negative-energy electronic states of the reference vacuum.

This elementary example resolves a common apparent discrepancy between experiments. A weak normal tunnel probe can produce resonances at biases $eV = \pm E_A$, whereas a parity-preserving microwave probe can absorb at $hf = 2E_A$. The two probes access different transitions of the same system. The interaction in a quantum dot changes the level spacings and wavefunctions. Calculate each transition from the appropriate many-body energy difference and matrix element of the physical probe operator.

Parity is conserved because pairing changes electron number by two. It remains well defined when particle number itself is not. A state of definite parity can have a non-integer *mean local charge*; its parity follows from the occupied Fock configurations. For a coupled dot and leads, it is the parity of the combined system that labels an eigenstate. Tunnelling produces fluctuations of the dot charge within that state.

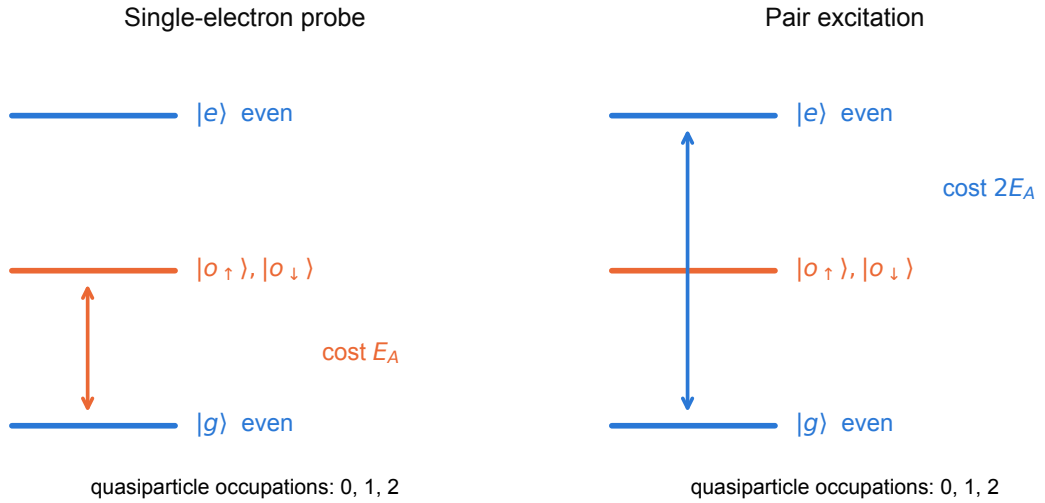


Figure 2.4: Four occupations of a spin-degenerate Andreev orbital. Single-electron addition or removal connects even and odd parity at excitation energy E_A. A pair transition connects the two even states at $2E_A$. The odd states are degenerate here; their splitting in a spin qubit requires additional physics. The arrows indicate transitions allowed by parity; their strengths depend on the matrix elements of the chosen drive.

2.5 Why a bound state carries supercurrent

An energy level that depends on phase contributes a current. For a nondegenerate stationary state, $I = (2e/\hbar)\partial_\phi E$. Applying this relation to the even ground state of Equation (2.4) gives

$$I_g(\phi) = \frac{e\Delta}{2\hbar}\frac{\tau \sin\phi}{\sqrt{1-\tau\sin^2(\phi/2)}}. \tag{2.6}$$

This uses the manual's phase and positive-current convention. The excited even state carries $-I_g$ and either odd state carries zero current in this ideal short-channel model. The two quasiparticles cancel the ground-state contribution one by one. For equal gaps and energy-independent short-junction scattering, the continuum contribution to the equilibrium energy is phase independent. For general dots, long junctions or unequal gaps, include the continuum contribution explicitly.

At small transmission the current is nearly sinusoidal. At high transmission the energy changes rapidly near π, giving a strongly nonsinusoidal current. An excitation changes the occupied many-body branch and hence the current; this provides one method of Andreev-state readout. The current depends on the full phase-dependent energy reference. Differentiating a plotted excitation $E_m - E_g$ gives the current difference $I_m - I_g$.

If all four occupations equilibrate with a reservoir, their partition function is $Z = \mathrm{e}^{\beta E_A} + 2 + \mathrm{e}^{-\beta E_A}$, where $\beta = (k_B T)^{-1}$. The resulting equilibrium current is $I_g \tanh[E_A/(2k_B T)]$. A device trapped in one parity sector samples a restricted ensemble, whose current is obtained by averaging over that sector. Quasiparticle poisoning is the process that switches the bound subsystem between such occupation sectors.

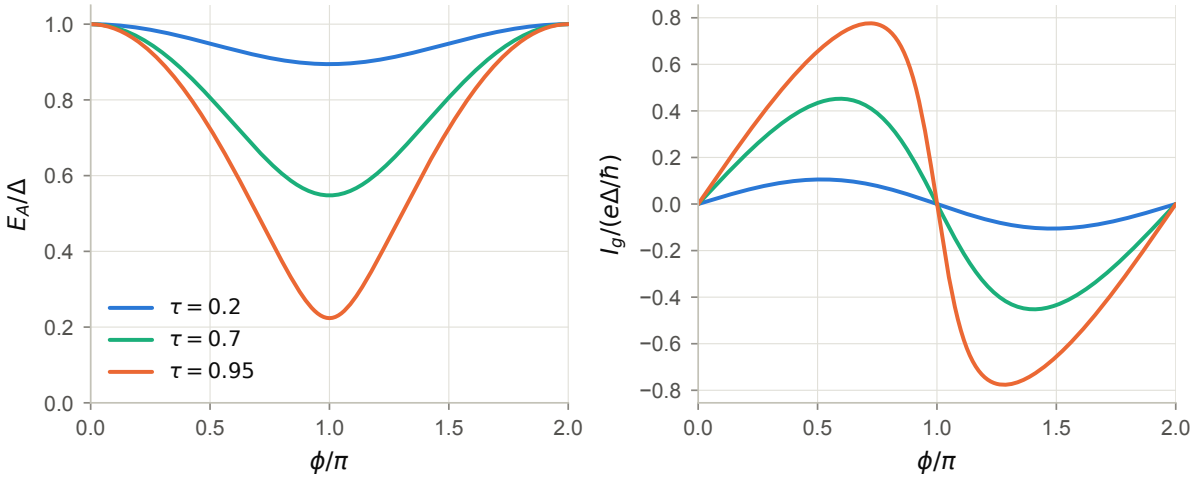


Figure 2.5: Analytic short-channel spectrum and ground-state current for the transmissions indicated. Energy is normalized by Δ and current by $e\Delta/\hbar$. Higher transmission produces a deeper bound state and a more skewed current–phase relation. These curves assume the even ground state at zero temperature and use Equations (2.3) and (2.6).

Read the figures

Suppose a microwave line follows twice the energy of a tunnel-spectroscopy peak. Which two occupations are connected in each experiment? The microwave line can connect $|g\rangle$ to $|e\rangle$; tunnelling connects $|g\rangle$ to $|o_\sigma\rangle$. If one quasiparticle is trapped, the pair transition from $|g\rangle$ loses its initial population, so the line disappears while the bound level can remain inside the gap. The same trapped odd state carries zero current in the ideal model; an interacting dot doublet can carry a finite current.

Reading further. The scattering picture and its connection to quantum dots are reviewed by Martín-Rodero and Levy Yeyati [16]. Aguado's perspective [57] connects the occupation picture to semiconductor superconducting qubits. Glazman and Catelani's lecture notes [58] develop the distinction between the condensate, quasiparticles and circuit degrees of freedom. The following chapter introduces the charging energy that makes the dot a genuinely interacting artificial atom.

3 The model

3.1 The impurity

The impurity is a spin-degenerate orbital with annihilation operators d_σ, $\sigma \in \{\uparrow, \downarrow\}$, occupation $n_d = n_\uparrow + n_\downarrow$ and spin $S_d^z = (n_\uparrow - n_\downarrow)/2$. Its Hamiltonian is written relative to half filling,

$$H_d = \frac{U}{2}\,(n_d - 1)^2 + \epsilon\,(n_d - 1) + B\,S_d^z, \tag{3.1}$$

where U is the charging energy, $\epsilon = \epsilon_d + U/2$ is the detuning from the particle–hole-symmetric point and B is a Zeeman energy that acts on the dot only. In terms of the conventional Anderson parameters, $H_d = \epsilon_d n_d + U n_\uparrow n_\downarrow + B S_d^z + \text{const}$. The four atomic states have the energies

$$E_{|0\rangle} = \frac{U}{2} - \epsilon, \qquad E_{|2\rangle} = \frac{U}{2} + \epsilon, \qquad E_{|\sigma\rangle} = \pm\frac{B}{2}, \tag{3.2}$$

so at $B = 0$ the singly occupied doublet is the atomic ground state when $|\epsilon| < U/2$. Multi-orbital impurities with arbitrary one- and two-body terms are supported as well (Section 3.8).

3.1.1 Charging, gates and the four dot configurations

The four states in Equation (3.2) are labelled by physical *dot-electron occupations*. The Andreev-quasiparticle occupations of Section 2.4 refer to a different basis. The states $|0\rangle$ and $|2\rangle = d_\uparrow^\dagger d_\downarrow^\dagger |0\rangle$ are spin singlets; $|\uparrow\rangle$ and $|\downarrow\rangle$ form a doublet. In the conventional Anderson notation, the first electron-addition energy is ϵ_d and the second is $\epsilon_d + U$. A gate that moves these addition energies through the lead chemical potential changes the preferred charge. The interval $-U < \epsilon_d < 0$, equivalently $|\epsilon| < U/2$, favours one electron on an isolated dot. This is the simplest Coulomb-blockade valley.

Hybridization broadens the charge transitions and mixes dot and lead states. Near a charge degeneracy, empty or doubly occupied configurations have appreciable weight: this is a charge-fluctuating or mixed-valence regime. Well inside a singly occupied valley, with U large relative to the hybridization, charge fluctuations are mainly virtual and the low-energy variable is a spin. Replacing the normal leads by superconductors adds coherent pair exchange and removes their gapless single-particle continuum. These two changes are responsible for much of the physics that follows.

A useful hierarchy of questions

First ask whether the dot would be empty, singly occupied or doubly occupied in isolation. Next compare its charge-excitation energies with the coupling to the leads. Finally ask whether the superconducting gap freezes out lead excitations before strong spin correlations

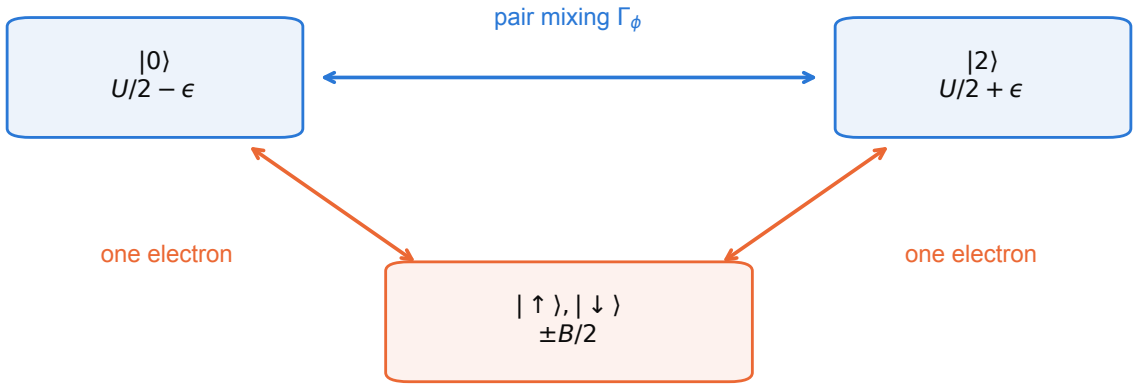


Figure 3.1: Physical electron configurations of a single-orbital dot. Tunnelling visits the singly occupied states by exchanging one electron with a lead. An induced pair amplitude instead couples the two even configurations directly. The energy labels use the shifted convention of Equation (3.1); arrows indicate couplings between configurations.

develop. Identify the regime from the gate setting together with U, Γ and Δ.

3.2 Superconducting reservoirs

Each reservoir l is an s-wave BCS superconductor,

$$H_l = \sum_{i\sigma} \xi_{li}\, c^\dagger_{li\sigma} c_{li\sigma} - \Delta_l \sum_i \left(c^\dagger_{li\uparrow} c^\dagger_{li\downarrow} + c_{li\downarrow} c_{li\uparrow} \right), \tag{3.3}$$

with a real gap $\Delta_l > 0$; the superconducting phase is moved into the tunnelling terms (Section 3.3). The Bogoliubov transformation

$$c_{i\uparrow} = u_i \gamma_{i\uparrow} + v_i \gamma^\dagger_{i\downarrow}, \qquad c_{i\downarrow} = u_i \gamma_{i\downarrow} - v_i \gamma^\dagger_{i\uparrow}, \qquad u_i, v_i = \sqrt{\tfrac{1}{2}(1 \pm \xi_i/E_i)}, \tag{3.4}$$

diagonalizes H_l in terms of quasiparticles with energies $E_i = \sqrt{\xi_i^2 + \Delta_l^2} \geq \Delta_l$: $H_l = \sum_{i\sigma} E_i \gamma^\dagger_{i\sigma} \gamma_{i\sigma} + \sum_i (\xi_i - E_i)$. The last term, the energy of the isolated BCS vacuum, is subtracted from all energies reported by qdjj_solver.

The continuum and its discretization. A real reservoir has a continuum of levels with a flat normal-state density of states $\rho = 1/(2D)$ per spin on $[-D, D]$; D is the *half*-bandwidth. The impurity couples to one combination of reservoir states, the contact orbital

$$C_{l\sigma} = \sum_i \sqrt{w_{li}}\, c_{li\sigma}, \tag{3.5}$$

and the impurity couples to the reservoir through the corresponding hybridization function. A finite bath replaces the continuum by levels ξ_{li} with weights w_{li} that approximate this function

as a quadrature rule. qdjj_solver provides logarithmic (`cosh_grid`), fitted surrogate [59] and Padé chain-expansion [60] representations. The bath and its weights are part of the model and are stored with every result. The continuum is recovered only in the limit of many levels; this limit must be checked separately from all other approximations (Section 6.4 and Chapter 15).

3.3 Tunnelling, phases and the reference junction

The impurity couples to the contact orbitals,

$$H_T = \sum_{l\sigma} \left(\mathrm{e}^{\mathrm{i}\phi_l/2}\, t_l\, C^\dagger_{l\sigma} d_\sigma + \mathrm{h.c.} \right), \qquad \Gamma_l = \pi \rho\, t_l^2, \qquad \Gamma = \sum_l \Gamma_l. \tag{3.6}$$

The phase factor $\mathrm{e}^{\mathrm{i}\phi_l/2}$ carries the superconducting phase ϕ_l of lead l. In the physical gauge the tunnelling amplitudes are real and the pairing term of lead l is $-\Delta_l \sum_i (\mathrm{e}^{-\mathrm{i}\phi_l} c^\dagger_{li\uparrow} c^\dagger_{li\downarrow} + \mathrm{h.c.})$, so that the pair amplitude $\langle c^\dagger_{li\uparrow} c^\dagger_{li\downarrow} \rangle$ is proportional to $\mathrm{e}^{\mathrm{i}\phi_l}$. The substitution $c_{li\sigma} \to \mathrm{e}^{-\mathrm{i}\phi_l/2} c_{li\sigma}$, generated by the unitary $W = \exp(-\mathrm{i} \sum_l \phi_l N_l/2)$ with N_l the electron number of lead l, makes the pair potential real, as in (3.3), and moves the phase into the tunnelling. Only phase differences are physical. Γ denotes the *total* hybridization. Papers often quote the coupling Γ_l per lead instead, which for two identical leads is $\Gamma/2$. A direct interlead hopping W_{LR} between the contact orbitals, with the phase factor $\mathrm{e}^{\mathrm{i}(\phi_L - \phi_R)/2}$, models a parallel conduction channel.

The *reference junction* used throughout this manual consists of a single-orbital impurity, two identical leads with $\Gamma_L = \Gamma_R = \Gamma/2$, phases $\phi_{L,R} = \mp\phi/2$ and no direct hopping. Its parameters, unless stated otherwise, are

$$U = 1, \quad \Gamma = 0.5, \quad \epsilon = 0.2, \quad \phi = 0.8, \quad D = 10, \quad \Delta = 1, \tag{3.7}$$

with a `cosh_grid` bath of four level pairs per lead.

3.4 Observables and the energy zero

The supercurrent follows from the phase dependence of the energy,

$$I = \frac{2e}{\hbar} \frac{\partial E}{\partial \phi} = \frac{2e}{\hbar} \left\langle \frac{\partial H}{\partial \phi} \right\rangle, \tag{3.8}$$

by the Hellmann–Feynman theorem. With $\phi = \phi_R - \phi_L$ and the electron charge $-e$ ($e > 0$), I is the electric current from the left to the right lead: the tunnelling changes the electron number of lead l at the rate $\dot{N}_l = -(2/\hbar)\langle \partial H/\partial \phi_l \rangle$. The operator $\partial H/\partial \phi$ is available as the observable `phase_derivative`. It is reported in units of Δ, so the current is in units of $2e\Delta/\hbar$. Further built-in observables are the impurity charge n_d, the impurity spin S^z_d and the double occupancy $n_\uparrow n_\downarrow$. Because the BCS vacuum energies are subtracted, energies at $\Gamma = 0$ are the atomic energies (3.2).

The local orbital density matrix resolves occupations and pairing coherences. In the ordered basis $|0\rangle, |\uparrow\rangle, |\downarrow\rangle, |2\rangle$, with $|2\rangle = d^\dagger_\uparrow d^\dagger_\downarrow |0\rangle$, its entries are $\rho_{ab} = \langle |b\rangle\langle a| \rangle$. Fixed total parity removes local odd–even coherences, while $\rho_{30} = \langle d_\downarrow d_\uparrow \rangle = F$ can remain finite. Writing $P_a = \rho_{aa}$ gives

$\langle n_d \rangle = P_\uparrow + P_\downarrow + 2P_2$ and probabilities $(P_0 + P_2)/2 \pm \mathrm{Re}\, F$ for the normalized local states $(|0\rangle \pm |2\rangle)/\sqrt{2}$. Their sum is the local even weight. Thus unit mean occupation can describe either a local spin or coherent pair mixing. `orbital_density_matrix` evaluates these operators in physical electron coordinates for QP or DMRG states; `orbital_density_properties` also returns the purity $\mathrm{Tr}\,\rho^2$. Equal incoherent weighting of a complete degenerate eigenspace gives a basis-independent density matrix. User manual: *Using the solver and saving results* (`docs/interfaces.md`) gives the measurement and mixture arguments.

3.5 Symmetries and sectors

The Hamiltonian conserves the fermion parity $P = (-1)^N$: pairing changes the electron number by two. Without transverse fields or spin–orbit coupling it also conserves the total spin projection S_z, and at $B = 0$ it is SU(2) symmetric. Calculations are performed in a *sector* of fixed parity and, optionally, fixed $2S_z$ (`Sector(parity, twice_sz)`). For the symmetric junction at the particle–hole-symmetric point ($\epsilon = 0$, no normal interlead hopping) there is an additional $\mathbb{Z}_2$ symmetry of particle–hole type. It is diagonal in the eta representation (`reference_model(symmetry=True)` at $\epsilon = 0$), and its eigenvalue, the *eta parity* $\eta = \pm 1$, can be used as a further quantum number. Tunnelling, pairing, U and the phase dependence are eta-even, whereas $n_d - 1$ is eta-odd, so a detuning breaks the symmetry. In Section 9.6 this distinction becomes a selection rule for driven transitions.

Caution

At exact degeneracies the eigenvectors can be rotated within their common eigenspace. Expectation values of non-conserved operators then depend on the basis chosen within the degenerate subspace; compare complete multiplets, or resolve them by additional quantum numbers.

3.6 Subgap states: singlet and doublet

Atomic limit. For $\Gamma \to 0$ the dot decouples. The spectrum consists of the atomic energies (3.2) plus quasiparticle excitations of the leads, each costing at least Δ. Even parity contains $|0\rangle$ and $|2\rangle$, odd parity the doublet $|\sigma\rangle$.

Large-gap (proximitized-dot) limit. In the wide-band limit, when Δ exceeds the dot and hybridization scales, virtual Cooper-pair tunnelling induces a local pairing on the dot. Eliminating the leads gives the effective Hamiltonian H_∞ of the infinite-gap limit [13, 14, 61]

$$H_\infty = H_d - \left(\Gamma_\phi\, d_\uparrow^\dagger d_\downarrow^\dagger + \Gamma_\phi^*\, d_\downarrow d_\uparrow\right), \qquad \Gamma_\phi = \sum_l \Gamma_l \mathrm{e}^{-\mathrm{i}\phi_l} = \Gamma \cos\frac{\phi}{2}, \tag{3.9}$$

the last equality for the symmetric junction. The doublet is unaffected, $E_D = \pm B/2$, while $|0\rangle$ and $|2\rangle$ hybridize into two singlets,

$$E_{S,S^*} = \frac{U}{2} \mp \sqrt{\epsilon^2 + |\Gamma_\phi|^2}. \tag{3.10}$$

The even subspace is therefore a two-level system with the pseudospin Hamiltonian $\frac{U}{2} + \epsilon\tau_z - |\Gamma_\phi|\tau_x$, where $\tau_z = \pm 1$ for $|2\rangle$ and $|0\rangle$. At $B = 0$ the ground state is a singlet when $\sqrt{\epsilon^2 + |\Gamma_\phi|^2} > U/2$ and a doublet otherwise; the phase dependence of Γ_ϕ drives the transition. This two-level system reappears in Chapter 13 as the simplest driven model.

3.6.1 Diagonalizing the even sector by hand

In the ordered electron basis $(|0\rangle, |2\rangle)$, the even block is

$$H_{\text{even}} = \begin{pmatrix} U/2 - \epsilon & -\Gamma_\phi^* \\ -\Gamma_\phi & U/2 + \epsilon \end{pmatrix}. \tag{3.11}$$

Its diagonal entries cross when $\epsilon = 0$, but pair mixing turns that crossing into an avoided crossing of size $2|\Gamma_\phi|$. The lower eigenstate is a coherent superposition of empty and doubly occupied dot configurations. For $R = \sqrt{\epsilon^2 + |\Gamma_\phi|^2} > 0$, its charge follows either from its wavefunction or from the Hellmann–Feynman theorem:

$$\langle n_d \rangle_S - 1 = \frac{\partial E_S}{\partial \epsilon} = -\frac{\epsilon}{R}. \tag{3.12}$$

At half filling it has mean dot charge one despite containing only empty and doubly occupied configurations in this limit. This is a direct example of even parity with odd mean charge.

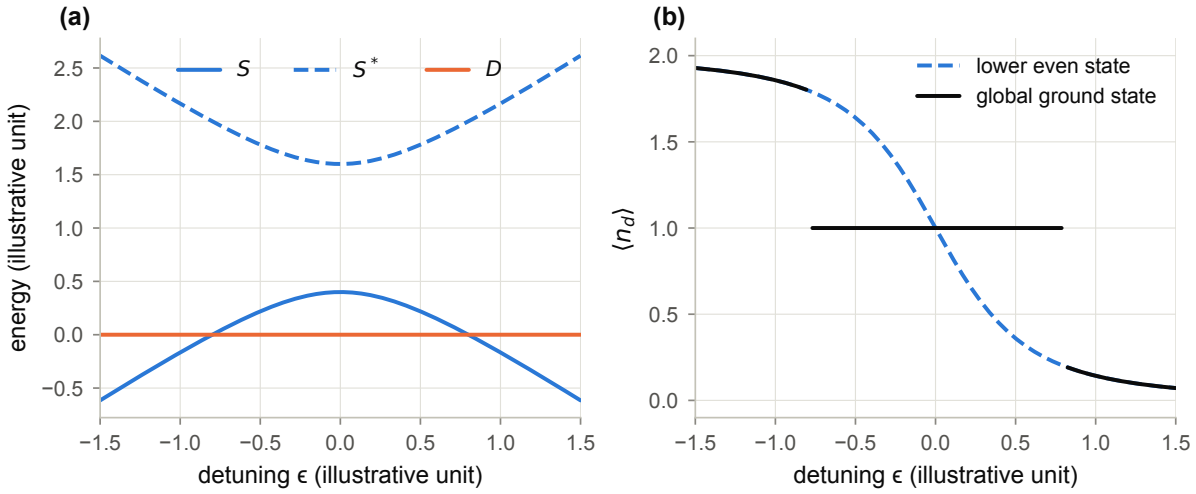


Figure 3.2: Large-gap dot with $U = 2$ and $|\Gamma_\phi| = 0.6$ in a common illustrative energy unit. (a) The even singlets avoid crossing each other; the lower singlet crosses the uncoupled odd doublet. (b) Its mean charge and the global ground-state charge. These curves describe the infinite-gap effective dot. The finite-gap reference junction is defined separately in Equation (3.7).

At zero field, a parity transition occurs at $R = U/2$. At fixed $|\Gamma_\phi| < U/2$, a gate sweep crosses this boundary twice, leaving a doublet region around half filling. Increasing $|\Gamma_\phi|$ eventually removes that region. For two leads,

$$|\Gamma_\phi|^2 = \Gamma_L^2 + \Gamma_R^2 + 2\Gamma_L\Gamma_R \cos\phi. \tag{3.13}$$

Pair exchange is strongest when the condensate contributions add, and weakest when they oppose each other. Exact cancellation at $\phi = \pi$ requires equal couplings. The even states repel because pairing couples them; a singlet and doublet cross because their parities differ.

The wide-band qualification is important when using a finite-band solver. For a flat band of half-width D, a lead's zero-energy anomalous contribution has magnitude

$$\Gamma_{l,\mathrm{ind}} = \frac{2\Gamma_l}{\pi} \arctan \frac{D}{\Delta}. \tag{3.14}$$

This follows by integrating $\Gamma_l \Delta/[\pi(\xi^2 + \Delta^2)]$ over $[-D, D]$. Taking $D \gg \Delta$ first recovers Γ_l. Sending Δ to infinity at fixed D instead suppresses this contribution. Obtaining the conventional atomic pairing model therefore requires the wide-band limit first. Replacing each lead by one paired site defines a separate finite-reservoir approximation.

3.6.2 Finite gap and Kondo correlations

For Δ comparable to U and Γ, quasiparticle states of the leads contribute to the bound states. In the strongly interacting regime, Kondo screening, characterized by the normal-state Kondo temperature T_K, competes with the gap. In the local-moment regime, $k_B T_K \gg \Delta$ favours a screened singlet and $k_B T_K \ll \Delta$ a doublet; the boundary depends on conventions, phase and other parameters [10–12, 14]. Chapter 4 develops this competition and distinguishes it from local pairing. Besides S and D, an excited singlet S^* can lie inside the gap. The continuum starts one quasiparticle above the ground state, at $E_{\mathrm{ground}} + \Delta$, when all parity sectors are considered in the continuum limit. In a fixed sector, the lowest allowed threshold can be higher: a singlet plus one quasiparticle has odd parity, whereas a doublet plus one quasiparticle can have even parity. For example, the even breakup threshold on the singlet side can be $E_D + \Delta$, corresponding to a doublet plus one lead quasiparticle. A finite bath replaces continua by discrete levels; the shading below indicates the continuum-limit lower envelope.

Table 3.1: Subgap states of the reference junction and their quantum numbers.

State	Parity	Spin	S_z sectors	Character
S	even	0	0	bonding combination of $\|0\rangle$, $\|2\rangle$ and lead quasiparticles; ground state at $\phi = 0.8$
S^*	even	0	0	antibonding partner of S; reached from S by the pair transition
$D_{\uparrow,\downarrow}$	odd	$\frac{1}{2}$	$\pm\frac{1}{2}$	local moment, partially screened; split by B
continuum	both			ground state plus at least one quasiparticle, energy $\geq E_{\mathrm{ground}} + \Delta$

Figure 3.3 shows the subgap spectrum of the reference junction. At $\phi = 0.8$ and $\epsilon = 0.2$ the singlet S is the ground state, the doublet lies $E_D - E_S = 0.096$ above it, and the excited singlet lies at $E_{S^*} - E_S = 0.716$, well below the continuum. The S–S^* pair transition and the doublet are the main subjects of the driven examples.

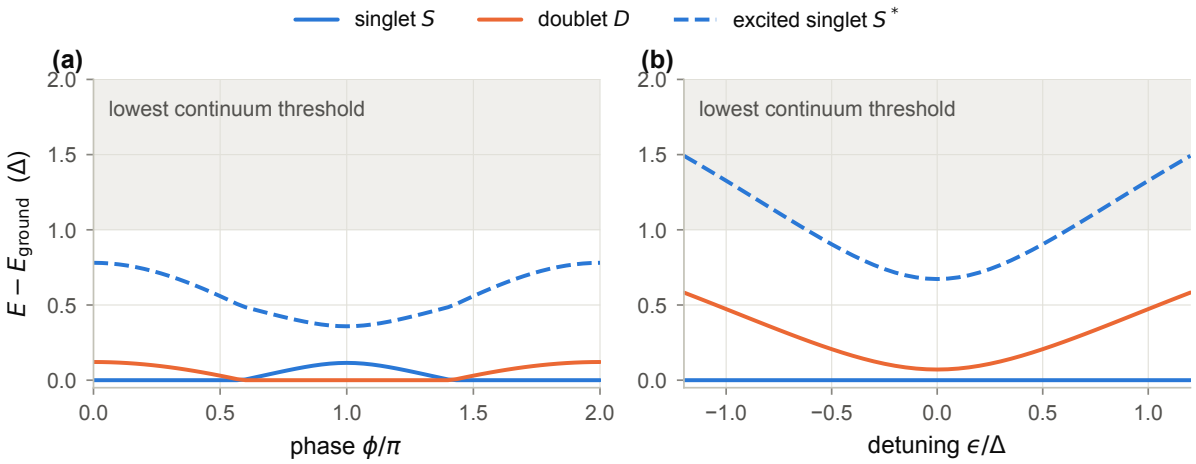


Figure 3.3: Subgap spectrum of the reference junction (3.7), measured from the ground state: (a) versus the phase at $\epsilon = 0.2$, (b) versus the detuning at $\phi = 0.8$. The doublet becomes the ground state near $\phi = \pi$, where $|\Gamma_\phi|$ is smallest. The shaded region marks the lowest continuum threshold across parity sectors, Δ above the ground state. Each probe's threshold follows from its allowed final sector. QP cutoff 2, four bath level pairs per lead.

Physical picture

The singlet ground state is a coherent superposition of the empty and doubly occupied dot (and, at finite Δ, of states with quasiparticles in the leads), held together by the induced pairing Γ_ϕ. The excited singlet S^* is the antibonding partner of the same pair. The transition $S \to S^*$ changes the charge distribution while preserving parity, so a gate or a phase drive can excite it when the matrix element is nonzero. The doublet carries total spin 1/2 and is reached only by changing the parity, that is, by adding or removing a quasiparticle.

3.7 From a parity crossing to Josephson behaviour

At zero temperature, the global ground-state energy is the lowest energy across all relevant sectors. A 0 junction has its equilibrium energy minimum at phase zero; a π junction has its minimum at π. For an approximately sinusoidal current, these correspond to positive and negative coefficients of $\sin\phi$. These definitions classify the full phase dependence of the energy.

In the usual single-level superconducting Anderson model, the singlet branch tends to favour 0 behaviour and the doublet branch π behaviour. Virtual finite-gap tunnelling processes through a local moment can reverse the pair transfer amplitude [6, 7]. The strict large-gap model instead has a phase-independent doublet energy and therefore zero doublet current. It demonstrates the parity crossing; reproducing the finite-gap π current requires the virtual processes described above.

If the ground-state parity changes as the phase is varied, the ground-state current is piecewise defined. Both zero and π can be local energy minima in intermediate regimes, conventionally

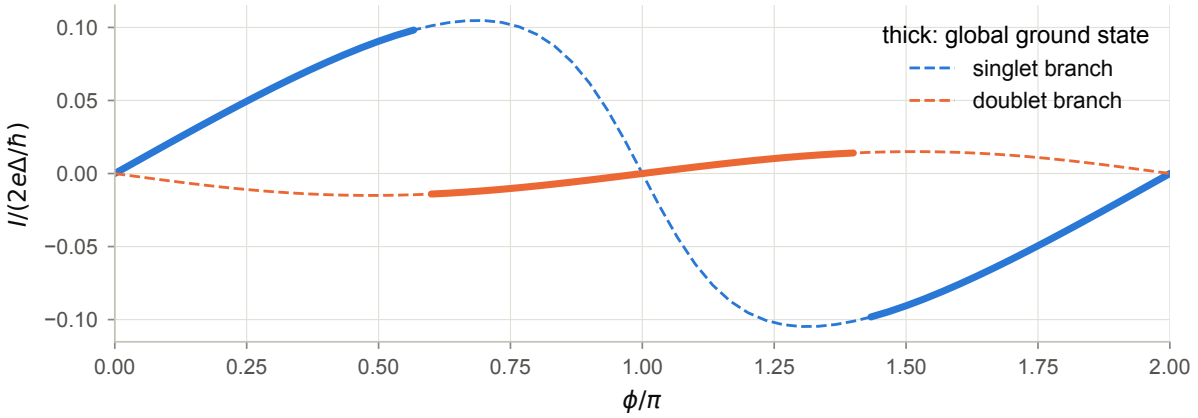


Figure 3.4: State-resolved and global ground-state currents of the finite-bath reference junction, rendered from the same calculation as Figure 3.3. Current is in units of $2e\Delta/\hbar$. The global ground state follows the singlet or doublet branch with lower energy; disconnected segments indicate parity changes, where a unique zero-temperature derivative need not exist. The finite-gap doublet current is distinct from its zero value in the strict large-gap model. Bath and QP truncations are those of Figure 3.3.

called $0'$ or π' according to the global minimum. Multilevel structure, spin–orbit coupling and magnetic fields admit further possibilities. Thus "even means 0" and "odd means π" are useful associations for that single-level model. Classify a general weak link by the phase dependence of its ground-state energy.

At finite temperature and with equilibrium exchange between sectors, use the free energy $F = -k_B T \ln \sum_m \exp[-E_m/(k_B T)]$ and $I = (2e/\hbar)\partial_\phi F$. If parity remains trapped during the experiment, restrict the state sum accordingly. A state-resolved current, a zero-temperature ground-state current and a thermally averaged current are three different observables even for the same Hamiltonian.

Read the atomic-dot plot

At half filling, the lower even state in Figure 3.2 has mean charge one. Which electron configurations produce this mean charge? The state is an even superposition of zero and two dot electrons. Why can it cross the doublet? The two states have different parity. What produces a doublet supercurrent at finite gap? Virtual tunnelling processes generate the phase dependence retained in Figure 3.4.

Chapter 7 turns this model into a complete calculation, including sector comparison, observables, transitions, numerical checks and saved results.

3.8 General impurities and models

`make_model` builds models with several reservoirs, arbitrary tunnelling matrices T_l (including spin mixing), interlead hopping and multi-orbital impurities, specified either by one- and two-body integrals or directly as fermionic operators. The reference junction is the special case built

by `reference_model`. Any Hermitian, parity-conserving fermionic operator (`FermionOperator`) can be turned into a `Hamiltonian` and solved; the examples in Chapters 13 and 20 use this freedom.

Tutorial: *Subgap states, singlet and doublet* (`examples/01_subgap_states`).

4 Magnetic impurities, Kondo physics and screening

4.1 How a dot becomes a magnetic impurity

In the local-moment regime, removing the dot's electron or adding a second one requires much more energy than the thermal and dynamical energy scales of interest. Charge fluctuations are suppressed, but the orientation of the remaining spin can still fluctuate. This is the starting point for quantum magnetism in a single impurity. An odd electron occupation supplies a spin even in a dot made from nonmagnetic materials.

Consider first normal leads. A lead electron can tunnel onto the dot, visit the doubly occupied configuration virtually, and tunnel back with a different spin. A second sequence visits the empty configuration. Eliminating these high-energy intermediate states gives an antiferromagnetic exchange Hamiltonian. For a single effective normal conduction channel with tunnelling amplitude t,

$$H_K = J\boldsymbol{S}_d \cdot \boldsymbol{s}(0) + H_{\text{lead}}, \qquad J = 2|t|^2\left(\frac{1}{-\epsilon_d} + \frac{1}{\epsilon_d + U}\right) > 0. \tag{4.1}$$

Here $\epsilon_d < 0 < \epsilon_d + U$, $\boldsymbol{s}(0) = \frac{1}{2}\sum_{\sigma\sigma'} c^\dagger_\sigma \boldsymbol{\sigma}_{\sigma\sigma'} c_{\sigma'}$ is the spin density of the coupled conduction orbital, and $\boldsymbol{\sigma}$ denotes the Pauli matrices. There is also potential scattering, which vanishes at the particle–hole-symmetric point. This low-energy reduction assumes well-separated charge excitations. In the mixed-valence regime, retain charge fluctuations explicitly. The normal-state effective channel is a coherent combination of the two physical leads [62, 63].

Antiferromagnetic exchange favours antiparallel correlations. Its spin-flip part, $J(S_d^+ s^- + S_d^- s^+)/2$, allows the bath and impurity to exchange angular momentum. Repeated virtual processes at progressively lower energies strengthen the effective coupling. At the *Kondo temperature* T_K, a weak-exchange description fails and the low-energy state becomes strongly correlated. For a spin-1/2 impurity with one screening channel and a metallic bath, the zero-temperature ground state is a singlet. This is Kondo screening.

4.2 Physical mechanisms of screening

The word screening is used for several different physical processes. Ordinary electrostatic screening rearranges charge around a perturbing electric potential. Kondo screening involves quantum *spin* correlations. Proximity pairing mixes different even-charge configurations through exchange of Cooper pairs. Figure 4.1 distinguishes these mechanisms.

The two-spin singlet

$$|\text{singlet}\rangle = \frac{|{\uparrow_d}{\downarrow_b}\rangle - |{\downarrow_d}{\uparrow_b}\rangle}{\sqrt{2}} \tag{4.2}$$

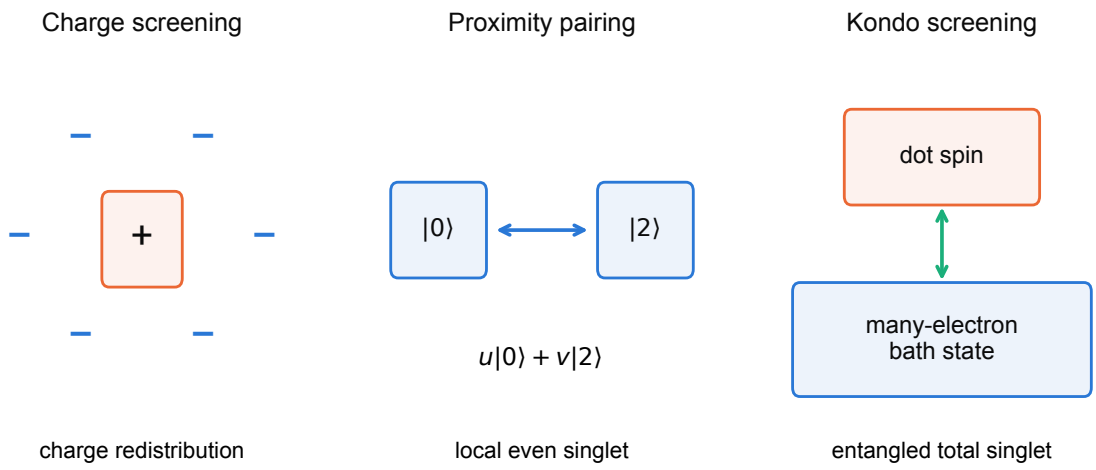


Figure 4.1: Three distinct physical mechanisms. Electrostatic screening rearranges charge; proximity pairing coherently mixes the empty and doubly occupied dot; Kondo screening entangles a local moment with conduction electrons. The screening cloud schematically represents correlations with many conduction electrons.

is a useful illustration of entanglement. Its total spin is zero, each local spin has zero mean polarization, but each has $\langle \boldsymbol{S}_d^2 \rangle = 3/4$ and $\langle \boldsymbol{S}_d \cdot \boldsymbol{S}_b \rangle = -3/4$: the local moments remain finite and are antiferromagnetically correlated. This two-spin wavefunction illustrates the entanglement. In the full Kondo problem the bath partner is a many-electron state distributed across energies and positions. A normal-metal correlation length is of order $\xi_K \sim \hbar v_F/(k_B T_K)$, with its precise definition depending on the correlation being measured.

A singlet in a proximitized dot can instead take the form $u|0\rangle + v|2\rangle$. In the strict large-gap model it contains exclusively empty and doubly occupied configurations. Both states have total spin zero, but only the first picture screens a pre-existing local moment. At finite gap and finite hybridization these descriptions can evolve smoothly into one another because they share the same symmetries, allowing a crossover between pairing-dominated and Kondo-dominated singlet regimes.

Which observable establishes screening?

To identify the screening mechanism, examine the dot charge distribution, $\langle \boldsymbol{S}_d^2 \rangle$, spin correlations with the bath, the temperature dependence of the susceptibility, and the normal-state Kondo scale. These distinguish a local moment, its screening and a predominantly empty/doubly occupied proximity singlet. Zero local magnetization, $\langle S_d^z \rangle = 0$, is compatible with all of these and with an unpolarized ensemble of free spins; a total-spin label $S = 0$ likewise leaves the mechanism to be identified.

4.3 Why a superconducting gap competes with Kondo screening

The Kondo effect draws on low-energy electron–hole excitations of a normal metal. A superconducting gap removes the gapless continuum on which this low-energy buildup relies. In

the local-moment regime the useful comparison is therefore between $k_B T_K$, defined for the corresponding *normal-state* impurity, and Δ [10–12].

When $k_B T_K \gg \Delta$, correlations have become strong before the gap cuts off the normal-metal flow. A screened singlet is favoured. When $k_B T_K \ll \Delta$, the gap interrupts that flow before screening is complete, and a doublet is favoured. When the two scales are comparable, locating the transition accurately requires an explicit solution of the superconducting impurity problem.

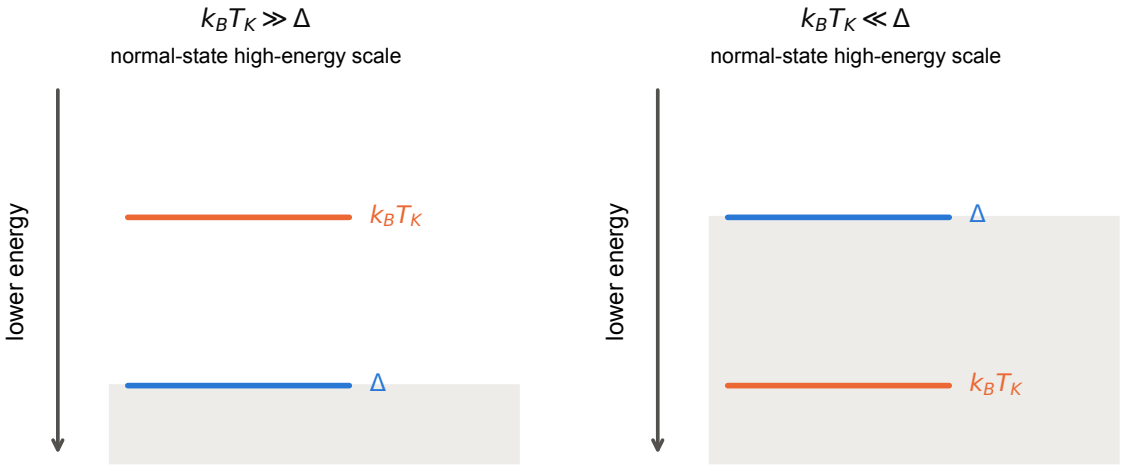


Figure 4.2: Schematic energy-scale comparison in the local-moment regime. Following the normal-state flow downwards, strong Kondo correlations are reached before the gap in the left panel, whereas the gap intervenes first in the right panel. Positions on these logarithmic energy scales illustrate the two limiting regimes. The shaded regions denote energies unavailable as bulk single-QP excitations.

The Kondo scale is exponentially sensitive to microscopic parameters. Definitions from susceptibility, a spectral width and transport fits differ by numerical factors. Total and per-lead definitions of Γ introduce another common conversion. Consequently, a quoted critical value of T_K/Δ is meaningful only with its scale convention, phase, asymmetry and Hamiltonian specified. This manual writes $k_B T_K/\Delta$ when the Kondo scale is expressed as a temperature; setting $k_B = 1$ converts it to an energy. Determine the transition boundary for the specified junction and conventions.

Phase matters even at fixed normal-state T_K. Contributions from the two condensates interfere, and their cancellation near $\phi = \pi$ can destabilize a singlet. Detuning can remove the local moment entirely. Thus a diagram with axes T_K and Δ summarizes one competition, while gate–phase diagrams often describe experiments more directly. Emptying the dot produces a singlet through a change of charge configuration, with the local moment removed.

4.4 The classical Yu–Shiba–Rusinov limit

A different instructive limit replaces the impurity by a prescribed classical spin $\boldsymbol{S}$, with no quantum spin flips. Magnetic scattering affects the two members of a Cooper pair differently

and binds a localized state. In a particle–hole-symmetric, wide-band s-wave host, with no potential scattering, one signed YSR pole can be written [2–5]

$$E_{\mathrm{YSR}} = \Delta \frac{1-\alpha^2}{1+\alpha^2}, \qquad \alpha = \frac{\pi \rho_0 J S}{2}. \tag{4.3}$$

Here ρ_0 is the normal density of states per spin and the exchange is $J\boldsymbol{S}\cdot c^\dagger \boldsymbol{\sigma} c/2$; these conventions fix the factor of two. The particle–hole partner has the opposite pole energy. Potential scattering changes the formula and the electron/hole weights.

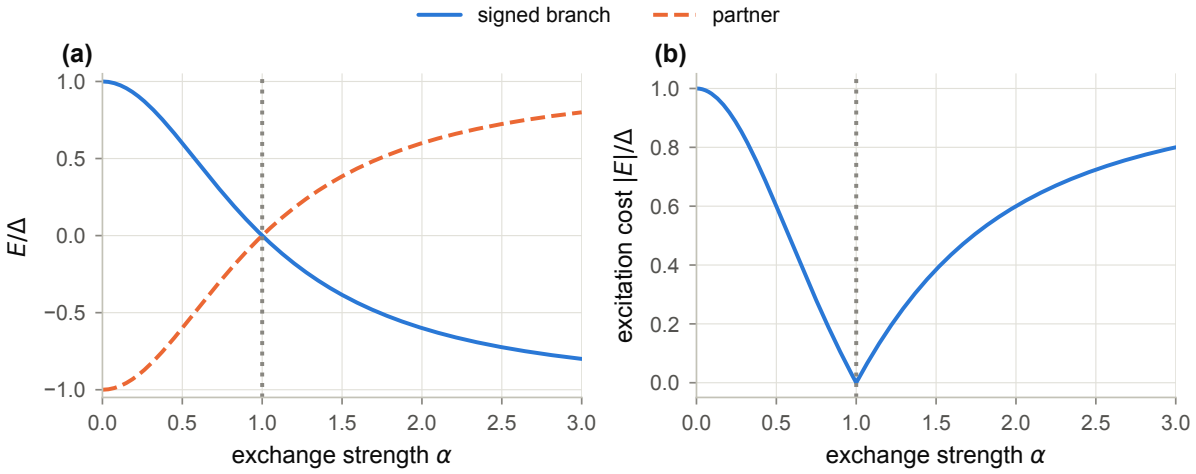


Figure 4.3: Classical-spin YSR poles from Equation (4.3). (a) Following a signed branch through zero and its particle–hole partner. (b) The positive excitation cost $|E_{\mathrm{YSR}}|$. The change of sign changes the reference occupation while the excitation cost remains nonnegative. These curves describe scattering from a prescribed classical spin.

Starting at weak exchange, the pole leaves the gap edge and moves towards zero. At $\alpha = 1$ its sign changes, requiring a change in the occupation defining the many-body ground state. Excitations above that ground state cost $|E_{\mathrm{YSR}}|$. The binding energy below the continuum edge is the separate quantity $\Delta - |E_{\mathrm{YSR}}|$.

The classical model explains localized impurity states and a parity-changing crossing within a simple analytical description based on static magnetic scattering. Describing the Kondo effect requires quantum impurity-spin dynamics. When a quantum-dot spectrum resembles the classical curve, examine its many-body wavefunctions and spin correlations to identify the screening mechanism.

4.5 Quantum YSR states and the singlet–doublet transition

For a quantum impurity, diagonalization produces many-body states of the *dot plus superconducting leads*. In the spin-rotation-invariant, single-orbital problem, the relevant low states are usually an even singlet S and an odd doublet D. An electron probe connects them. Define the signed energy difference

$$\delta_{SD} = E_D - E_S. \tag{4.4}$$

The singlet is the ground state for $\delta_{SD} > 0$, and the doublet for $\delta_{SD} < 0$. The lowest transition between them costs $|\delta_{SD}|$; positive and negative bias probe electron addition and removal, with generally different weights. A branch crossing through zero in a plot of δ_{SD} and two resonances meeting at zero bias are related representations of the same singlet–doublet transition.

Parity conservation keeps the even and odd sectors decoupled, allowing their levels to cross exactly. Coupled states of the same symmetry instead form an avoided crossing. At zero temperature the parity crossing changes the global ground state. A closed, isolated system retains its initially prepared parity as a parameter is varied through the crossing. Relaxation to the new global ground state requires a channel for parity exchange with the surroundings.

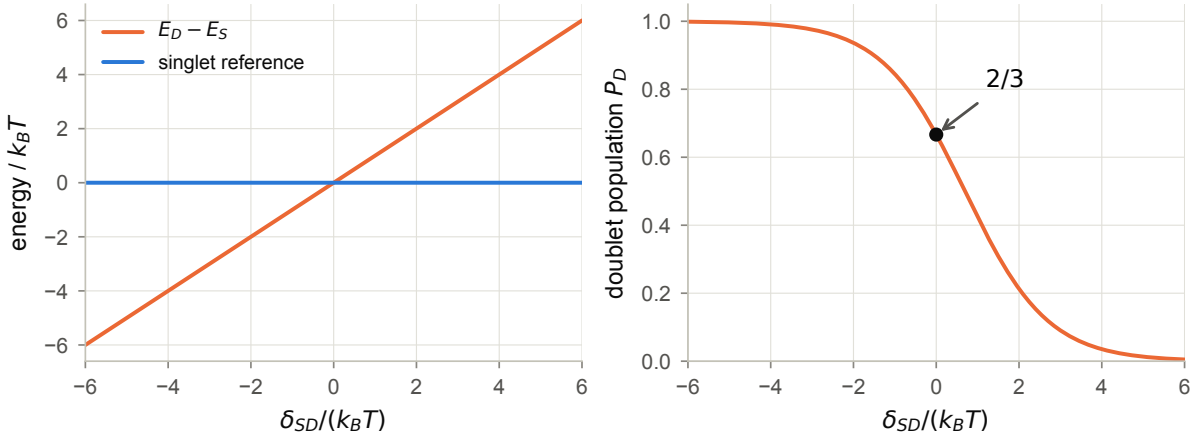


Figure 4.4: Ground-state competition and thermal occupation of a singlet and a spin-degenerate doublet. The horizontal coordinate is the actual energy difference δ_{SD} in units of k_BT. The doublet probability assumes equilibrium between both parities and no other thermally occupied states. Thermal rounding changes the populations while the Hamiltonian eigenvalues retain their exact crossing.

At temperatures low enough that only these multiplets are appreciably populated, equilibrium gives

$$Z = \mathrm{e}^{-\beta E_S} + 2\mathrm{e}^{-\beta E_D}, \qquad P_D = \frac{2\mathrm{e}^{-\beta\delta_{SD}}}{1 + 2\mathrm{e}^{-\beta\delta_{SD}}}. \tag{4.5}$$

The factor two is the doublet degeneracy. At equal energies the doublet has probability 2/3. A magnetic field splits the two Boltzmann weights; a parity-trapped experiment instead needs a restricted population model. The parity crossing remains exact as temperature changes the populations and spectral broadening changes the displayed line shapes.

In this setting, *Andreev bound state* is often used broadly for a subgap excitation of a superconducting weak link, while *YSR state* emphasizes its magnetic-impurity origin. For an interacting quantum dot these names often refer to the same measured spectral features. We specify the state, transition and approximation to make the physical interpretation explicit. A useful short introduction to this many-body interpretation is Ref. [64]; the wider theory is reviewed in Refs. [16, 17].

4.6 A residual doublet can have a reduced local spin

A doublet has total spin 1/2, distributed between dot and leads. For its $S_z = +1/2$ component,

$$\langle S_d^z \rangle + \langle S_{\text{leads}}^z \rangle = \frac{1}{2}. \tag{4.6}$$

Hybridization changes the local charge fluctuations and dot–lead correlations, redistributing this polarization. Calling a doublet "partially screened" describes this local reduction while the conserved total spin remains 1/2.

If a weak field acts only on the dot as BS_d^z, the Hellmann–Feynman theorem relates the linear splitting to the local polarization. In an SU(2)-symmetric zero-field doublet,

$$\lim_{B\to 0} \frac{|E_{D\uparrow} - E_{D\downarrow}|}{|B|} = 2|\langle D\uparrow|S_d^z|D\uparrow\rangle|. \tag{4.7}$$

When $B = g\mu_B B_{\text{lab}}$, this slope is $|g_{\text{eff}}/g|$. It is an impurity Knight-shift diagnostic [65]. A field coupled uniformly to the *total* spin would instead measure the total-spin response. Spin–orbit coupling and different lead g-factors require a more general analysis, including directional dependence.

Chapter 20 demonstrates the same local-spin renormalization in the Zeeman splitting and in the matrix element for a transverse magnetic drive. A reduced g_{eff} is experimentally relevant to a spin qubit. Interpreting it quantitatively requires accounting for charge admixture and wavefunction delocalization alongside Kondo correlations, since each can reduce the local polarization.

Read the figures

A gate sweep takes a tunnel resonance down to zero energy and back up. Which physical change could produce this trace? It can cross a singlet–doublet boundary as charge or induced pairing changes. Identify the normal-state regime, the field response and the transition weights to assess the role of Kondo correlations. Likewise, observing a doublet with a reduced dot-local Zeeman slope is compatible with total spin 1/2; it reveals where that spin responds to the applied field.

Reading further. Hewson's book [62] develops the normal-state local-moment and Kondo problems. Bulla, Costi and Pruschke [63] explain why many energy scales must be retained and how NRG does so. Balatsky, Vekhter and Zhu [5] review impurity-induced bound states, while Heinrich, Pascual and Franke [29] connect individual magnetic impurities to superconducting-surface experiments.

5 Subgap spectroscopy and Andreev qubits

5.1 From an eigenstate to a measured signal

A calculated energy difference determines where a resonance *can* occur. An experiment also specifies how the system is prepared, which operator couples to the probe, and which response is detected. The same junction can therefore give different tunnelling, microwave and supercurrent spectra. A useful procedure for interpreting a measurement is

1. identify the initial state's energy, parity, spin and population;
2. identify the probe operator and its symmetry;
3. find final states with nonzero matrix elements;
4. compare their energy differences with the probe energy;
5. include temperature, broadening and the detector response.

The last step often requires physics beyond the isolated-junction Hamiltonian. An eigenstate calculation provides the energies and matrix elements that enter the response calculation; a measured line shape also depends on the probe and environment.

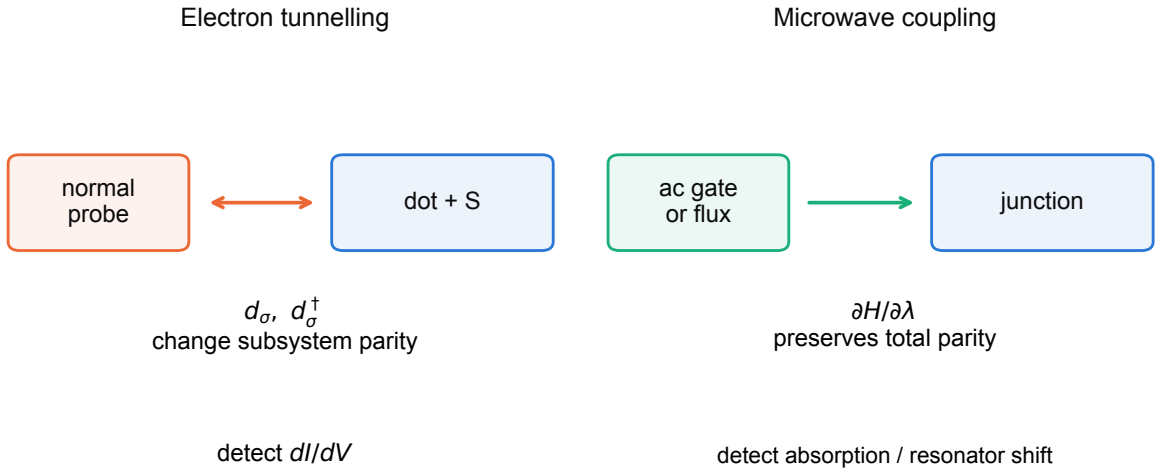


Figure 5.1: Two measurements of the same subgap system. A weak normal tunnel probe exchanges one electron with the junction and measures a conductance response. A microwave line modulates a gate or phase and is detected through absorption or a resonator response. The associated parity-changing and parity-preserving transitions have frequencies and visibility set by their respective energies, matrix elements and populations.

5.1.1 Single-electron tunnelling

For an initial ground state $|g\rangle$, define excitation energies $\omega_m = E_m - E_g \geq 0$. The zero-temperature local spectral function is

$$A_\sigma(E) = \sum_m \left[|\langle m|d_\sigma^\dagger|g\rangle|^2 \delta(E - \omega_m) + |\langle m|d_\sigma|g\rangle|^2 \delta(E + \omega_m) \right]. \tag{5.1}$$

The first term adds an electron and the second removes one. The negative-bias peak represents electron removal with the positive excitation cost ω_m. Both operators change the parity of the probed dot–superconductor subsystem. The total parity including the probe remains conserved.

For a sufficiently weak, featureless normal probe in equilibrium spectroscopy, dI/dV samples a thermally broadened version of this spectral function. We use eV as the probe electron energy relative to the junction; experimental voltage conventions must be translated before comparing signs. Peaks at opposite bias can have different intensities because the electron and hole matrix elements generally differ away from particle–hole symmetry. Spin selection rules and occupation of the initial doublet component can suppress one branch altogether.

The probe and preparation determine how this spectral function appears experimentally. A superconducting tip supplies its own energy-dependent DOS and gap, shifting and reshaping thresholds. A normal lead with appreciable coupling adds a gapless channel and can change the impurity state it is meant to probe. Nonequilibrium occupation requires spectral contributions from the populated states. Transport in an N–QD–S device can involve a complete Andreev cycle transferring a pair even though its individual spectroscopic steps exchange single electrons.

5.1.2 Microwave absorption and dispersive sensing

A weak modulation $\delta\lambda \cos(2\pi f t)$ couples through $O = \partial H/\partial\lambda$. Gate modulation is associated with charge; phase modulation with the current operator. These operators are parity even. For a transition $i \to f$, the resonance condition is

$$hf = E_f - E_i, \tag{5.2}$$

and weak net absorption contains the factor $(p_i - p_f)|\langle f|O|i\rangle|^2$, where p_i and p_f are populations. Observing a net absorption line therefore requires both a nonzero matrix element and a population contrast between the initial and final states.

A resonator can also detect the reactive response of a junction while being detuned from its transitions. Virtual transitions shift the resonator's frequency and change the phase of reflected or transmitted microwaves. This is *dispersive readout*. In a low-frequency adiabatic limit, the response is related to the curvature of a state energy with phase, or its Josephson inductance. At finite frequency it generally depends on matrix elements and transition denominators as well [66]. Interpret the frequency shift through this full junction–resonator response.

5.2 Superconducting quantum point contacts and atomic contacts

The normal conductance of spin-degenerate channels is

$$G_N = \frac{2e^2}{h} \sum_n \tau_n. \tag{5.3}$$

It determines the sum of transmissions. Resolving the individual channels requires the additional information in the nonlinear subgap current–voltage characteristic. Under voltage bias, repeated Andreev reflections allow an excitation to gain energy in steps of eV until it reaches a continuum. For equal gaps, features appear near $e|V| = 2\Delta/n$, with positive integer n, and their amplitudes depend on the channel transmissions. This *multiple Andreev reflection* (MAR) measurement is distinct from the equilibrium phase-biased spectrum of Equation (2.3).

Scheer and collaborators used superconducting transport to determine the transmission channels of atomic contacts and connect them to chemical valence [67]. Thus a few-channel junction has microscopic structure beyond its normal resistance. Once transmissions are known, the short-contact formula predicts the corresponding phase-dependent ABS branches under its assumptions.

Bretheau and collaborators detected the Andreev pair excitation of a superconducting atomic contact using a voltage-biased Josephson junction as a microwave spectrometer [30]. The spectrometer's Josephson frequency satisfies $hf = 2eV_J$, while the contact absorbs at $hf = 2E_A$. There are two different junctions and two different roles in this relation: the voltage-biased source produces radiation, and the phase-biased contact absorbs it. Identifying which junction supplies the bias keeps the factor of two discussed in Section 2.4 explicit.

The same concepts apply to gate-defined semiconductor constrictions. Microwave sensing of a gate-defined superconducting QPC was demonstrated by Chidambaram and collaborators [68]. Semiconductor junctions also permit gate-dependent channel occupation, appreciable spin–orbit coupling and longer dwell times. These features make them tunable, but require checking whether the simplest short, spin-degenerate channel formula is adequate. Nanowire microwave spectroscopy provides complementary examples [33, 41].

5.3 Reading a quantum-dot tunnelling spectrum

Deacon and collaborators studied a dot strongly coupled to a superconductor and weakly coupled to a normal probe [22]. Gate-dependent subgap resonances revealed the competition between singlet and doublet ground states. Lee and collaborators resolved the field dependence and spin splitting of these excitations [23]. These measurements connect the many-body energies of Section 3.6 to experimental lines.

Start with a singlet ground state and an excited spin-degenerate doublet. A small field splits the final doublet, so two transition energies can emerge. On the doublet-ground-state side, sufficiently low temperature can populate only the lower Zeeman component. Tunnelling to a singlet then gives a different number of branches. Thermal population of the upper component

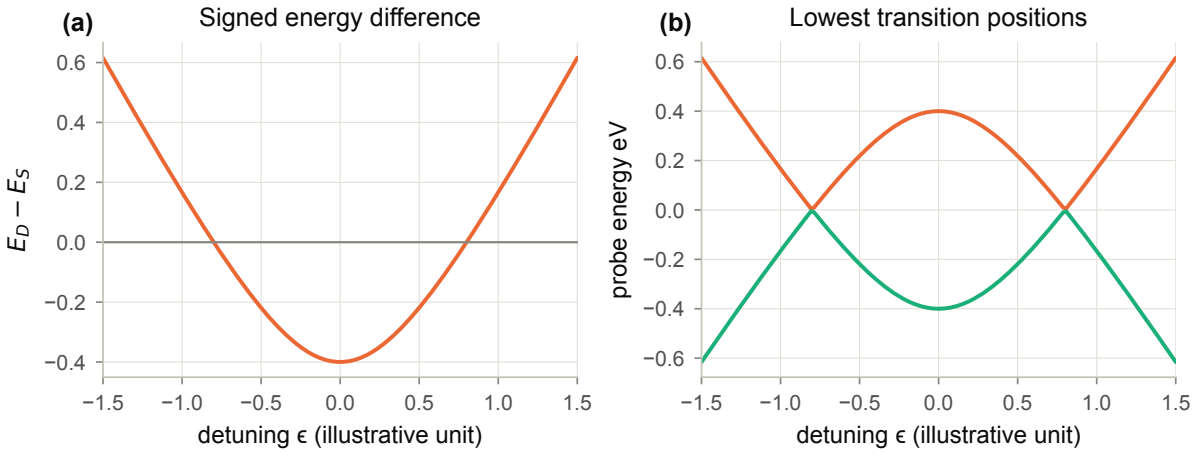


Figure 5.2: Analytic interpretation exercise for the large-gap dot, with parameters specified in Figure 3.2. (a) Signed energy difference $E_D - E_S$. (b) Positive and negative energies of the lowest single-electron transition, $\pm|E_D - E_S|$. The curves specify resonance positions; a conductance calculation would additionally require line widths, populations, transition weights and higher transitions. The doublet is the ground state between the crossings.

can restore additional lines. The number of visible lines thus reflects both the spectrum and the preparation of the initial state.

A zero-bias crossing can occur when an ordinary singlet and doublet exchange order. Distinguishing this ordinary parity transition from a Majorana mode requires additional evidence. To interpret an apparent avoided crossing as coherent hybridization, resolve the relevant line widths, thermal populations and contributing transitions, and check which levels the Hamiltonian couples.

For a useful comparison with a paper, identify the lead gaps, gate-to-energy conversion, total versus per-lead hybridization, field direction, probe coupling and temperature. Match the observable as well as the Hamiltonian. Comparing a calculated energy branch with a bright experimental ridge is meaningful only after checking which transition produces that ridge.

5.4 The even-parity Andreev-level qubit

The two even states of a short channel form the Andreev-level, or Andreev-pair, qubit: $|g\rangle$ and $|e\rangle$ of Equation (2.4). Their transition frequency is $2E_A/h$ in that model. A gate or phase modulation can drive it when the corresponding off-diagonal matrix element is nonzero. Quantitative control requires the wavefunctions or a suitable effective Hamiltonian together with the phase dependence of E_A.

Janvier and collaborators demonstrated coherent manipulation of Andreev states in superconducting atomic contacts, with resonator-based readout, Rabi oscillations and Ramsey measurements [32]. Rabi oscillations show controlled population transfer; Ramsey fringes measure the phase accumulated by a superposition. These go beyond observing an absorption resonance. The odd sector is outside the chosen even qubit space: trapping one quasiparticle can interrupt the operation and change the readout response.

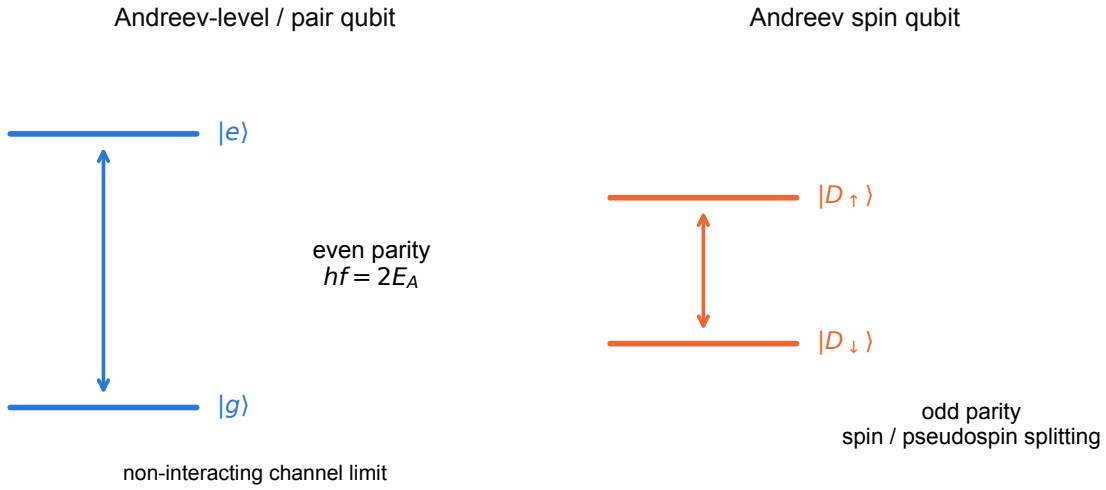


Figure 5.3: Two distinct Andreev-qubit encodings. The pair qubit uses the even ground and excited states; the spin qubit uses two states within an odd manifold. The vertical scales are schematic and independent. Parity switching leaves the selected computational space in either case. Spin labels denote pseudospins when spin–orbit coupling mixes physical spin.

For an interacting dot, the corresponding even transition is $S \to S^*$. Its frequency is $(E_{S^*} - E_S)/h$ and must be calculated independently of the lowest parity-changing excitation. The large-gap pseudospin Hamiltonian makes the distinct energy differences explicit. The driven two-level example in Chapter 13 explains the associated Rabi physics; Chapters 16 and 17 address phase and gate driving in the finite-gap junction.

5.5 The odd-parity Andreev spin qubit

An Andreev spin qubit (ASQ) uses two states within an odd-parity manifold. In a spin-conserving model these are $D_\uparrow$ and $D_\downarrow$. With spin–orbit coupling they are more generally pseudospin states with mixed spin and orbital character. The qubit splitting is the energy difference between these two odd-parity states. Quasiparticle addition and the pair excitation $2E_A$ involve different transitions.

An odd occupation can arise in two ways. A quasiparticle can be trapped in an otherwise non-interacting weak link; the duration of this occupation is then set by the parity lifetime. Alternatively, Coulomb interaction can make the odd doublet the equilibrium ground manifold over a range of gates and phases. The second route connects the superconducting Anderson model directly to a qubit architecture. Both require understanding population leakage and the gap to other states.

Hays and collaborators demonstrated continuous monitoring of a trapped spin through its spin-dependent microwave response [69]. Their subsequent coherent-control experiment used two-tone Raman transitions through auxiliary Andreev states [39]. A Raman process couples the two qubit states indirectly through driven transitions to higher levels. The energies and matrix elements of those auxiliary levels are essential to the control mechanism, even though the qubit itself is encoded in two states.

In quantum-dot devices, Bargerbos and collaborators measured spin-split Andreev levels and spin-conditioned circuit spectra [44]. Pita-Vidal and collaborators demonstrated direct electrical spin control and strong coupling to a transmon [40]. Spectroscopic avoided crossings establish hybridization between the spin and circuit excitations; determining two-qubit gate fidelity additionally requires coherent-control measurements.

5.5.1 Why can an electric field rotate a spin?

A scalar gate modulation preserves an exactly conserved spin. Spin–orbit coupling mixes spin and orbital motion so that an electric perturbation can acquire a transverse matrix element in the qubit subspace. Assess the static spin splitting and the transverse electrical coupling separately. A phase-biased structure with suitable spin–orbit and orbital structure can produce spin splitting at zero Zeeman field away from time-reversal-invariant operating points. Spin–orbit coupling alone preserves Kramers degeneracy at those points, while a spin-rotation-invariant junction retains spin degeneracy under phase bias.

This is a reason to distinguish a minimal single-orbital, spin-conserving model from a realistic all-electric ASQ Hamiltonian. Spin-dependent tunnelling, multiple orbitals or an additional conduction path may be essential. The dot-local transverse magnetic drive of Chapter 20 isolates spin renormalization and resonance physics; electrical ASQ control requires the appropriate microscopic operator and symmetry breaking.

5.6 Embedding the junction in a quantum circuit

So far ϕ has been an externally prescribed parameter. In a circuit, capacitance introduces charging energy and makes phase a quantum variable conjugate to transferred Cooper-pair number, $[\hat{\phi}, \hat{n}] = \mathrm{i}$. For an inductively shunted junction restricted to an isolated internal branch p, an illustrative Hamiltonian is

$$H_{\mathrm{circ}} = 4E_C(\hat{n} - n_g)^2 + E_p(\hat{\phi}) + \frac{E_L}{2}(\hat{\phi} - \phi_{\mathrm{ext}})^2, \qquad E_C = \frac{e^2}{2C}. \tag{5.4}$$

The dimensionless n_g is an offset charge in Cooper-pair units, and $E_L = (\hbar/2e)^2/L$ for inductance L. A reference Josephson junction provides a cosine contribution instead of this ideal inductive term. The circuit layout determines which potential is appropriate.

Near a stable minimum of the total potential $V(\phi)$, small phase oscillations have the approximate spacing $\hbar\omega \simeq \sqrt{8E_C V''(\phi_{\mathrm{min}})}$. This spacing follows from the circuit capacitance and potential curvature. The branch projection in Equation (5.4) is adiabatic: near internal-state resonances one must retain a matrix-valued junction Hamiltonian and its couplings. Charge offsets and boundary conditions must also be consistent with the chosen parity. Reviews in Refs. [57, 58] explain this connection between microscopic states and collective circuit modes.

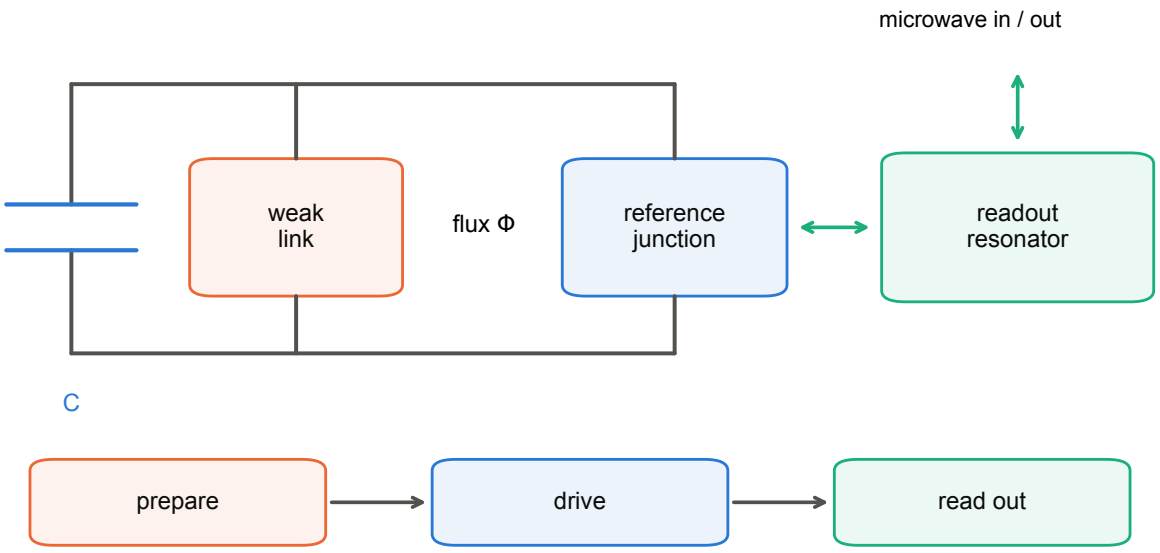


Figure 5.4: Conceptual microwave experiment. A weak link and a reference junction form a flux-controlled loop; a shunt capacitance and a coupled resonator supply collective circuit degrees of freedom and readout. The sequence separates preparation, coherent driving and measurement. Resonator output depends on the occupied junction state and the coupled circuit response. The schematic illustrates the general architecture and readout sequence.

5.7 Lifetimes, poisoning and the limits of a level diagram

Three distinct processes are relevant here. *Relaxation* transfers population between levels within the chosen system. *Dephasing* destroys relative phase coherence of a superposition. *Poisoning* changes the parity of the bound subsystem by exchanging a quasiparticle with its environment. A spin flip need not change parity; a parity switch need not be a spin flip. Escape of a driven quasiparticle into the continuum can empty a bound state while preserving the total parity of bound state plus reservoirs.

For a non-interacting channel, promoting an occupied bound quasiparticle to the continuum has threshold $\Delta - E_A$, while creating one bound and one continuum quasiparticle costs $\Delta + E_A$. The even pair transition costs $2E_A$. Identify the relevant final states and excitation threshold for each microwave process. Interacting thresholds use the appropriate many-body final energies; Chapter 16 gives a concrete example.

Measured T_1, T_2 and line widths depend on electromagnetic noise, quasiparticle distributions, drive strength and couplings to external modes. Calculating these rates requires a model of the relevant dynamical processes. Numerical Lorentzian broadening specifies the plotted line shape; interpreting its width as a lifetime requires that physical model. The package's states and operator matrix elements supply ingredients for calculating those responses.

Read the experiment

A resonator trace switches between two frequencies. Which state changes could produce this signal? It may resolve populations switching between spin states or between parities. Identify the state-dependent response and the switching process. To test coherent spin control, use controlled oscillations under a pulse and phase-sensitive Ramsey measurements. Similarly, an absorption line locates a transition, while its disappearance can reflect population changes, a selection rule or escape from the bound manifold.

A route through the literature. For devices and transport, start with De Franceschi and collaborators [15]; for dot-junction theory, use Martín-Rodero and Levy Yeyati [16] and Meden [17]. Read the atomic-contact spectroscopy and coherent-control papers together [30, 32] to see the progression from an excitation to a qubit. Then compare trapped-spin control [39] with the Coulomb-stabilized dot implementation [40]. This order keeps the encoding, measurement and microscopic model distinct while showing how they fit together.

6 Static solution methods

6.1 Which approximation answers which question?

Representing the reservoir continuum and solving the interacting many-body problem require separate approximations and checks. Exact diagonalization solves a specified finite bath, whose continuum accuracy is assessed by bath refinement. Quadratic continuum methods describe hybridization and pairing; an interacting dot requires an additional treatment of its correlations.

Table 6.1: A guide to static methods. Each row describes a physical approximation or representation. The QP and DMRG implementations are described below.

Method	Useful physical information	Validity and convergence
Scattering / BdG	ABS, electron–hole coherence, phase-dependent current	Quadratic model; the short-contact formula also assumes short dwell time
Large-gap dot	Pair mixing, parity boundary, analytic matrix elements	Infinite-gap limit with lead quasiparticles integrated out
Perturbation / fRG	Virtual processes, weak-coupling corrections	Specify the expansion or truncation and its validity
NRG	Kondo scales, impurity thermodynamics, subgap spectra	Logarithmic bath and retained-state convergence
QMC	Equilibrium correlations and finite-temperature observables	Sampling errors; real-frequency continuation is difficult
ED / QP expansion	Many-body states, energies and transitions	Finite bath; QP truncation is an additional approximation
DMRG / MPS	Correlated states with entanglement-controlled compression	Bond dimension, optimization and bath convergence

6.1.1 Scattering theory, BdG and effective dot models

For a short, non-interacting contact, scattering theory reduces the normal region to its transmission channels. The result Equation (2.3) supplies a direct analytic benchmark. A more general quadratic BdG Hamiltonian can include spatial structure, multiple orbitals, Zeeman terms and spin–orbit coupling. Diagonalizing that specified quadratic problem is exact. Replacing the interacting dot term by a static mean field is a separate approximation, which can miss quantum spin correlations or produce broken-symmetry solutions where the finite impurity has a correlated singlet. Bulk BCS mean field describes the reservoir condensate; mean-field decoupling of the dot's U approximates its local correlations.

The large-gap model is another controlled simplification with a different purpose: it retains the dot interaction exactly while integrating out the lead quasiparticles. Its small Hilbert space

exposes pair mixing and the parity transition. It is complementary to a short resonant-level junction. A broad resonance with $\Gamma \gg \Delta$ can satisfy the short-dwell-time condition, whereas the conventional large-gap dot assumes Δ exceeds the dot and hybridization scales after the wide-band limit. Choose between these approximations according to the hierarchy of scales at the parameter point of interest.

6.1.2 Perturbative and renormalization approaches

An expansion in tunnelling describes virtual charge transfer and Josephson cotunnelling in a weakly coupled dot. An expansion in U starts instead from a hybridized non-interacting problem. The expansion parameters and regimes of validity differ. Near a charge degeneracy, denominators in a tunnelling expansion become small; at low normal-state energies, Kondo logarithms can invalidate a finite-order exchange expansion even when its bare coupling is small. Use a few virtual processes to interpret the mechanism, and establish their quantitative accuracy by checking the expansion in the relevant parameter regime.

Functional renormalization group (fRG) follows the evolution of propagators and interaction vertices as a cutoff is removed. Practical truncations can describe substantial parameter ranges efficiently, but the retained frequency dependence and vertex hierarchy determine their range of validity. The dot-junction reviews [16, 17] compare these methods and their limitations. Assess both perturbative and nonperturbative calculations through their assumptions and convergence at the parameter point of interest.

6.1.3 Numerical renormalization group

NRG addresses an impurity coupled to a continuum with widely separated energy scales [63, 70]. A logarithmic discretization is transformed to a chain with successively smaller hopping scales. The chain is diagonalized iteratively, retaining low-energy many-body states at each step. The scale separation is what permits the buildup of Kondo correlations to be followed without diagonalizing the entire Fock space at once. A superconducting gap modifies this low-energy structure and produces discrete subgap levels.

NRG is an important reference for the superconducting Anderson impurity, including singlet–doublet boundaries and quantum YSR spectra. Its logarithmic discretization, retained-state number and spectral processing still require checks. More orbitals or channels increase the computational cost rapidly. Broadening a discrete numerical spectrum is useful for visualization; predicting physical lifetimes requires a dynamical calculation. For the isolated subgap poles, energies and weights are often the most direct comparison with other methods.

6.1.4 Quantum Monte Carlo

Quantum Monte Carlo (QMC) samples an interacting equilibrium problem statistically, often through imaginary-time correlation functions. Continuous-time impurity algorithms can sum an expansion to all orders by stochastic sampling. In “weak-coupling CT-QMC”, the name identifies the interaction expansion whose orders are sampled [71].

QMC provides a complementary route to finite-temperature occupation, current and correlations. Statistical uncertainty, low-temperature cost and possible model-dependent sign or phase problems must be assessed. Recovering a sharp real-frequency spectrum from noisy imaginary-time data is an ill-conditioned analytic-continuation problem. A method can therefore determine a thermal current accurately while resolving nearby subgap spectral lines less directly.

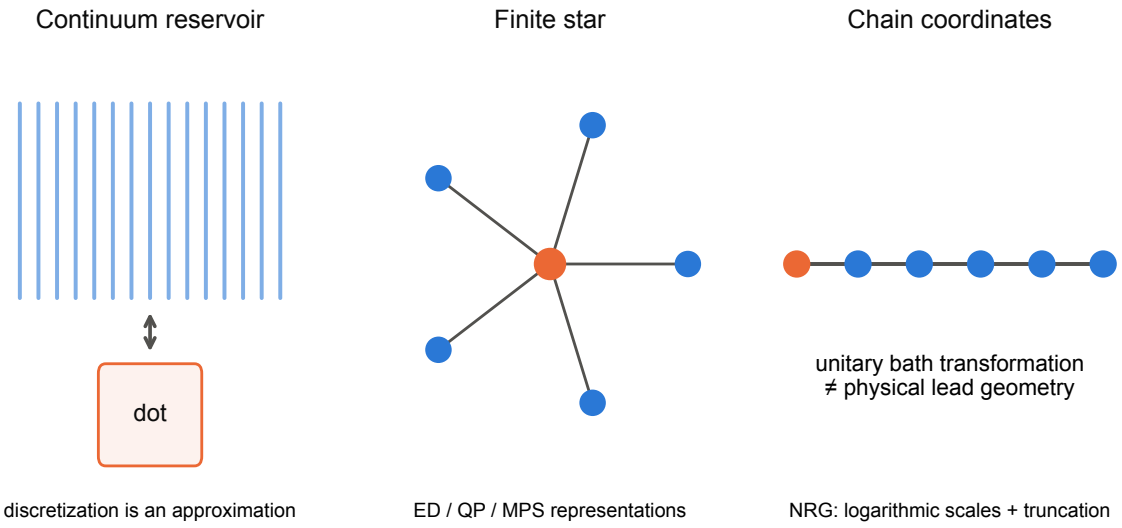


Figure 6.1: Reservoir representations and many-body approximations. A finite star couples bath orbitals directly to the dot; a unitary transformation can organize the same finite one-body bath as a chain. This coordinate change is exact. NRG combines a logarithmic discretization with iterative truncation; ED, QP truncation and MPS select different representations of the many-body state. The orbital chain is a computational representation of the reservoir's contact spectral measure.

6.1.5 Choosing a comparison

For a quadratic junction, compare with an independent electron-space BdG calculation. For the large-gap dot, compare with its exact even and odd blocks. For a small finite bath, full electron-space ED tests the many-body algebra. For a continuum local-moment problem, a converged NRG calculation can test correlation physics that a few-level bath may miss. Match the Hamiltonian, bandwidth, hybridization convention, temperature and observable before comparing numbers. Use matched-bath comparisons to assess solver accuracy and independent bath refinements to assess continuum accuracy.

6.2 Canonical coordinates

All solvers act on the Hamiltonian written in *canonical coordinates*: the impurity operators d_σ and the Bogoliubov quasiparticles $\gamma_{li\sigma}$ of the *isolated* reservoirs, Equation (3.4). In these coordinates the reservoir Hamiltonian is diagonal. When the QP expansion converges rapidly, the coupled ground state is dominated by components with few bath quasiparticles: the impurity is dressed by virtual quasiparticle excitations. Whether this description is adequate must be

checked at the couplings of interest. The map from electron operators to canonical modes is stored with the model (`metadata["coordinates"]`); `h.physical_operator` applies it to any electron operator.

Two optional reductions exploit the symmetry of the single-dot junction. The eta representation diagonalizes the particle–hole-type symmetry of Section 3.5. Paired-mode compression keeps only the combination of mirror-symmetric levels that couples to the dot and freezes the decoupled ("dark") combinations in their vacuum. Both depend on the parameters: the eta representation exists only at $\epsilon = 0$, and the compressed modes depend on ϕ. They are therefore switched off for driven calculations (Section 9.5).

6.3 The quasiparticle expansion

The Fock space of the finite model is spanned by occupation-number states of all impurity and quasiparticle modes. The QP expansion keeps every impurity configuration but at most q occupied quasiparticle modes,

$$H_q = P_q H P_q, \qquad P_q = \sum_{n \le q} \Pi_n, \tag{6.1}$$

where Π_n projects onto states with exactly n bath quasiparticles in the chosen symmetry sector. Because P_q projects onto a subspace, the lowest eigenvalue of H_q is a variational upper bound. It decreases monotonically with q and reaches the exact finite-model energy when q equals the number of bath modes (`cutoff=None`) [72, 73]. With $q = 2$, the singlet ground state is described by the dot configurations dressed by up to two quasiparticles. This captures the Yu–Shiba–Rusinov binding and much of the Kondo screening for moderate couplings. The dimension grows as $\binom{N}{q}$ with the number N of bath modes; the code counts it exactly before building the basis. Table 6.2 gives typical values for the reference junction.

The retained amplitudes are optimized together by diagonalization, summing tunnelling processes to all orders within the selected QP space. The amplitudes describe virtual QP components of a stationary state; nonequilibrium populations and poisoning rates require a dynamical model. Each sector's ground energy is an upper bound, while differences of independently truncated sector energies can approach their converged values from either side. Check the excitation gaps and transition locations themselves.

Table 6.2: Fock-space dimensions of the reference junction (two leads, `cosh_grid`), even sector $S_z = 0$ / odd sector $S_z = \frac{1}{2}$.

level pairs per lead	bath modes	$q = 2$	$q = 3$	$q = 4$
2	16	146 / 109	594 / 557	2 162 / 1 789
4	32	546 / 409	4 386 / 4 249	33 186 / 27 609
8	64	2 114 / 1 585	33 858 / 33 329	525 890 / 438 065
16	128	8 322 / 6 241	266 370 / 264 289	8 394 882 / 6 995 041

A Floquet calculation multiplies these dimensions by the number of harmonic blocks, $2M + 1$, where M is the Floquet cutoff (Section 8.2). For large baths the static eigenbasis of Section 10.2 is therefore useful.

In the code

`solve(h, cutoff, sector, options)` returns `Eigenstates` with `energies`, `vectors` (columns in the order of `basis`), `residuals`, the quasiparticle number distribution `qp_weights` and the expectation values of all model observables. The eigensolver (dense, sparse Lanczos or matrix-free) is chosen automatically according to the dimension. `ProjectedOperator(op, basis)` applies an arbitrary operator in the same Fock basis, also between different sectors. The explicit `method="block"` uses locally optimal block preconditioned conjugate gradients (LOBPCG), evolving several trial vectors together to retain degenerate multiplets; compare the complete subspace with a dense or symmetry-resolved reference. `QPWorkspace` reuses compatible preparation without changing the finite Hamiltonian or its QP projection. For small problems, its independent state count uses a full dense spectrum or Hermitian LDL factorization to check how many states lie below a specified energy boundary.

User manual: *Using the solver and saving results* (`docs/interfaces.md`).

6.4 Bath representations

The finite bath is a quadrature of the continuous reservoir. The `cosh_grid` discretization places levels with logarithmic density near the gap edge, where the bound states draw their weight. Surrogate reservoirs fit a few levels to the hybridization function on the imaginary axis [59], and the Padé chain expansion builds a short Wilson-like chain [60]. In every case three distinct approximations must be checked separately: the representation of the continuum by the finite bath, the QP cutoff, and the eigensolver tolerance. A small residual measures only the last of them.

Caution

The half-bandwidth D is a physical parameter of the reservoir. Refining the bath at fixed D converges to a finite-band continuum. Approaching the wide-band limit also requires increasing D relative to the other physical energy scales.

6.5 Density-matrix renormalization group

The DMRG solver [74, 75] represents the many-body state as a matrix-product state over the impurity and bath modes, and the Hamiltonian as a matrix-product operator; both are built with the TeNPy library [76]. DMRG retains all quasiparticle numbers and therefore complements the QP expansion when many quasiparticles matter, for instance deep in the Kondo regime. Both solvers accept the same `Hamiltonian` object, which allows direct comparisons.

An MPS controls the entanglement retained across partitions of the ordered orbital list while including all quasiparticle numbers allowed by the sector. Its bond dimension controls the number of states retained in a Schmidt decomposition. Increasing that dimension allows more correlations, but the optimization must also converge and the relevant excited states must be targeted. The orbital ordering affects the entanglement cost; it specifies the tensor-product

representation, while the Hamiltonian defines the physical geometry. Schollwöck's review [75] provides the underlying variational picture. A finite discretized bath remains an approximation with either MPS or QP states.

Three convergence questions

The eigenvector residual measures how accurately the chosen matrix problem was solved. Increasing the QP cutoff or MPS bond dimension tests whether the interacting state is represented adequately. Refining the bath tests whether that matrix problem represents the intended reservoirs. Vary these controls separately and inspect the observable of interest, especially near a parity crossing where small relative errors can exchange the ground-state ordering.

6.6 Validation

Calculations on small baths are compared with an independent exact diagonalization in the physical electron basis, built from tensor products of single-mode operators without the Bogoliubov transformation. Further checks use analytic limits, symmetry identities and finite differences of energies, e.g. the current (3.8) against the numerical derivative $\partial E/\partial\phi$. The same independent diagonalization serves as the reference for the driven problems (Section 10.7).

Chapter 7 provides a complete runnable workflow using these methods, including the static spectrum of Figure 3.3 and the physical current.

7 From a Hamiltonian to a checked calculation

7.1 State the question and the approximation

Consider the reference junction of Equation (3.7). We want its ground-state parity, lowest electron-addition/removal excitation, even pair excitation and Josephson current. Determining these quantities requires comparing the relevant sectors and evaluating state-resolved observables. The physical input and finite-bath approximation are specified in `examples/01_subgap_states/input/reference.json`, shared by the tutorial, handbook example and figure-generation scripts.

The practical sequence is

bath and impurity $\longrightarrow$ Hamiltonian $\longrightarrow$ sector solves $\longrightarrow$ observables and checks.

The bath stores signed normal levels and their contact weights. The Hamiltonian stores the interacting operator in canonical coordinates. A sector specifies total quantum numbers of the dot and leads. The result contains state-resolved energies, vectors or MPS, observables and numerical diagnostics. Physical parameters, representation choices and solver tolerances have separate roles.

7.2 A first calculation

The following setup is generated from the shared input; it uses explicit parameters so that it also runs in a fresh Python session. Energies are in gap units and the QP cutoff is a many-body approximation to the declared finite bath.

```
import numpy as np
from qdjj_solver import Sector, cosh_grid, reference_model
from qdjj_solver.qp_solver import SolverOptions, solve

bath = cosh_grid(**{'pairs': 4, 'delta': 1.0, 'bandwidth': 10.0})
model = dict(bath=bath, **{'u': 1.0, 'gamma': 0.5, 'phi': 0.8, 'detuning': 0.2, '
    field': 0.0, 'symmetry': False, 'compress': False})
h = reference_model(**model)
even = solve(h, cutoff=2, sector=Sector(0, 0), options=SolverOptions(eigenpairs=2))
odd = solve(h, cutoff=2, sector=Sector(1, 1))
partner = solve(h, cutoff=2, sector=Sector(1, -1))
print(even.energies, odd.energies, partner.energies)
```

The last array compares the spin projections of the doublet. Their degeneracy is a check at zero field; in a finite field both must be included when finding the global minimum. The even sector supplies the singlet S and excited singlet S^*. At the reference point, $E_D - E_S = 0.096$ and $E_{S^*} - E_S = 0.716$. The signed first difference identifies which parity lies lower. The positive excitation cost is its absolute value, whereas the pair excitation connects two states of the same even sector.

From the source root the matching even calculation can also be run with:

```
qdjj-solver solve examples/01_subgap_states/input/reference.json --output results/
    even.json --save-states
```

This command solves the sector named by the input. Run the other relevant sectors to determine the global ground state. The input contains the numerical settings as well as the model, which makes differences between Python and command-line defaults irrelevant to this explicit comparison.

7.3 Interpret observables and matrix elements

Each observable array has one entry per returned state. The current derivative is reported in energy units; multiplying it by $2e/\hbar$ gives the physical current. For a normalized gap-unit calculation, the corresponding dimensionless number is $I/(2e\Delta/\hbar)$.

```
current = even.observables["phase_derivative"][0].real
charge = even.observables["impurity_charge"][0].real
addition = odd.matrix_elements("d_up_dagger", even)
pair = even.matrix_elements("current")
print(current, charge, abs(addition[0, 0])**2, abs(pair[1, 0])**2)
```

The rows of a transition matrix label the bra/final states and columns the ket/initial states. Thus the first squared amplitude adds a spin-up dot electron to S and reaches the chosen odd state, while the second connects S to S^*. The matrix element specifies the coupling strength; predicting the measured response also requires initial-state populations and line widths. Named electron probes are already transformed to the model's canonical coordinates. For arbitrary physical operators use the transformation described in Section 6.2.

7.4 Sweep a parameter and retain the results

The standalone script `examples/handbook/scan.py` scans phase, writes both sector results after every completed point, and retains any failed point with its diagnostic. Its plotting mode reads those saved results without solving again. Follow the smooth sector branches first, then construct their lower envelope and ground-state current as in Figure 3.4.

Use a dense phase grid to locate parity crossings, and refine the QP cutoff and bath to converge their positions. Track states through same-sector crossings using symmetries, observables

and, in compatible coordinates, overlaps. At exact degeneracy compare the complete relevant subspace.

7.5 Ask three separate convergence questions

1. Does the result solve its declared finite matrix problem? Inspect residuals and orthogonality; DMRG also provides sweep and independent-trial diagnostics.
2. Is the many-body representation adequate? Refine QP cutoff or MPS bond dimension and compare the excitation, current or correlation actually reported.
3. Is the bath adequate? Refine its nodes or fit at fixed physical parameters, with adequate many-body convergence at each size.

The small DMRG tutorial deliberately begins with insufficient bond dimension, then approaches the result of full ED for the same finite bath, demonstrating the first two checks. Apply the third through bath refinement. The larger reference junction here illustrates a finite-bath, cutoff-two calculation; assess its continuum accuracy using all three checks.

Tutorial: *DMRG bond-dimension convergence* (`examples/11_dmrg_convergence`).

7.6 Save states and prepare for driving

```
from qdjj_solver import save_result, load_result
save_result(even, "results/even.json", save_states=True)
restored = load_result("results/even.json")
assert np.max(abs(restored.energies - even.energies)) < 1e-12
```

The JSON stores scalar results, settings and provenance; the companion NPZ or HDF5 file stores wavefunctions. Keep both together. Scalar-only plotting can use ordinary JSON tools, but evaluating a new matrix element requires the states. Saved, completed DMRG states provide initial wavefunctions for a new compatible optimization.

The static transition energy and its matrix element now identify a candidate resonance for the driven part of the manual. Retain fixed canonical coordinates when introducing the drive. Chapters 8 and 9 develop that step before the numerical Floquet methods are applied.

The complete software handbook

User manual: *Static states, observables and transitions* (`docs/static_calculations.md`); User manual: *Parameter scans, saved results and reproducible analysis* (`docs/workflows.md`); User manual: *DMRG states and bond-dimension refinement* (`docs/dmrg.md`). The separate User's Guide and Reference Manual PDF also gives installation, full constructor and solver references, JSON formats, saved-record fields and troubleshooting. Both manuals are published with the matching software release.

Tutorial: *A first calculation* (`examples/00_first_calculation`).

Part II

Periodic driving

8 Floquet theory for periodically driven systems

This chapter introduces the physics of periodically driven quantum systems and develops Floquet theory from its basic principles. Extensive reviews are available in Refs. [52, 53, 77–80]; here we develop the concepts needed to understand and use the Floquet methods in qdjj_solver.

8.1 Periodic Hamiltonians and the Floquet theorem

Consider a Hamiltonian with period $T = 2\pi/\Omega$,

$$H(t+T) = H(t), \qquad \mathrm{i}\partial_t|\psi(t)\rangle = H(t)|\psi(t)\rangle. \tag{8.1}$$

The system exchanges energy with the drive, and its state evolves in time. The periodicity constrains the time-evolution operator $U(t, t_0)$: the evolution over one period is identical for starting times separated by an integer number of periods. The one-period propagator $U(T, 0)$ is unitary; let its eigenvectors be $|\varphi_\alpha\rangle$ with eigenvalues $\mathrm{e}^{-\mathrm{i}\varepsilon_\alpha T}$. The states

$$|\psi_\alpha(t)\rangle = U(t,0)|\varphi_\alpha\rangle = \mathrm{e}^{-\mathrm{i}\varepsilon_\alpha t}|u_\alpha(t)\rangle, \qquad |u_\alpha(t+T)\rangle = |u_\alpha(t)\rangle, \tag{8.2}$$

are solutions of the Schrödinger equation that differ from stationary states only by a periodic "micromotion" $|u_\alpha(t)\rangle$. This is the Floquet theorem [81–84]. The quantities ε_α are the *quasienergies*, the $|u_\alpha(t)\rangle$ are the *Floquet modes*, and the $|\psi_\alpha(t)\rangle$ are the *Floquet states*. The modes form a complete basis at every time, so any solution is $|\psi(t)\rangle = \sum_\alpha c_\alpha \mathrm{e}^{-\mathrm{i}\varepsilon_\alpha t}|u_\alpha(t)\rangle$ with constant coefficients: the Floquet states play the role of the energy eigenstates of a static problem.

The quasienergy is defined only modulo Ω. Replacing ε_α by $\varepsilon_\alpha + \ell\Omega$ and $|u_\alpha(t)\rangle$ by $\mathrm{e}^{\mathrm{i}\ell\Omega t}|u_\alpha(t)\rangle$ leaves $|\psi_\alpha(t)\rangle$ unchanged for every integer ℓ. This is the temporal analogue of the quasimomentum in Bloch's theorem: quasienergies can be represented in a Brillouin zone of width Ω, for instance $[-\Omega/2, \Omega/2)$.

Physical picture

A static system has energy levels; a periodically driven system has quasienergy levels. They determine the phases accumulated over each period and enter the conditions for interference, resonances and spectroscopic transitions. A state that is an energy eigenstate without the drive is continuously deformed into a Floquet state as the drive is switched on, as long as no resonance is crossed.

Effective Hamiltonian and micromotion. The one-period propagator can be written as $U(T,0) = \mathrm{e}^{-\mathrm{i}H_F T}$ with the *Floquet Hamiltonian* H_F, whose eigenvalues are the quasienergies. H_F depends on the time at which the period starts, while its spectrum is time-origin invariant. The full evolution separates into a slow evolution under a time-independent *effective Hamiltonian* H_{eff} and a periodic micromotion generated by the kick operator $\mathcal{K}(t) = \mathcal{K}(t+T)$, $U(t,0) = \mathrm{e}^{-\mathrm{i}\mathcal{K}(t)}\mathrm{e}^{-\mathrm{i}H_{\mathrm{eff}}t}\mathrm{e}^{\mathrm{i}\mathcal{K}(0)}$. At $t = T$ this gives $H_F = \mathrm{e}^{-\mathrm{i}\mathcal{K}(0)} H_{\mathrm{eff}} \mathrm{e}^{\mathrm{i}\mathcal{K}(0)}$: both operators have the same spectrum, and H_{eff} is invariant under shifts of the time origin [50, 51, 85]. The high-frequency expansion of Section 10.4 approximates H_{eff}.

8.2 Fourier space: the Sambe picture

Since $H(t)$ and $|u(t)\rangle$ are periodic, both can be expanded in harmonics of Ω. qdjj_solver uses the convention

$$H(t) = \sum_k H_k \, \mathrm{e}^{\mathrm{i}k\Omega t}, \qquad H_{-k} = H_k^\dagger, \qquad |u(t)\rangle = \sum_m \mathrm{e}^{\mathrm{i}m\Omega t} |u_m\rangle. \tag{8.3}$$

Inserting $|\psi(t)\rangle = \mathrm{e}^{-\mathrm{i}\varepsilon t}|u(t)\rangle$ into the Schrödinger equation and comparing the coefficients of $\mathrm{e}^{\mathrm{i}m\Omega t}$ gives

$$\sum_{m'} \left(H_{m-m'} + m\Omega \, \delta_{mm'} \right) |u_{m'}\rangle = \varepsilon \, |u_m\rangle. \tag{8.4}$$

This is a time-independent eigenvalue problem for the infinite block matrix

$$Q = \begin{pmatrix} \ddots & & & & \\ & H_0 - \Omega & H_{-1} & H_{-2} & \\ & H_1 & H_0 & H_{-1} & \\ & H_2 & H_1 & H_0 + \Omega & \\ & & & & \ddots \end{pmatrix}, \tag{8.5}$$

which acts in the extended (Sambe) space of T-periodic states with scalar product $\langle\!\langle a|b\rangle\!\rangle = T^{-1}\int_0^T \mathrm{d}t \, \langle a(t)|b(t)\rangle$ [86]. The diagonal blocks are copies of the time-averaged Hamiltonian H_0 shifted by multiples of Ω; the off-diagonal blocks are the drive harmonics. For a monochromatic drive linear in a parameter, only $H_{\pm 1}$ are nonzero and Q is block-tridiagonal. qdjj_solver truncates the matrix to the blocks $|m| \le M$, where M is the *Floquet cutoff* (option `floquet_cutoff`).

Replicas. The eigenvalue problem (8.4) is invariant under the shift $|u_m\rangle \to |u_{m-\ell}\rangle$ combined with $\varepsilon \to \varepsilon + \ell\Omega$, for any integer ℓ. Every physical Floquet state therefore appears as an infinite ladder of *replicas*, one per Brillouin zone. The harmonic weights $\|u_m\|^2$ sum to one (for $\langle\!\langle u|u\rangle\!\rangle = 1$), and their centroid $\langle m\rangle = \sum_m m\|u_m\|^2$ shifts by ℓ from one replica to the next. The truncation distorts the replicas near the edges of the window $|m| \le M$. The code therefore works with the most central replica and reports the weight in the outermost blocks as a convergence diagnostic.

Mean energy. Taking the expectation value of (8.4) in a normalized Floquet mode gives

$$\bar{E} \equiv \frac{1}{T}\int_0^T \mathrm{d}t\, \langle\psi(t)|H(t)|\psi(t)\rangle = \varepsilon - \Omega\langle m\rangle, \tag{8.6}$$

the time-averaged energy of the Floquet state. The value of $\bar{E}$ is replica invariant, making it a natural label for a Floquet state; it is reported as `mean_energies`.

8.3 An exactly solvable example

Consider a spin $\frac{1}{2}$ (or any two-level system) in a static field and a circularly polarized field,

$$H(t) = \frac{\omega_0}{2}\sigma_z + \frac{b}{2}\left(\mathrm{e}^{-\mathrm{i}\Omega t}\sigma_+ + \mathrm{e}^{\mathrm{i}\Omega t}\sigma_-\right), \qquad H_{-1} = \frac{b}{2}\sigma_+, \quad H_1 = \frac{b}{2}\sigma_-, \tag{8.7}$$

This problem is solved by transforming to a rotating frame. The transformation $W(t) = \mathrm{e}^{\mathrm{i}\Omega t\sigma_z/2}$ gives, by Equation (8.9), the static Hamiltonian $H' = \frac{1}{2}(\omega_0 - \Omega)\sigma_z + \frac{b}{2}\sigma_x$ with eigenvalues $\pm\frac{1}{2}w$, $w = \sqrt{(\omega_0-\Omega)^2 + b^2}$. Transforming back, the spin-up component of each solution acquires $\mathrm{e}^{-\mathrm{i}\Omega t/2}$ and the spin-down component $\mathrm{e}^{+\mathrm{i}\Omega t/2} = \mathrm{e}^{-\mathrm{i}\Omega t/2}\mathrm{e}^{\mathrm{i}\Omega t}$. The Floquet states therefore have

$$\varepsilon_\pm = \frac{\Omega \pm w}{2} \pmod{\Omega}, \qquad |u(t)\rangle = |u_0\rangle + \mathrm{e}^{\mathrm{i}\Omega t}|u_1\rangle, \quad |u_0\rangle \propto |\uparrow\rangle,\ |u_1\rangle \propto |\downarrow\rangle. \tag{8.8}$$

Exactly two harmonics have nonzero amplitudes. In the photon picture of Section 8.4, the spin-down component is accompanied by one more photon in the field than the spin-up component. Away from resonance, $|\omega_0 - \Omega| \gg b$, the two quasienergies approach $\omega_0/2$ and $-\omega_0/2 + \Omega$, which are the bare energy of $|\uparrow\rangle$ and the bare energy of $|\downarrow\rangle$ plus one photon. At resonance, $\Omega = \omega_0$, these replicas would cross; the drive opens a gap b between them, the Rabi splitting. A system prepared in $|\uparrow\rangle$ oscillates as $P_\downarrow(t) = (b^2/w^2)\sin^2(wt/2)$, so the Rabi splitting at resonance equals the frequency of the Rabi oscillations. For a linearly polarized field, $b\cos(\Omega t)\sigma_x$, the same picture holds up to counter-rotating corrections of order b^2/ω_0 (Chapter 13). qdjj_solver reproduces Equation (8.8) to machine precision with all its methods, and the code is tested against it.

8.4 The photon picture

Equation (8.4) has a transparent interpretation. Consider the system coupled to a single quantized field mode of frequency Ω, $H_{\mathrm{sys}} + \Omega a^\dagger a + H_{\mathrm{int}}$, in a coherent state with a large mean photon number $\bar{N}$. In the limit $\bar{N} \to \infty$ at fixed field amplitude, the Hamiltonian in the basis $|\alpha\rangle \otimes |\bar{N} + m\rangle$ becomes exactly Q. Here m is the change of the photon number relative to $\bar{N}$: $|m|$ photons have been absorbed from the field for $m < 0$ and emitted into it for $m > 0$ [82, 87, 88]. The Floquet states are the *dressed states* of the system and the field. The diagonal blocks $H_0 + m\Omega$ are the bare levels with m extra photons, and the harmonic weight $\|u_m\|^2$ is the probability that m photons have been exchanged with the field. The quasienergy spectrum is the spectrum of the dressed system, measured relative to a field energy that is defined only up to multiples of Ω.

Physical picture

Two bare levels E_a and E_b are resonant when $E_b - E_a = k\Omega$ for some integer k: in the photon picture, the states $|a\rangle \otimes |\bar{N}\rangle$ and $|b\rangle \otimes |\bar{N} - k\rangle$ are degenerate, and absorbing k photons transfers the system from a to b without energy cost. The drive couples them, and the Floquet spectrum shows an avoided crossing, the Autler–Townes splitting [89]. For $k = 1$ its size is set directly by the first harmonic of the drive. For $k > 1$ it comes from the harmonic H_k, from virtual intermediate states, or, for strong modulation, from Bessel functions of the modulation index.

8.5 Gauge freedom and the energy zero

A time-dependent unitary transformation $|\psi\rangle \to W(t)|\psi\rangle$ maps the Schrödinger equation onto one with

$$H'(t) = W(t)H(t)W^\dagger(t) + \mathrm{i}\,(\partial_t W(t))W^\dagger(t). \tag{8.9}$$

If $W(t)$ is periodic, the quasienergies of H and H' coincide modulo Ω, while the Floquet modes are multiplied by $W(t)$. Two consequences are used throughout this manual.

1. A c-number term $c(t)$ in $H(t)$ multiplies ψ by the phase $\exp[-\mathrm{i}\int c\,\mathrm{d}t]$. Its time average shifts all quasienergies equally; its oscillating part only redistributes the harmonic weights. qdjj_solver keeps such terms by default, so the Floquet problem uses $H(t)$ exactly as built (option `drop_scalar_harmonics` removes the oscillating c-number terms).

2. A time-dependent superconducting phase on the tunnelling terms can be traded for a time-dependent electrochemical potential, i.e. a voltage (Section 9.2).

8.6 Regimes

Weak driving. Without the drive, $\varepsilon_a = E_a$ and $|u_m\rangle = \delta_{m0}|a\rangle$. To second order in the drive, the quasienergy of a nondegenerate state shifts by the dynamical (AC) Stark shift

$$\delta\varepsilon_a = \sum_{(b,m)\neq(a,0)} \frac{|\langle b|H_m|a\rangle|^2}{E_a - E_b - m\Omega}, \tag{8.10}$$

obtained by perturbation theory in the Sambe space. Here E_a and $|a\rangle$ are the eigenvalues and eigenstates of the time-averaged Hamiltonian H_0. For a drive linear in a parameter, H_0 is the undriven Hamiltonian. For a nonlinear drive, such as the phase drive, H_0 itself changes at second order in the amplitude (Equation (9.4)), and this change adds to (8.10). The denominators vanish at the resonances $E_b - E_a = -m\Omega$, where degenerate perturbation theory, the rotating-wave approximation of Section 10.5, must be used.

Resonant driving. Near a one-photon resonance the two coupled states $|a\rangle \otimes |\bar{N}\rangle$ and $|b\rangle \otimes |\bar{N}-1\rangle$ form an isolated two-level system. Its splitting at resonance, the Rabi splitting, is $2|\langle b|H_{-1}|a\rangle|$; it equals the frequency of Rabi oscillations between a and b [90]. The counter-rotating couplings shift the resonance by an amount of second order in the drive, the Bloch–Siegert shift [82, 91].

Slow driving. For Ω small compared with the gaps to all other levels, the system follows the instantaneous eigenstate $|a(t)\rangle$ adiabatically. The quasienergy becomes the time average of the instantaneous energy $E_a(t)$, corrected by the geometric (Berry) phase γ_a accumulated per period [92, 93],

$$\varepsilon_a \simeq \frac{1}{T}\int_0^T E_a(t)\,\mathrm{d}t - \frac{\gamma_a}{T} \pmod{\Omega}. \tag{8.11}$$

The Berry phase vanishes when the parameter moves back and forth along a line, as for a single-parameter cosine drive.

Fast driving. For Ω larger than all other energy scales the time-averaged Hamiltonian governs the leading response. The quasienergies then follow from a static effective Hamiltonian, expanded in powers of $1/\Omega$ (Section 10.4) [51, 85, 94–97]. Strong fast driving renormalizes couplings by Bessel functions, which can switch them off entirely: coherent destruction of tunnelling [98] and dynamical localization [99] (Chapter 14).

Strong driving. When the modulation of a level is large compared with Ω, many harmonics are involved and multiphoton resonances appear, with couplings renormalized by Bessel functions of the modulation index. In two-level systems this produces the Landau–Zener–Stückelberg interference patterns [100–103] (Chapter 13).

8.7 Floquet states coupled to a continuum

The subgap states of a junction are discrete, but the continuum begins at $E_{\mathrm{ground}} + \Delta$. A replica $|a\rangle \otimes |\bar{N}+m\rangle$ of a bound state that falls into the continuum, $E_a + m\Omega > E_{\mathrm{ground}} + \Delta$, is degenerate with continuum states. In an infinite system it acquires a decay rate given by the golden rule, $2\pi|V|^2\rho_c$, with V the drive matrix element and ρ_c the density of continuum states. Physically, the drive can excite quasiparticles out of the bound state, the analogue of the multiphoton ionization of an atom. The Floquet state then becomes a resonance with a finite lifetime [79, 104].

In a finite bath the continuum is a set of discrete levels. The replicas of these levels cross the bound state as a parameter is varied, and every crossing becomes a narrow avoided crossing. As the bath is refined, the crossings become denser and narrower; their positions and gaps depend on the discretization. Hone, Ketzmerick and Kohn analysed this generic behaviour of Floquet spectra with dense sets of levels, and the related absence of a strict adiabatic limit [105, 106].

Caution

Narrow avoided crossings with continuum replicas redistribute a dressed bound state's weight among the discrete finite-bath states. Their positions and gaps depend on the discretization; in the continuum their collective effect gives a finite lifetime. Identify physical features by following the dressed states' static weights and checking stability under bath refinement (Chapter 15).

8.8 What is observable

Weak-probe spectroscopy measures quasienergy differences combined with integer multiples of the drive frequency. The probe induces transitions between Floquet states at the frequencies

$$\omega = \varepsilon_\alpha - \varepsilon_\beta + q\Omega, \qquad q \in \mathbb{Z}, \tag{8.12}$$

with strengths given by the harmonics of the probe matrix element between the two Floquet modes. Which lines are actually seen also depends on the populations of the Floquet states. Relaxation sets these populations: in an open system they follow from a Floquet master equation [106–109]. qdjj_solver computes the quasienergies, modes and probe matrix elements (Chapter 11). A calculation of the populations using the same modes is planned. At present, spectra are evaluated for explicitly specified initial states.

In the code

`solve_floquet` returns `FloquetStates` with the `quasienergies` on a definite branch (Section 10.2), the `folded` values in a chosen zone, the `mean_energies` (8.6), the harmonics $|u_m\rangle$ of the modes (`modes`), the `harmonic_weights` $\|u_m\|^2$ and the `static_weights`, the time-averaged weights $\sum_m |\langle a|u_m\rangle|^2$ of the undriven eigenstates $|a\rangle$. `mode_at(t)` and `state_at(t)` evaluate $|u(t)\rangle$ and $|\psi(t)\rangle$. `matrix_elements` computes probe matrix elements (Chapter 11), and `dressed_state(label)` returns the index of the Floquet state that continues the static state `label`.

User manual: *Floquet calculations* (`docs/floquet.md`).

9 Driving the junction

9.1 Which parameters can be driven

In qdjj_solver a drive is a periodic modulation of one or several model parameters,

$$p(t) = p_0 + \sum_n A_n \cos(n\Omega t + \theta_n), \tag{9.1}$$

and the driven Hamiltonian is $H(t) = H\big(p(t)\big)$, built by the same model constructor as the static one. For a monochromatic drive we write $A \equiv A_1$ and $\theta \equiv \theta_1$. To distinguish the driven parameters, A_ϕ denotes the amplitude of a phase drive (in radians) and A_ϵ that of a gate drive (an energy). The physically important cases are the following.

Gate drive. An ac voltage on a gate electrode modulates the dot level, $\epsilon(t)$. Because H_d is linear in ϵ, $H(t) = H(\epsilon_0) + (n_d - 1)\sum_n A_n \cos(n\Omega t + \theta_n)$. A monochromatic drive has only the harmonics $H_{\pm 1} = \frac{A_\epsilon}{2} e^{\pm i\theta}(n_d - 1)$. This is the setting of photon-assisted tunnelling through quantum dots [110–113].

Phase drive. Microwaves applied to a superconducting loop or across the junction modulate the phase difference, $\phi(t)$. Since the phase enters the tunnelling through the factors $e^{\pm i\phi/4}$, $H(t)$ contains all harmonics, with Bessel-function amplitudes (Section 9.3). This is how Andreev levels are excited in microwave spectroscopy [30, 32, 34, 114].

Coupling drive. A gate on a tunnel barrier modulates Γ_l, which enters the Hamiltonian through $t_l \propto \sqrt{\Gamma_l}$ [115].

Field drive. An oscillating magnetic field along z modulates the Zeeman energy. A transverse field $b(t)S_d^x$ flips the spin and breaks the conservation of S_z; this is electron spin resonance (ESR) of the impurity spin (Chapter 20) [116–118].

Combined drives. Several parameters may be modulated simultaneously with relative phase offsets, for example by a gate electrode that also couples capacitively to the junction phase.

In the code

```
from qdjj_solver import Harmonic, ParameterDrive, PeriodicHamiltonian,
    reference_model
from qdjj_solver.qp_solver import solve_floquet
drives = [ParameterDrive.cosine("phi", .3),                    # phi0 + 0.3
    cos(Omega t)
          ParameterDrive("detuning", (Harmonic(1, .02, np.pi/2),  # two
    harmonics
                                      Harmonic(2, .01)))]
```

```
periodic = PeriodicHamiltonian.from_parameters(reference_model, model, drives,
    omega=.5)
```

The model constructor, here `reference_model`, is evaluated at equally spaced times over one period (`samples`, default 64), and every operator coefficient is Fourier transformed (Section 10.1). `from_callable(f, omega)` accepts any function `f(t)` that returns a `Hamiltonian`.

User manual: *Floquet calculations* (`docs/floquet.md`).

9.2 Phase drive, voltage and the Josephson relation

The superconducting phase is included in the tunnelling amplitudes, Equation (3.6). With this choice a time-dependent phase is equivalent to a voltage. The periodic transformation $W(t) = \exp[-\mathrm{i}\sum_l \phi_l(t) N_l/2]$, with N_l the electron number of lead l, removes the phases from the tunnelling and moves them onto the pair potentials. By Equation (8.9) it also adds the term $\sum_l (\hbar\dot{\phi}_l/2) N_l$, which raises the electrochemical potential μ_l of lead l by $\hbar\dot{\phi}_l/2$. We define the bias voltage $V = V_L - V_R$ as the electric potential of the left lead relative to the right one. Since electrons carry the charge $-e$, $eV = \mu_R - \mu_L$, and the phase difference $\phi = \phi_R - \phi_L$ obeys the Josephson relation

$$\dot{\phi} = \frac{2e}{\hbar} V. \tag{9.2}$$

With the current I of Equation (3.8), positive from the left to the right lead, the power supplied by the voltage source is $IV = \dot{\phi}\,\partial E/\partial\phi$. For a single lead, the phase can instead be moved onto the dot with $W(t) = \mathrm{e}^{\mathrm{i}\phi(t) n_d/2}$, which gives

$$H'(t) = H(\phi = 0) - \frac{\dot{\phi}(t)}{2}\, n_d, \tag{9.3}$$

i.e. a level drive $\epsilon(t) = \epsilon_0 - \dot{\phi}/2$ with identical quasienergies. The code is tested against this identity (Section 10.7). The same gauge freedom underlies the description of voltage-biased junctions and multiple Andreev reflection as Floquet scattering problems [119–122].

9.3 Harmonics of the phase drive

For the reference junction with $\phi(t) = \phi_0 + A\cos(\Omega t + \theta)$, where $A \equiv A_\phi$ in this section, each tunnelling factor $\mathrm{e}^{\pm\mathrm{i}\phi(t)/4}$ contains $\mathrm{e}^{\pm\mathrm{i}(A/4)\cos(\Omega t+\theta)}$. The Jacobi–Anger expansion $\mathrm{e}^{\mathrm{i}z\cos\vartheta} = \sum_n \mathrm{i}^n J_n(z)\mathrm{e}^{\mathrm{i}n\vartheta}$ [123] gives the harmonics in closed form (Appendix A.1):

$$H_0 = H(\phi_0)\big|_{\Gamma\to\Gamma J_0(A/4)^2}, \tag{9.4}$$

$$H_k = 4(-1)^{(k-1)/2} J_k\!\left(\tfrac{A}{4}\right) \mathrm{e}^{\mathrm{i}k\theta}\, \frac{\partial H}{\partial\phi}\bigg|_{\phi_0} \qquad (k \text{ odd}), \tag{9.5}$$

$$H_k = (-1)^{k/2} J_k\!\left(\tfrac{A}{4}\right) \mathrm{e}^{\mathrm{i}k\theta}\, H_T(\phi_0) \qquad (k \neq 0 \text{ even}), \tag{9.6}$$

where H_T is the tunnelling Hamiltonian. Three consequences are useful. First, for a weak drive $H_{\pm1} \approx \frac{A}{2}\mathrm{e}^{\pm\mathrm{i}\theta}\partial H/\partial\phi$: the phase drive couples through the current operator, and the one-photon

Rabi splitting between two states is $A|\langle b|\partial H/\partial\phi|a\rangle|$. Second, the time-averaged hybridization is reduced by the factor $J_0(A/4)^2$, which vanishes at $A \approx 9.62$ (Chapter 14). Third, the even harmonics are proportional to H_T and the odd ones to $\partial H/\partial\phi$, so two-photon processes probe a different operator from one-photon processes.

9.4 From laboratory parameters to drive amplitudes

The code works with energies in units of Δ and dimensionless phases. Typical conversions are:

- *Frequency.* $\Omega/\Delta = hf/\Delta$; for an aluminium gap $\Delta \approx 180\,\mu$eV, $\Omega = 1$ corresponds to $f \approx 44\,$GHz, and a typical microwave frequency of 10 GHz to $\Omega \approx 0.23$.
- *Voltage drive.* An ac voltage $V_{\rm ac}\cos\Omega t$ across the junction gives $\dot\phi = (2e/\hbar)V_{\rm ac}\cos\Omega t$, hence the phase amplitude $A_\phi = 2eV_{\rm ac}/(\hbar\Omega)$, the familiar Tien–Gordon modulation index of Cooper pairs.
- *Flux drive.* In a loop threaded by a flux Φ, $\phi = 2\pi\Phi/\Phi_0$ with $\Phi_0 = h/2e$, so a flux modulation $\delta\Phi$ gives $A_\phi = 2\pi\,\delta\Phi/\Phi_0$.
- *Gate drive.* An ac gate voltage of amplitude V_g shifts the level by αeV_g, with the lever arm α; hence $A_\epsilon = \alpha eV_g/\Delta$.

Microwave spectroscopy usually operates in the weak-drive regime, $A_\phi \ll 1$ and $A_\epsilon \ll \Omega$. Floquet engineering and the strong-driving phenomena of Chapters 13 and 14 require modulation indices of order one.

9.5 Fixed canonical coordinates

The QP basis is built from the Bogoliubov quasiparticles of the isolated reservoirs, which depend on Δ_l and on the bath levels ξ_{li} and remain fixed as ϵ, U, B, Γ_l or ϕ_l vary. All drives of the latter parameters therefore act on a fixed Fock space, and the Sambe construction applies directly. If the coordinates themselves varied with time, e.g. for a modulated gap $\Delta(t)$, the transformed Hamiltonian would acquire the additional term $\mathrm{i}(\partial_t W)W^\dagger$ of Equation (8.9). The implemented methods use fixed coordinates: `qdjj_solver` checks that those of every sampled Hamiltonian coincide with those of the undriven model, and rejects drives that change them. The eta representation and paired-mode compression depend on ϵ and ϕ, so driven models are built with `symmetry=False, compress=False`.

9.6 Selection rules

A drive conserves fermion parity, so it couples only states of the same parity. Parity-changing transitions require the exchange of a quasiparticle with an external system. Drives that conserve S_z (gate, phase, coupling, longitudinal field) act within sectors of fixed S_z, and the calculation is done sector by sector. A transverse field requires `Sector(parity, None)`.

At the particle–hole-symmetric point of the symmetric junction the eta parity provides a further, less obvious selection rule. The phase drive and the coupling drive are eta-even and couple only states of equal eta parity; the gate drive, proportional to $n_d - 1$, is eta-odd and couples only states of opposite eta parity. The lowest two even states S and S^* have opposite eta parity, so at $\epsilon = 0$ the pair transition $S \to S^*$ is invisible to the phase drive and maximally visible to the gate drive. Away from $\epsilon = 0$ both drives couple the pair. Chapter 17 demonstrates these complementary rules. For a non-interacting resonant level the same rule reads as follows: the symmetric junction at resonance is reflectionless, and the current matrix element of the pair transition, proportional to $\sqrt{1-\tau}$ with τ the transmission, vanishes [36, 114].

9.7 The driven proximitized dot

The large-gap limit (3.9) gives a transparent model of the driven even sector. We write the pseudospin Hamiltonian as

$$H = \frac{U}{2} + \epsilon\,\tau_z - |\Gamma_\phi|\,\tau_x = \frac{U}{2} + R\,(\cos\vartheta\,\tau_z - \sin\vartheta\,\tau_x), \qquad R = \sqrt{\epsilon^2 + |\Gamma_\phi|^2}, \quad \tan\vartheta = \frac{|\Gamma_\phi|}{\epsilon}. \tag{9.7}$$

The level splitting is $\omega_0 = E_{S^*} - E_S = 2R$. A gate drive $A_\epsilon \cos\Omega t\,\tau_z$ has the transverse component $A_\epsilon \sin\vartheta$ in the eigenbasis. A phase drive modulates $\Gamma_\phi = \Gamma\cos(\phi/2)$ and has the transverse component $\frac{A_\phi}{2}\Gamma|\sin(\phi_0/2)|\cos\vartheta$. The resonant Rabi splittings are therefore

$$\delta_{\text{gate}} = A_\epsilon|\sin\vartheta| = \frac{A_\epsilon|\Gamma_\phi|}{R}, \qquad \delta_{\text{phase}} = \frac{A_\phi\Gamma}{2}|\sin\frac{\phi_0}{2}||\cos\vartheta| = \frac{A_\phi\Gamma}{2}|\sin\frac{\phi_0}{2}|\frac{|\epsilon|}{R}. \tag{9.8}$$

The phase-drive splitting vanishes at $\epsilon = 0$ and the gate-drive splitting is largest there: the selection rule of Section 9.6 in its simplest form. For a junction with finite Δ, these expressions provide qualitative guidance; quantitative results use the numerically calculated matrix elements.

Caution

The large-gap model assumes that the drive is slow compared with Δ. A strong phase drive that is fast compared with the dot dynamics but slow compared with Δ ($\Omega \ll \Delta$) renormalizes Γ_ϕ by the time average $\langle\cos(\phi(t)/2)\rangle = J_0(A_\phi/2)\cos(\phi_0/2)$. A drive faster than the bandwidth instead renormalizes each hopping separately by $J_0(A_\phi/4)$, hence $\Gamma \to \Gamma J_0(A_\phi/4)^2$. The order of the large-gap and high-frequency limits therefore determines the effective coupling.

10 Numerical methods for driven problems

10.1 From a drive to harmonics

`PeriodicHamiltonian.from_parameters` evaluates the model constructor at N equally spaced times $t_j = jT/N$ and Fourier transforms every operator coefficient,

$$H_k = \frac{1}{N}\sum_{j=0}^{N-1} H(t_j)\,\mathrm{e}^{-2\pi \mathrm{i} jk/N}, \qquad 0 \le k \le \lceil N/2 \rceil - 1. \tag{10.1}$$

This is exact for Hamiltonians with no harmonics at or above $N/2$, including a monochromatic modulation of a parameter on which the Hamiltonian depends linearly. For the phase drive the Bessel functions decay faster than exponentially once $k > A_\phi/4$, so a modest N suffices. The construction is checked at the midpoints $t_{j+1/2}$, where the model is rebuilt and compared with the Fourier series. The largest ℓ_1 norm of the coefficient differences bounds the operator-norm error of the interpolated Hamiltonian and must stay below `sampling_tolerance`. The observables of the model, e.g. $\partial H/\partial\phi$, are sampled in the same way, since they too depend on time under a phase drive.

10.2 Sambe-space diagonalization

`solve_floquet` truncates Q in Equation (8.5) to $|m| \le M$ (option `floquet_cutoff`) and diagonalizes it. The many-body space in each block is either the full QP Fock space of the sector (`basis="fock"`) or the static basis of the K lowest eigenstates of the undriven Hamiltonian (`basis="eigen"`, K set by `basis_states`). In the static basis the harmonics become the $K \times K$ matrices $\langle a|H_k|b\rangle$ between the static eigenstates. The Sambe dimension is $(2M+1)d$, where d is the dimension of the Fock space of the sector or $d = K$. Small problems are diagonalized densely. Large Fock-space problems use shift-invert Arnoldi iterations (ARPACK) [124], with a sparse LU factorization of $Q - \sigma$ for each target quasienergy σ [125]; by default the targets are the static energies of the tracked states.

A rigorous error bound. Let v be a normalized eigenvector of the truncated matrix Q_M with eigenvalue λ, and embed it in the infinite Sambe space. The residual of the embedded vector has two parts: the window residual $r = \|(Q_M - \lambda)v\|$, which measures the eigensolver accuracy, and the *leakage* $\kappa = \|\sum_{m'} H_{m-m'} v_{m'}\|$ into the omitted blocks $|m| > M$. Because the infinite Sambe operator is self-adjoint, it has an eigenvalue within

$$|\varepsilon - \lambda| \le \sqrt{r^2 + \kappa^2} \tag{10.2}$$

of λ (Appendix A.2). This combined residual is reported as `residuals`; the window residual must stay below `residual_tolerance`. The bound is of first order: for an isolated quasienergy the actual error is typically of second order in κ, and often much smaller than the bound. In the static basis, `fock_residuals` evaluates the same residual for the Fock-space Sambe operator and thus tests the convergence in K.

Branches and tracking. Each Floquet state appears in many replicas (Section 8.2). The solver keeps one replica per state, the one whose harmonic centroid $\langle m \rangle$ is smallest in magnitude. It recognizes the other replicas by their quasienergy, shifted by a multiple of Ω, and by their overlap after a shift of the harmonic index; for degenerate multiplets it projects onto all retained states with that quasienergy. With `selection="tracked"` (the default), the lowest `states` static eigenstates are assigned to Floquet states by maximizing the total static weight $s_{\alpha a} = \sum_m |\langle a|u_{\alpha,m}\rangle|^2$; each assigned weight must exceed `tracking_threshold`. Near a resonance the eigenpairs closest to one shift-invert target can be replicas of the state assigned at another target. The solver therefore doubles the number of eigenpairs requested at that target until the corresponding static state is assigned, up to `max_eigenpairs_per_target`. With `selection="all"`, every Floquet state in the window is returned. Complete sets, needed for the sum rule of Chapter 11, require the dense solver, because shift-invert finds only the states near explicit `targets`. The reported quasienergy is placed on a definite branch:

- `branch="label"` (default for tracked states) chooses the replica in which the component on the assigned static state a has its harmonic centroid in $[-\frac{1}{2}, \frac{1}{2})$, so that $\varepsilon_\alpha \to E_a$ as the drive vanishes and ε_α varies continuously through a one-photon resonance;
- `branch="centroid"` (default for `selection="all"`) uses the replica with total centroid in $[-\frac{1}{2}, \frac{1}{2})$;
- `folded` gives every quasienergy in the zone $[c - \Omega/2, c + \Omega/2)$, $c =$`zone_center`.

Caution

At a resonance the dressed states are equal mixtures of two static states, and the labels may swap from one side of the resonance to the other. Plot both branches together, as in the rotating frame of Figure 13.1, to follow the complete resonant pair.

10.3 The one-period propagator

`floquet_propagator` integrates the Schrödinger equation over one period with $H(t) = \sum_k H_k e^{ik\Omega t}$, without a Floquet cutoff, and diagonalizes $U(T, 0)$. The integrator is the fourth-order commutator-free Magnus scheme [126–128] (Appendix A.4),

$$U(t+h,t) = e^{-ih(\alpha_1 H_1 + \alpha_2 H_2)}\, e^{-ih(\alpha_2 H_1 + \alpha_1 H_2)}, \qquad \alpha_{1,2} = \frac{3 \mp 2\sqrt{3}}{12}, \quad H_{1,2} = H\big(t + (\tfrac{1}{2} \mp \tfrac{\sqrt{3}}{6})h\big), \tag{10.3}$$

where h is the time step. The exponentials are evaluated by eigendecomposition, so that each step is exactly unitary. The eigenphases of $U(T, 0)$ give the folded quasienergies. The mean

energies (8.6), accumulated along a second propagation, select the central replica, and the Fourier transform of $|u(t)\rangle$ on the time grid gives the harmonics. With `step_check=True` the calculation is repeated with half the time step, and $|\varepsilon_h - \varepsilon_{h/2}|/15$ estimates the remaining error of the time stepping. The propagator approach is also used by QuTiP's Floquet module [129, 130]. In qdjj_solver it serves as an independent check of convergence with the Floquet cutoff and as an alternative method in a static basis.

10.4 The high-frequency expansion

For Ω large compared with the many-body spectral width, the Sambe blocks with $m \neq 0$ are far from the $m = 0$ block and can be eliminated perturbatively. The result is the static effective Hamiltonian H_{eff} introduced in Chapter 8, whose eigenvalues approximate the quasienergies. To second order in $1/\Omega$, the van Vleck form of this expansion [50, 51, 85, 97] reads (Appendix A.3)

$$H_{\text{eff}} = H_0 + \frac{1}{\Omega}\sum_{m\geq 1}\frac{[H_m, H_{-m}]}{m} + \frac{1}{\Omega^2}\Big(\sum_{m\neq 0}\frac{[[H_{-m}, H_0], H_m]}{2m^2} + \sum_{m\neq 0}\sum_{m'\neq 0,m}\frac{[[H_{-m'}, H_{m'-m}], H_m]}{3mm'}\Big). \tag{10.4}$$

The first-order term vanishes when every H_k commutes with $H_{-k} = H_k^\dagger$. This holds for any drive that becomes even in time after a shift of the time origin, such as a single-parameter cosine with any phase θ, for which $H_k = \mathrm{e}^{\mathrm{i}k\theta} g_k$ with Hermitian g_k. A finite first-order term requires, for example, several parameters driven with relative phases. The commutators are evaluated with the full fermionic operators, before any QP truncation. The result is an ordinary `Hamiltonian` in the same coordinates (`periodic.van_vleck(order)`), which both the QP and the DMRG solver can solve. The error at order n scales as $\Omega^{-(n+1)}$ (Figure 14.1). Because the bath bandwidth enters the many-body spectral width, the expansion serves as a check for small models and as a conceptual tool in the high-frequency regime. Treat subgap resonances at $\Omega \sim \Delta$ with Sambe diagonalization or the propagator.

10.5 The rotating-wave model

Near a resonance only a few blocks of Q matter. `rwa_model(periodic, states, photons)` restricts Q to the pairs $|a_i, n_i\rangle$ of a static state a_i and a photon number n_i,

$$Q^{\text{RWA}}_{ij} = \left(H_{n_i - n_j}\right)_{a_i a_j} + n_i \Omega\, \delta_{ij}, \tag{10.5}$$

with matrix elements in the static eigenbasis. The photon numbers are chosen so that the diagonal entries $E_{a_i} + n_i\Omega$ are nearly degenerate. For example, absorption from a to b with $E_b - E_a \approx \Omega$ uses `states=[a, b]` and `photons=[0, -1]`. At resonance the splitting is $2|(H_{n_a - n_b})_{ab}|$. The model neglects the counter-rotating terms (Bloch–Siegert shift) and the AC Stark shifts from all other states, both of second order in the drive. It is exact for a two-level system with a circularly polarized drive.

Table 10.1: Methods for Floquet quasienergies in qdjj_solver.

Method	Controlled by	Use for
Sambe, Fock basis	M, QP cutoff, bath	reference results; moderate Fock dimensions; shift-invert for tracked states
Sambe, static basis	M, K	large Fock spaces, scans over Ω or amplitude; check `fock_residuals`
Propagator	time steps, basis	independent check without Floquet cutoff; strong slow drives
Van Vleck	order in $1/\Omega$	Ω above the many-body width; effective Hamiltonians, DMRG
RWA	chosen states	interpretation of resonances, Rabi splittings

10.6 Choosing a method

Convergence must be checked separately with respect to the Floquet cutoff M, the size K of the static basis, the QP cutoff, the bath, the number of drive samples and, for the propagator, the number of time steps. Chapter 15 works through each of them.

10.7 Validation

The driven solvers are checked against independent results:

- propagation of the exact $H(t)$ of a phase- and gate-driven junction in the physical electron basis, with a different Magnus integrator and without Fourier series; it agrees with the QP propagator and the Fock-space Sambe results to 10^{-8};
- the exactly solvable circularly driven two-level system, for Sambe, propagator, RWA and the analytic van Vleck operators;
- Bessel-function harmonic weights of a gate-driven isolated dot (Chapter 12) and Jacobi–Anger harmonics of the phase drive;
- the gauge identity (9.3) between a phase drive and a level drive;
- the $\Omega^{-(n+1)}$ error scaling of the van Vleck expansion;
- the Rabi splitting at an S–S^* resonance against the RWA and the static matrix element.

11 Probing the driven junction

A driven junction can be probed by a second, weak perturbation: a probe tone in two-tone spectroscopy, a tunnelling contact, or a spin-resonance coil. This chapter describes the transitions that such a probe induces between Floquet states, and how qdjj_solver computes their positions and strengths.

11.1 The Floquet golden rule

Add to the driven Hamiltonian a weak probe $\lambda X(t)\cos\omega_p t$, where $X(t)$ is an operator, possibly modulated by the drive, with harmonics $X(t)=\sum_k X_k \mathrm{e}^{\mathrm{i}k\Omega t}$. Between Floquet states the probe matrix element oscillates at a ladder of frequencies,

$$\langle\psi_\alpha(t)|X(t)|\psi_\beta(t)\rangle=\sum_q X^{(q)}_{\alpha\beta}\,\mathrm{e}^{\mathrm{i}(\varepsilon_\alpha-\varepsilon_\beta+q\Omega)t},\qquad X^{(q)}_{\alpha\beta}=\sum_{m,k}\langle u_{\alpha,m+k-q}|X_k|u_{\beta,m}\rangle. \tag{11.1}$$

First-order perturbation theory, averaged over many drive periods, gives the transition rate from β to α,

$$\Gamma_{\beta\to\alpha}(\omega_p)=\frac{\pi\lambda^2}{2}\sum_q|X^{(q)}_{\alpha\beta}|^2\Big[\delta\big(\omega_p-\omega^{(q)}_{\alpha\beta}\big)+\delta\big(\omega_p+\omega^{(q)}_{\alpha\beta}\big)\Big],\qquad \omega^{(q)}_{\alpha\beta}=\varepsilon_\alpha-\varepsilon_\beta+q\Omega, \tag{11.2}$$

the Floquet generalization of Fermi's golden rule [77, 78]. Each pair of Floquet states contributes a ladder of lines separated by the drive frequency. In the photon picture of Section 8.4, q counts the drive photons exchanged during the transition, and $|X^{(q)}_{\alpha\beta}|^2$ is the strength of the q-photon line. A line at a positive frequency absorbs a probe quantum; a line at a negative frequency corresponds to stimulated emission into the probe.

The set of lines is a property of the physical Floquet states. Choosing another replica for the final state, $(\varepsilon_\alpha+\ell\Omega, u_{\alpha,m-\ell})$, relabels $X^{(q)}\to X^{(q+\ell)}$ but leaves every line frequency and strength unchanged. For a Hermitian probe, $\overline{X^{(q)}_{\alpha\beta}}=X^{(-q)}_{\beta\alpha}$. Without a drive only $q=0$ survives, and $X^{(0)}$ reduces to the static matrix element.

Sum rule. Parseval's theorem and the completeness of the Floquet states give

$$\sum_\alpha\sum_q|X^{(q)}_{\alpha\beta}|^2=\frac{1}{T}\int_0^T\mathrm{d}t\,\langle\psi_\beta(t)|X(t)^\dagger X(t)|\psi_\beta(t)\rangle, \tag{11.3}$$

the time-averaged weight of the state $X(t)|\psi_\beta\rangle$. The code reports both sides, `captured` and `total`. Their ratio, `completeness`, is the fraction of the spectral weight accounted for by the computed final states. A complete set (`selection="all"`) in the full Fock space of the destination sector saturates the sum rule.

11.2 Probes

Probes are specified by name:

- `current`, the phase derivative $\partial H/\partial\phi$, for a flux or phase probe;
- `charge`, the dot occupation n_d, for a gate probe;
- `spin_x`, `spin_y`, `spin_z` and `spin_plus`, `spin_minus`, for spin resonance;
- `d_up`, `d_dn` and their adjoints `d_up_dagger`, `d_dn_dagger`, for tunnelling spectroscopy.

Any other named model observable may also be used. Two physical distinctions are important.

- *Time-dependent probes.* A phase drive changes the current operator itself, so the probe has harmonics. qdjj_solver samples the observables together with the Hamiltonian and uses these harmonics. A probe given as an explicit operator is treated as time independent.
- *Tunnelling probes* change the fermion parity and connect Floquet states of different sectors under the same drive. With $S_X(\omega)$ the line spectrum of the probe X (defined below), the electron-addition spectrum is $A^+(\omega) = S_{d^\dagger}(\omega)$ and the electron-removal spectrum is $A^-(\omega) = S_d(-\omega)$, as for the static spectral function.

11.3 Initial states, degeneracies and line shapes

The observed lines depend on the populations of the Floquet states. Determining these populations requires a model of relaxation through the environment, which is planned. At present, spectra are computed for explicitly specified initial states and weights. The default is the dressed continuation of the static ground state (`dressed_state(0)`).

Within a degenerate multiplet the Floquet states can be unitarily rotated. Before constructing the line spectrum, qdjj_solver therefore distributes each initial weight uniformly over its degenerate group and sums the strengths of degenerate final states, which makes the lines independent of the basis chosen inside a multiplet. Terms between states of one group at $q = 0$ are expectation values and are omitted from the line spectrum. Terms of one group with $q \neq 0$ are *elastic* lines at $q\Omega$: the probe exchanges energy with the drive without changing the state. They are kept.

Each line l, at frequency $\omega_l = \omega^{(q)}_{\alpha\beta}$, has the strength $s_l = p_\beta |X^{(q)}_{\alpha\beta}|^2$, where p_β is the weight of the initial state. The lines are broadened with Lorentzian or Gaussian shapes L of half width at half maximum w, which gives the spectrum $S(\omega) = \sum_l s_l\, L(\omega - \omega_l)$ (`kind="signed"`, the default). `kind="rate"` returns $S(\omega) + S(-\omega)$, which is proportional to the rate (11.2) at the probe frequency $\omega > 0$. `kind="net"` returns $S(\omega) - S(-\omega)$, absorption minus stimulated emission, in which the elastic lines cancel. Lines into the discretized continuum need a width larger than the level spacing; a proper treatment of the continuum is planned.

In the code

```
options = dict(floquet_cutoff=6, selection="all", method="dense")
states = solve_floquet(periodic, 2, Sector(0, 0), options)
table = states.matrix_elements("charge")              # FloquetTransitions
lines = table.lines(initial=states.dressed_state(0))   # SpectralLines
rate = lines.spectrum(omega, width=.002, kind="rate")
odd = solve_floquet(periodic, 2, Sector(1, 1), dict(floquet_cutoff=6, states=1)
    )
removal = states.matrix_elements("d_up", odd)         # odd state -> even
    states
```

For the junction of Chapter 7, the complete even set needs a dense Sambe matrix of dimension 13×546, which takes a few minutes of computing time; `basis="eigen"` reduces the cost. The two sets of states must belong to the same drive and must treat the c-number terms of Section 8.5 in the same way; their sectors, QP cutoffs, bases and methods may differ. Static eigenstates also provide `matrix_elements`.

User manual: *Floquet calculations* (`docs/floquet.md`).

11.4 Computing the harmonics

Equation (11.1) is a Fourier coefficient of the mode matrix element,

$$X^{(q)}_{\alpha\beta} = \frac{1}{T}\int_0^T \mathrm{d}t\, \mathrm{e}^{-\mathrm{i}q\Omega t}\, \langle u_\alpha(t)|X(t)|u_\beta(t)\rangle. \tag{11.4}$$

qdjj_solver first forms the harmonics $|v_{\beta,m}\rangle = \sum_k X_k|u_{\beta,m-k}\rangle$ of $X(t)|u_\beta(t)\rangle$ in the Fock basis of the destination sector. Within one basis this is a sparse matrix–vector product; between different sectors or cutoffs, the operator acts between the two QP-truncated spaces. The norm $\sum_m \|v_{\beta,m}\|^2$ is the right-hand side of the sum rule (11.3). The overlap $\langle u_\alpha(t)|v_\beta(t)\rangle$ is a trigonometric polynomial with a finite number N of harmonics, so N equally spaced samples and a discrete Fourier transform give every $X^{(q)}$ exactly, without aliasing. The memory is dominated by the vectors $v_{\beta,m}$; the argument `max_memory_gib` limits it, and `ket_states` restricts the initial states.

11.5 Mollow triplet and Autler–Townes doublet

A resonant pump dresses two levels a and b into the hybrids $|\pm\rangle$, separated by the Rabi splitting δ (Chapter 13). The probe response depends on whether it acts on the pumped transition itself or on a transition to a third level.

- *Probe of the pumped transition, from a dressed state.* The probe connects $|\pm\rangle$ with their own replicas and with each other. A system in the lower dressed state shows lines at three probe frequencies near the pump: absorption at $\Omega + \delta$, stimulated emission at $\Omega - \delta$, and two elastic lines at the line frequencies $\pm\Omega$; in the upper dressed state, absorption and emission exchange places. At resonance each of these four lines carries a quarter of the static strength $|X_{ab}|^2$, so in the rate the central line is twice as strong as the sidebands.

This is the probe counterpart of the Mollow triplet of resonance fluorescence [88, 131, 132]. The net absorption is negative at $\Omega - \delta$: a dressed two-level system amplifies a probe at this frequency [133].

- *Probe of a transition from a spectator level c.* The single line $c \to a$ splits into two lines at $\pm\delta/2$ around its undriven position, each with half the strength: the Autler–Townes doublet [89].

Both were observed together in a pumped superconducting qubit [134]. They appear in Chapter 18 for the pair transition of the junction, and in Section 20.3 for the spin doublet.

Part III

Worked examples

12 Example: the gate-driven isolated dot

The first example is an exactly solvable, isolated normal dot. It introduces three concepts used throughout the following chapters: quasienergies, harmonic weights (photon sidebands) and the Floquet zone.

12.1 Exact solution

Consider the isolated impurity (3.1) with a gate drive,

$$H(t) = H_d(\epsilon_0) + A\cos(\Omega t)\,(n_d - 1). \tag{12.1}$$

Every Fock state $|n\rangle$ of the dot, with charge $n \in \{0, 1, 2\}$, is an eigenstate at every time, so its time evolution consists only of a phase factor,

$$|\psi_n(t)\rangle = \mathrm{e}^{-\mathrm{i}E_n t}\,\mathrm{e}^{-\mathrm{i}q_n (A/\Omega)\sin\Omega t}|n\rangle, \qquad q_n = n - 1. \tag{12.2}$$

Comparing with Equation (8.2), the quasienergy is the static energy, $\varepsilon_n = E_n$, for every drive amplitude: this purely diagonal, zero-mean modulation preserves the time-averaged energy. The Floquet mode is the periodic phase factor. With the generating function of the Bessel functions, $\mathrm{e}^{-\mathrm{i}z\sin\vartheta} = \sum_m J_m(z)\mathrm{e}^{-\mathrm{i}m\vartheta}$,

$$|u_n(t)\rangle = \sum_m \mathrm{e}^{\mathrm{i}m\Omega t}(-1)^m J_m\!\left(\frac{q_n A}{\Omega}\right)|n\rangle, \qquad \|u_{n,m}\|^2 = J_m^2\!\left(\frac{q_n A}{\Omega}\right). \tag{12.3}$$

The harmonic weights depend only on the *modulation index* $q_n A/\Omega$, the ratio between the amplitude of the level oscillation and the photon energy. Figure 12.1(a) compares them with the Sambe results.

Physical picture

$J_m^2(A/\Omega)$ is the probability that a driven level has exchanged m photons with the field. An electron that tunnels from a lead into such a level can do so at any of the energies $E_n + m\Omega$, so the tunnelling spectrum acquires sidebands with weights J_m^2. This is the Tien–Gordon theory of photon-assisted tunnelling, first formulated for superconducting tunnel junctions [135, 136] and observed in quantum dots [110–112]. For a modulation index of 2.405, the first zero of J_0, the central line disappears.

12.2 Gauge and the meaning of the charge

Only charge *differences* enter a physical transition: tunnelling from $|n\rangle$ to $|n+1\rangle$ involves the relative modulation index $(q_{n+1} - q_n)A/\Omega = A/\Omega$. The absolute weights (12.3) depend on the constant in H_d. Writing the drive as $A\cos(\Omega t)\, n_d$ instead would assign $q_n = n$, and the empty dot would have no sidebands at all. The two forms differ by the c-number $A\cos\Omega t$, a gauge transformation (Section 8.5) that leaves the quasienergies unchanged. qdjj_solver keeps the constants of the model by default, so that $q_n = n - 1$ is measured from half filling; this centres the sidebands and minimizes the Floquet cutoff needed for convergence. The option `drop_scalar_harmonics=True` removes the oscillating c-number terms, which here gives the second form.

12.3 Floquet zones and replicas

Figure 12.1(b) shows the replicas $\varepsilon_n + m\Omega$ of the empty and doubly occupied states as a function of Ω at fixed amplitude, with line intensity proportional to $J_m^2(A/\Omega)$. All replicas are equally valid quasienergies; the shaded first zone $|\varepsilon| < \Omega/2$ is one choice of representatives. At low frequency the modulation index is large, many sidebands carry weight and the replicas fan out; at high frequency the weight concentrates in $m = 0$. Replicas of different states cross freely: without a coupling between the states, crossings in the Floquet spectrum are exact.

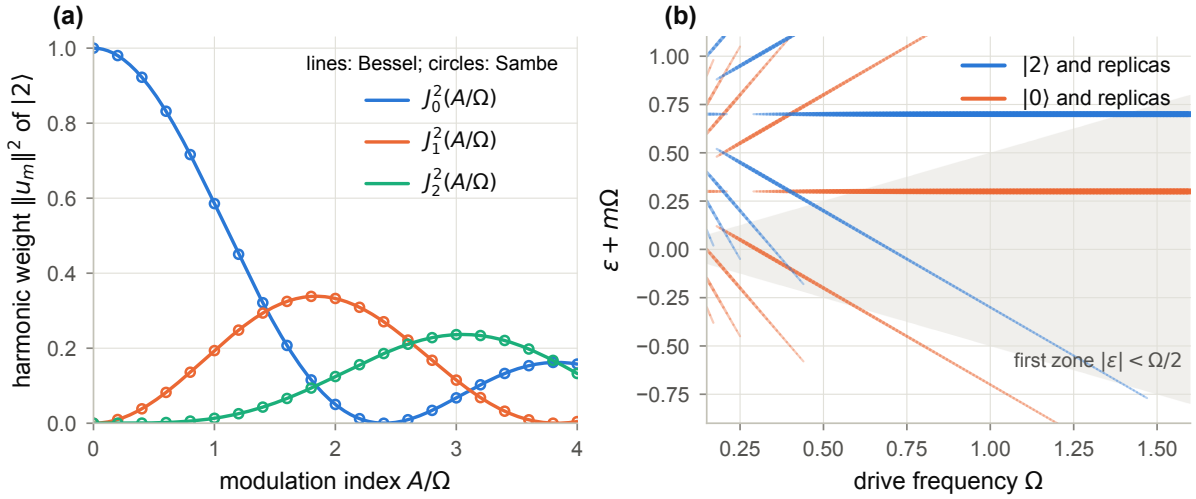


Figure 12.1: Gate-driven isolated dot, $U = 1$, $\epsilon_0 = 0.2$. (a) Harmonic weights of the doubly occupied state versus the modulation index A/Ω; circles are Sambe results, lines the Bessel functions (12.3). (b) Replicas $\varepsilon + m\Omega$ of $|0\rangle$ and $|2\rangle$ versus Ω for $A = 0.6$; line opacity and width indicate the harmonic weight. The shaded region is the first Floquet zone.

12.4 In the code

```
import numpy as np
from qdjj_solver import Hamiltonian, Impurity, PeriodicHamiltonian, Sector
```

```
from qdjj_solver.qp_solver import solve_floquet

def dot(detuning):
    impurity = Impurity.anderson(1., detuning)
    return Hamiltonian(impurity.operator, 2, (1, -1), observables=impurity.
    observables)

A, omega = .6, 1.
periodic = PeriodicHamiltonian.from_callable(lambda t: dot(.2 + A*np.cos(omega*t)),
     omega,
                                             assume_fixed_coordinates=True)
states = solve_floquet(periodic, 0, Sector(0, 0), dict(floquet_cutoff=12, states=2)
    )
print(states.quasienergies)            # 0.3 and 0.7: the static energies of |0>
    and |2>
print(states.harmonic_weights[:, states.harmonic_indices == 0])   # J_0(A/omega)^2
    for both
```

The isolated dot is constructed directly in fixed physical-electron coordinates. The explicit assertion `assume_fixed_coordinates=True` (Section 9.5) allows the code to compare the samples through their mode labels. Since the only harmonics of this drive are H_0 and $H_{\pm 1}$, any number of samples $N \geq 3$ reproduces $H(t)$ exactly.

Tutorial: *The gate-driven isolated dot* (`examples/02_driven_dot`).

13 Example: the proximitized dot as a driven two-level system

The even sector of the proximitized dot, Equation (9.7), is a two-level system: the empty and doubly occupied dot, coupled by the induced pairing Γ_ϕ. It is the superconducting analogue of the driven atom and of the charge qubit [32, 36, 137, 138], and exhibits characteristic resonance phenomena of driven systems: Rabi splitting, Autler–Townes doublets, the Bloch–Siegert shift and multiphoton resonances. The model is built directly as a `Hamiltonian`,

```
from qdjj_solver import Hamiltonian, Impurity, PeriodicHamiltonian, Sector, create,
     hermitian_pair
from qdjj_solver.qp_solver import rwa_model, solve_floquet

def proximitized(detuning, pairing, u=1.):
    impurity = Impurity.anderson(u, detuning)
    operator = impurity.operator + hermitian_pair(-pairing*create(0)*create(1))
    return Hamiltonian(operator, 2, (1, -1), observables=impurity.observables)

def driven(eps0, pairing, A, omega):
    return PeriodicHamiltonian.from_callable(lambda t: proximitized(eps0 + A*np.cos
    (omega*t), pairing),
                                             omega, assume_fixed_coordinates=True)
```

13.1 Rabi splitting and the rotating-wave approximation

At $\epsilon_0 = 0$ the eigenstates are the bonding and antibonding singlets $(|0\rangle \pm |2\rangle)/\sqrt{2}$, split by $\omega_0 = 2\Gamma_\phi$, and the gate drive $A\cos(\Omega t)\,\tau_z$ is purely transverse: it has no diagonal matrix elements in the eigenbasis. In the Sambe space, the state $|S, 0\rangle$ (no photon exchanged) is resonant with $|S^*, -1\rangle$ (one photon absorbed) when $\Omega = \omega_0$. Keeping only these two blocks gives the rotating-wave Hamiltonian

$$Q^{\mathrm{RWA}} = \begin{pmatrix} E_S & A/2 \\ A/2 & E_{S^*} - \Omega \end{pmatrix}, \qquad \varepsilon_\pm = \frac{E_S + E_{S^*} - \Omega}{2} \pm \frac{1}{2}\sqrt{(\omega_0 - \Omega)^2 + A^2}. \tag{13.1}$$

At resonance the dressed states are equal mixtures of S and S^*, split by the Rabi frequency A; away from resonance the splitting increases and the dressed states approach the bare ones. Figure 13.1(a) compares this with the full Sambe calculation in the rotating frame, where the replica $\varepsilon_{S^*} - \Omega$ is plotted together with ε_S: the familiar Autler–Townes avoided crossing [87, 89].

The Bloch–Siegert shift. The RWA neglects the counter-rotating coupling of $|S,0\rangle$ to $|S^*,+1\rangle$ and of $|S^*,-1\rangle$ to $|S,-2\rangle$, which are detuned by about $2\omega_0$. To second order they shift the two resonant levels by $\mp(A/2)^2/2\omega_0$, which moves the resonance to

$$\Omega_{\mathrm{res}} = \omega_0 + \frac{A^2}{4\omega_0} + O(A^4), \tag{13.2}$$

the Bloch–Siegert shift [82, 91]. Figure 13.1(b,c) identifies the resonance with the minimum splitting of the dressed pair and shows that this splitting remains close to A while the resonance shifts as predicted; deviations appear when A becomes comparable to ω_0. Other definitions of the resonance, such as equal mixing of S and S^*, agree to order A^2 and differ at order A^4.

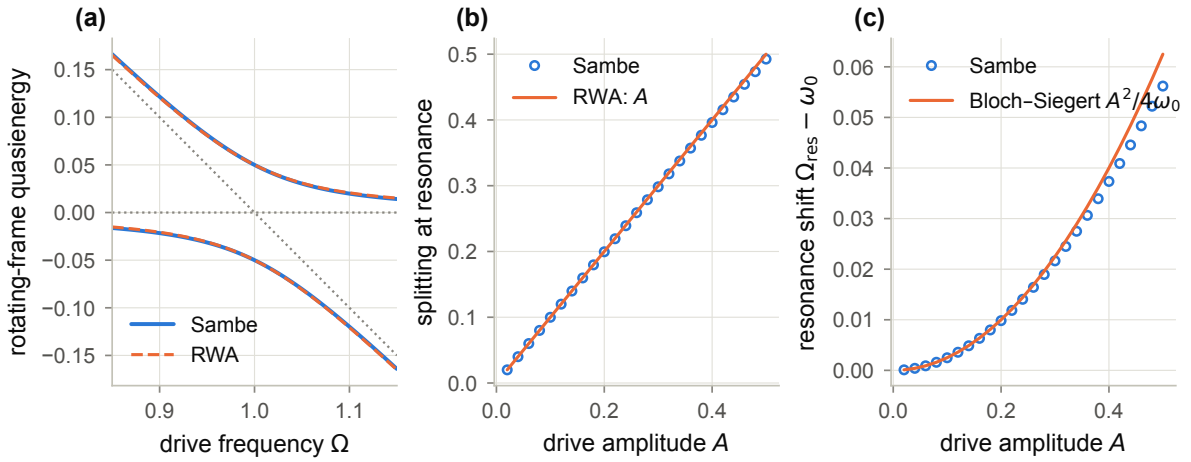


Figure 13.1: Proximitized dot at $\epsilon_0 = 0$, $\Gamma_\phi = 0.5$ ($\omega_0 = 1$), driven by the gate. (a) Quasienergies ε_S and $\varepsilon_{S^*} - \Omega$ in the rotating frame near the one-photon resonance for $A = 0.1$: Sambe (solid) and RWA $\varepsilon_\pm$ (dashed); dotted lines are the undriven levels E_S and $E_{S^*} - \Omega$. (b) Splitting at the resonance versus amplitude. (c) Shift of the resonance; the line is the Bloch–Siegert result (13.2).

13.2 Strong driving and multiphoton resonances

Now let the detuning be large, $\epsilon_0 \gg \Gamma_\phi$, and the drive strong, $A \gtrsim \Omega$. The diabatic states $|0\rangle$ and $|2\rangle$ are then nearly eigenstates, separated by $2\epsilon(t)$, and the weak pairing induces transitions. In the interaction picture with respect to the diagonal part, the pairing term acquires the phase factor

$$\exp\Big[2\mathrm{i}\int_0^t \epsilon(t')\,\mathrm{d}t'\Big] = \mathrm{e}^{2\mathrm{i}\epsilon_0 t}\sum_k J_k\Big(\frac{2A}{\Omega}\Big)\,\mathrm{e}^{\mathrm{i}k\Omega t}. \tag{13.3}$$

At the k-photon resonance $2\epsilon_0 = k\Omega$ one term is static and the others oscillate. Averaging over the fast oscillations leaves an effective coupling $\Gamma_\phi J_k(2A/\Omega)$, hence the splitting

$$\delta_k = 2\Gamma_\phi |J_k\Big(\frac{2A}{\Omega}\Big)| \qquad (\Gamma_\phi \ll \Omega). \tag{13.4}$$

The resonances are modulated by Bessel functions of the modulation index; at the zeros of J_k the k-photon resonance disappears and the two levels cross: *coherent destruction of tunnelling* [98,

139]. Scanning ϵ_0 and A maps out the Landau–Zener–Stückelberg interference pattern measured in superconducting qubits and quantum dots [100–102, 140].

Figure 13.2(a) compares the Sambe splittings with (13.4) for $k = 1, 2, 3$; the small offsets at $A \to 0$ are the $O(\Gamma_\phi^2/\Omega)$ level shifts that detune the resonance. Panel (b) shows the quasienergy splitting as a function of the detuning at the first zero of $J_2(2A/\Omega)$: the $k = 1, 3, 4$ resonances show avoided crossings of the predicted size, while the $k = 2$ one has collapsed.

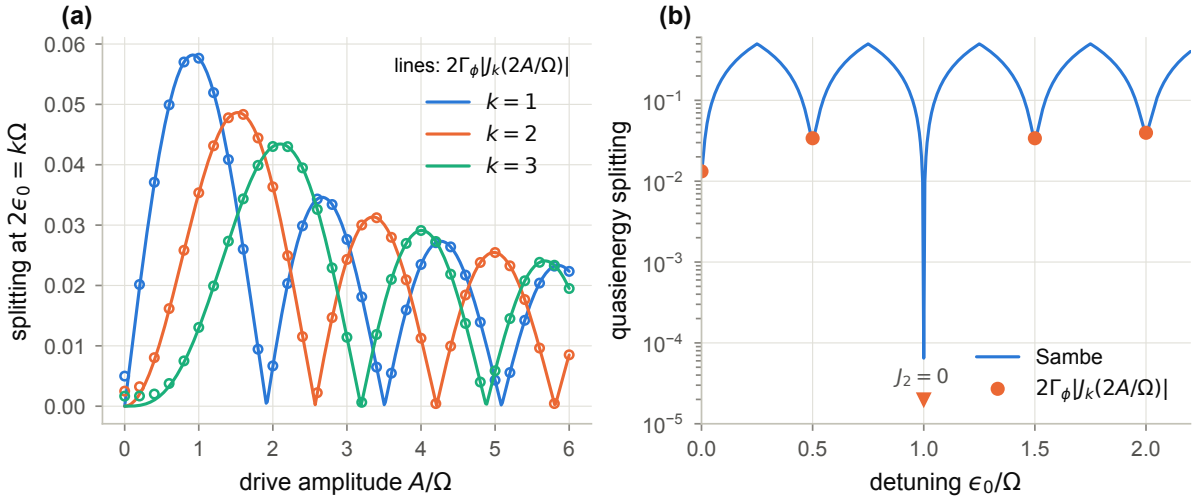


Figure 13.2: Strongly driven proximitized dot, $\Gamma_\phi = 0.05$, $\Omega = 1$. (a) Splitting at the k-photon resonance $2\epsilon_0 = k\Omega$ versus amplitude; circles are Sambe results, lines (13.4). (b) Folded quasienergy splitting versus detuning at $A = j_{2,1}\Omega/2$, where $j_{2,1} \approx 5.136$ is the first zero of J_2; dots mark $2\Gamma_\phi|J_k(2A/\Omega)|$ at $\epsilon_0 = k\Omega/2$, and the triangle the vanishing value for $k = 2$.

In the code

```
periodic = driven(0., .5, .1, 1.)                    # eps0, Gamma_phi, A,
    omega
exact = solve_floquet(periodic, 0, Sector(0, 0), dict(floquet_cutoff=12, states
    =2))
rwa = rwa_model(periodic, states=[0, 1], photons=[0, -1],
                cutoff=0, sector=Sector(0, 0))
```

Strong-drive calculations require a Floquet cutoff well above the modulation index A/Ω of the dot states; the residual bound (10.2) signals an insufficient cutoff.

User manual: *Floquet calculations* (`docs/floquet.md`).

Tutorial: *The proximitized dot as a driven two-level system* (`examples/03_two_level_system`).

14 Example: the high-frequency limit

When the drive is faster than every internal process, the system responds to a time-averaged, renormalized Hamiltonian. This limit is the basis of Floquet engineering [50–52], and it is a direct test of the van Vleck expansion of Section 10.4.

14.1 Accuracy of the van Vleck expansion

Figure 14.1(a) compares the eigenvalues of the van Vleck Hamiltonians of order $n = 0$, 1 and 2 with exact Sambe quasienergies for a single-lead model driven simultaneously through its phase and level energy, with a phase offset between the two drives. The error decreases as $\Omega^{-(n+1)}$, as the expansion predicts [85, 97]. With a relative phase the drive is not even in time, $H_{-k} \neq H_k$, and the first-order term $[H_1, H_{-1}]/\Omega$ is finite. For a single-parameter cosine drive it vanishes and the zeroth-order result is already accurate to $O(\Omega^{-2})$.

14.2 Renormalized coupling and coherent destruction of tunnelling

For a phase drive with Ω larger than the many-body spectral width, the zeroth-order Hamiltonian is H_0 of Equation (9.4): the junction with

$$\Gamma \to \Gamma_{\text{eff}} = \Gamma J_0\left(\frac{A}{4}\right)^2 . \tag{14.1}$$

Each tunnelling amplitude carries the phase factor $\mathrm{e}^{\mp \mathrm{i}\phi(t)/4}$. Its time average is $J_0(A/4)\,\mathrm{e}^{\mp \mathrm{i}\phi_0/4}$, so the hybridization, quadratic in the tunnelling amplitude, is reduced by $J_0(A/4)^2$. As A increases, the dot decouples progressively from the leads; at the first zero of J_0, $A = 4 \times 2.405 \approx 9.62$, it is isolated to leading order in $1/\Omega$. This is the junction version of dynamical localization [99, 141, 142] and of coherent destruction of tunnelling [98, 143].

Figure 14.1(b) follows the quasienergies of the lowest singlets and of the doublet for $U = 1$, $\Gamma = 0.8$, $\epsilon = 0$ and $\Omega = 40$, together with the static energies of the junction with the renormalized coupling (14.1). The undriven ground state is a singlet. As Γ_{eff} decreases, the doublet becomes the lowest dressed state near $A \approx 3.8$: the drive induces a level crossing between the dressed singlet and doublet, a dynamical analogue of the 0–π transition. At the zero of J_0 the time-averaged coupling vanishes and the atomic energies are recovered to leading order, $\varepsilon_{S,S^*} = U/2$ and $\varepsilon_D = 0$. The remaining small deviations, which also split S and S^*, are the $O(\Omega^{-2})$ corrections of the higher harmonics $J_k(A/4)$, $k \geq 1$; the second-order van Vleck Hamiltonian reproduces them.

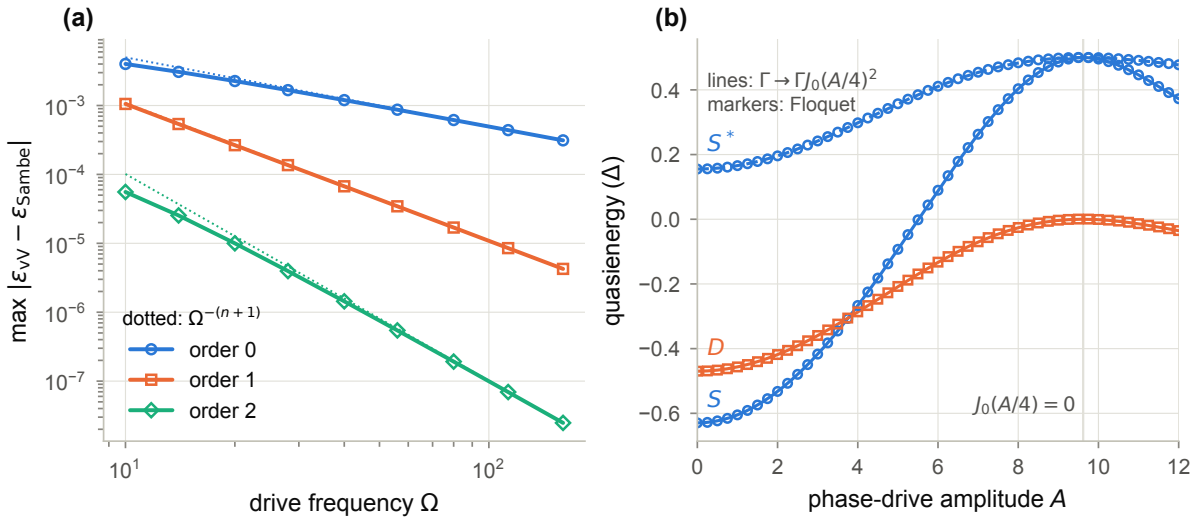


Figure 14.1: High-frequency limit. (a) Maximum deviation between the eigenvalues of the van Vleck Hamiltonian of order n and exact Sambe quasienergies, for a single-lead model with combined phase and level drive; dotted lines are $\Omega^{-(n+1)}$. (b) Quasienergies of the phase-driven junction ($U = 1$, $\Gamma = 0.8$, $\epsilon = 0$, $\phi_0 = 0.8$, one bath level pair per lead with $D = 2$, $\Omega = 40$) versus drive amplitude. Markers are Floquet results, lines the static energies with $\Gamma \to \Gamma J_0(A/4)^2$.

Caution

The renormalization (14.1) describes the formal limit with Ω above the full reservoir bandwidth. Microwave experiments on superconducting junctions typically operate below that bandwidth. For $\Gamma, |\epsilon| \ll \Omega \ll \Delta$ the leads follow the drive adiabatically, and the relevant time average is that of the induced pairing $\Gamma_\phi(t)$, $\Gamma\cos(\phi_0/2) \to \Gamma J_0(A/2)\cos(\phi_0/2)$ (Section 9.7). The order of limits matters, and the van Vleck expansion of the full model is a reliable approximation only in the first regime.

In the code

```
fast = dict(bath=cosh_grid(pairs=1, bandwidth=2.), u=1., gamma=.8, phi=.8,
    detuning=0.,
            symmetry=False, compress=False)
periodic = PeriodicHamiltonian.from_parameters(reference_model, fast,
                                               ParameterDrive.cosine("phi", 6.),
     omega=40.)
effective = periodic.van_vleck(2)                          # a static Hamiltonian
energies = solve(effective, 2, Sector(1, 1)).energies     # dressed doublet,
    panel (b) of the figure
```

The effective Hamiltonian keeps the coordinates of the model, so it can be compared with static calculations and solved by DMRG.

User manual: *Floquet calculations* (`docs/floquet.md`).

Tutorial: *The high-frequency limit* (`examples/04_high_frequency`).

15 Example: numerical convergence

A Floquet calculation of the junction involves six independent approximations: the Floquet cutoff M, the static basis size K (if used), the QP cutoff, the bath discretization, the number of drive samples and, for the propagator, the number of time steps. This chapter studies the Floquet cutoff, the static basis and the bath for the phase-driven reference junction at QP cutoff 2; convergence with the QP cutoff must be checked as for the static problem (Section 6.3). The sampling and the time steps are checked by the midpoint test of Section 10.1 and the step-doubling estimate of Section 10.3.

15.1 The Floquet cutoff

Figure 15.1(a) shows the error of the tracked S and S^* quasienergies for a strong phase drive, $A = 1.5$ at $\Omega = 0.45$, as a function of M, together with the rigorous bound (10.2). The error decreases exponentially, by one to two orders of magnitude per harmonic, because the harmonics of the drive decay like Bessel functions. The bound always lies above the error, which is roughly the square of the bound, as expected for an isolated eigenvalue. The bound is conservative and can be used as a stopping criterion. The weight in the outermost blocks, `boundary_weights`, decreases at the same rate.

15.2 The static basis

In the static basis the many-body space is truncated to the K lowest undriven eigenstates. Figure 15.1(b) compares the tracked quasienergies with those of the full Fock space at QP cutoff 2 (dimension 546) for a weaker drive. The error is about 10^{-3} already for $K \approx 10$ and then decreases only slowly; it falls below 10^{-4} when K approaches the full dimension. The reason is physical. The phase drive couples the subgap states to quasiparticle excitations at all energies up to the bandwidth $D = 10$, and each contributes a small AC Stark shift (8.10). The static basis treats couplings among the retained states exactly; recovering the accumulated virtual contributions requires sufficiently many off-resonant states. `fock_residuals` provides a conservative error bound. For quantitative AC Stark shifts use the Fock basis; for resonances, splittings and scans the static basis is efficient.

15.3 The discretized continuum

Figure 15.1(c,d) follows the dressed singlet across the one-photon threshold $\Omega = E_D + \Delta - E_S \approx 1.10$, above which its first replica lies in the continuum, for baths with two, four and eight level

pairs per lead. Below the threshold the AC Stark shifts obtained with the three baths agree within 2%, and the calculation is converged in the bath. The exceptions are a few narrow avoided crossings at two-photon resonances, $2\Omega = E_a - E_S$, with discrete continuum levels a; like the one-photon crossings above the threshold, they move with the bath. Above the threshold, the dressed singlet shows a narrow avoided crossing, with a dip of its static weight to about one half, wherever a replica of a discrete continuum level crosses it. The positions of these crossings differ from bath to bath: they are discretization artefacts (Section 8.7). In the continuum limit they merge into a finite lifetime of the dressed bound state, set by the rate at which the drive excites quasiparticles out of it.

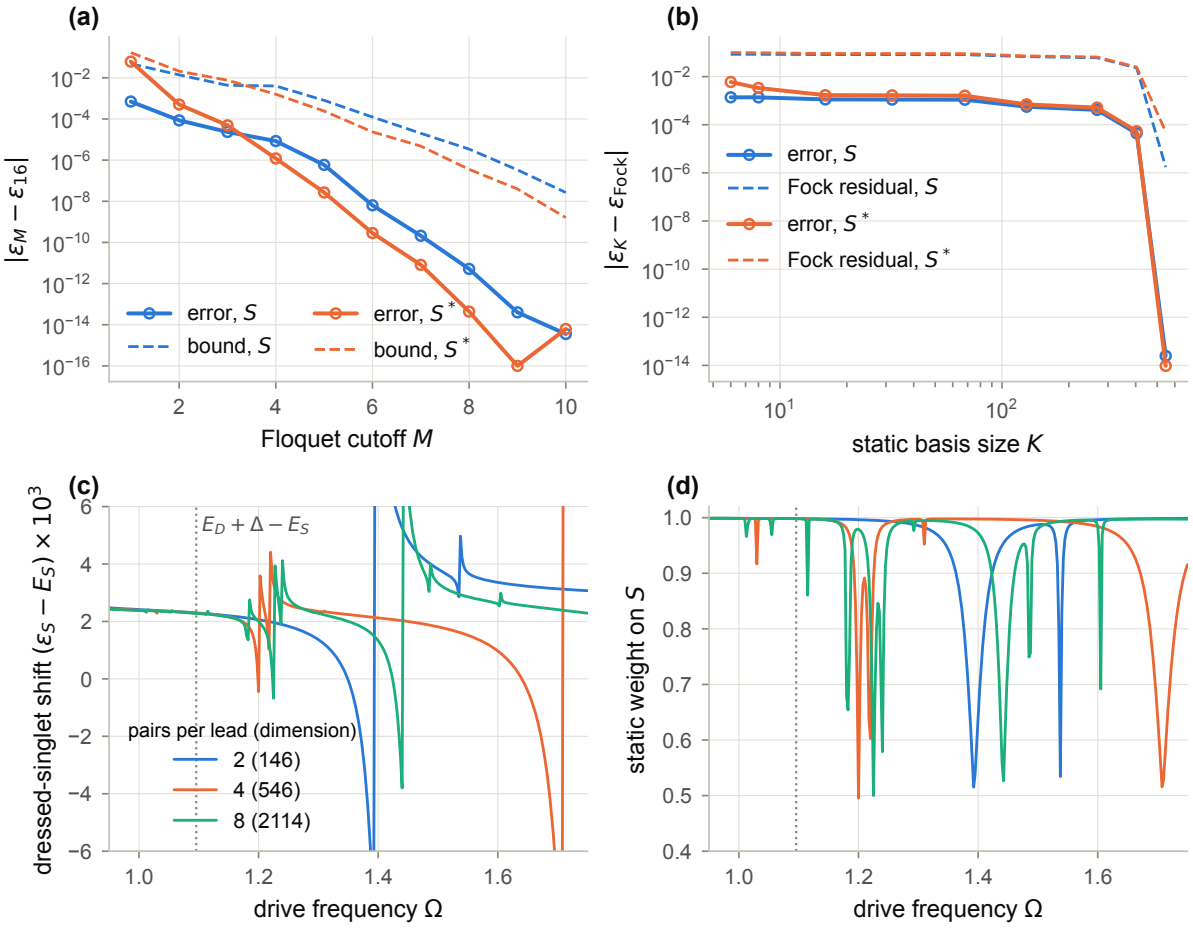


Figure 15.1: Convergence for the phase-driven reference junction. (a) Error of the tracked S and S^* quasienergies versus the Floquet cutoff (static basis, $K = 68$, $A = 1.5$, $\Omega = 0.45$), with the rigorous bound (10.2). (b) Error of the static-basis result versus K, relative to the full Fock space ($A = 0.3$), with the Fock-space residual. (c) AC Stark shift of the dressed singlet and (d) its static weight versus Ω across the one-photon continuum threshold (dotted), for three bath sizes ($A = 0.3$); the legend gives the number of level pairs per lead and the Fock-space dimension.

15.4 A practical workflow

1. Converge the static problem first: QP cutoff and bath, for the states of interest (Chapter 6).
2. Choose M from the modulation index: $M \gtrsim$ (largest level modulation)$/\Omega + 5$; check that `residuals` and `boundary_weights` are small.
3. For scans, use the static basis and check `fock_residuals`, or compare selected points with Fock-space shift-invert results.
4. Cross-check one point with `floquet_propagator`, which has no Floquet cutoff.
5. Above continuum thresholds, compare at least two bath sizes and interpret only features that are stable under refinement.

Tutorial: *Numerical convergence of a driven calculation* (`examples/05_convergence`).

16 Example: the phase-driven junction

Microwave irradiation of a superconducting loop that contains the junction modulates the phase difference, $\phi(t) = \phi_0 + A\cos\Omega t$. This is the configuration of Andreev spectroscopy experiments, in which absorption of microwave photons excites the junction from its ground state into the excited singlet, the "pair transition" [30–34]. The theory of the microwave response of Andreev levels is developed in Refs. [35, 36, 114, 144–146]; for interacting dots, see Refs. [42, 43, 147]. Here we compute the dressed subgap states of the interacting reference junction (3.7), where $\omega_{SS^*} = E_{S^*} - E_S = 0.716$.

16.1 The pair transition

For a weak drive the phase couples through the current operator $\partial_\phi H \equiv \partial H/\partial\phi$ (Section 9.3), and the Rabi splitting at the resonance $\Omega \approx \omega_{SS^*}$ is

$$\delta = A\,|\langle S|\partial_\phi H|S^*\rangle|, \tag{16.1}$$

with $|\langle S|\partial_\phi H|S^*\rangle| = 0.0272$ for the reference junction. The matrix element is small: at $\epsilon = 0.2$ the junction is close to the particle–hole-symmetric point, where it vanishes by the eta selection rule (Section 9.6 and Chapter 17). Figure 16.2(a) shows the rotating-frame quasienergies ε_S and $\varepsilon_{S^*} - \Omega$ near the resonance for $A = 0.4$. The Sambe solution in the full Fock space at QP cutoff 2 and the two-level RWA give the same avoided-crossing structure. Their energies differ by the AC Stark shift due to other states, which the two-level RWA omits; the offset grows as A^2. Panel (b) compares the splitting at the resonance with (16.1); at $A = 0.75$ the AC Stark shift has lowered the resonance frequency by 0.018. Both the RWA, whose coupling is $2|(H_1)_{SS^*}| = 8J_1(A/4)|\langle S|\partial_\phi H|S^*\rangle|$, and the full result fall below the linear law as the amplitude grows: at $A = 0.75$ they reach 0.996 (RWA) and 0.962 (full Sambe result) of the linear value. The Bessel saturation of the drive harmonic accounts for the reduction in the RWA; the counter-rotating terms, the higher harmonics and the other states, all omitted by the two-level RWA, reduce the effective coupling further. From $A \approx 0.8$ onwards, the pair hybridizes with replicas of other states and the splitting no longer follows a smooth curve.

16.2 The Floquet spectrum versus frequency and amplitude

Figure 16.1(a,b) shows the Floquet spectrum close to the ground state: every replica $\varepsilon_\alpha + \ell\Omega$ within ± 0.22 of E_S, coloured by its time-averaged weight on the undriven singlet. The calculation uses the complete Fock space of a bath with two level pairs per lead (dimension 146, $\omega_{SS^*} = 0.731$), so that all AC Stark shifts are included. The dressed singlet is the dark line. The light lines descending with slope $-\ell$ are replicas $E_b - \ell\Omega$, $\ell > 0$, of higher states b.

Where a replica crosses the dressed singlet and the drive couples the two, the lines repel and exchange weight; otherwise they cross.

As a function of the frequency, panel (a), the S^* replica produces the one-photon avoided crossing at $\Omega \approx 0.73$ and a much narrower two-photon crossing at $\Omega \approx 0.37$. Above the continuum threshold, $\Omega \gtrsim 1.1$, replicas of doublet-plus-quasiparticle states cross densely, and the strongest of them visibly repel the dressed singlet. Away from resonances the dressed singlet lies about 14×10^{-3} above E_S. Two contributions of comparable magnitude and opposite sign produce this shift. The time-averaged Hamiltonian H_0 renormalizes the hybridization, $\Gamma \to \Gamma J_0(A/4)^2$ (Equation (9.4)); for $A = 1$ the factor is 0.969, which weakens the binding of the singlet and, by itself, raises its energy by 30×10^{-3}. The second-order AC Stark shifts (8.10) lower the energy by 18×10^{-3} at $\Omega = 0.6$, which leaves 12×10^{-3}. At these low frequencies the result approaches the adiabatic average of the instantaneous energy, $\langle E_S(\phi(t))\rangle - E_S = 15 \times 10^{-3}$. As a function of the amplitude at $\Omega = 0.6$, panel (b), the dressed singlet rises roughly as A^2. Near $A \approx 1.4$ it hybridizes with a replica that the growing shift has brought into resonance.

16.3 The adiabatic limit

At low frequency, $\Omega \ll \omega_{SS^*}$, the junction follows the drive adiabatically, and the quasienergy of the dressed ground state tends to the time average of the instantaneous energy, Equation (8.11),

$$\varepsilon_S \simeq \frac{1}{2\pi} \int_0^{2\pi} E_S(\phi_0 + A\cos\vartheta)\, \mathrm{d}\vartheta. \tag{16.2}$$

The Berry phase vanishes for this one-dimensional back-and-forth motion. Figure 16.2(c) compares Floquet quasienergies at $\Omega = 0.1$ and 0.3 with (16.2). At $\Omega = 0.1$ the dressed singlet follows the adiabatic average until the phase swing reaches $\phi = \pi$, at $A = \pi - \phi_0$, where the S–S^* gap is smallest. Passages through this region are no longer adiabatic. The dressed state then acquires an admixture of S^*, its static weight on S drops, and its quasienergy falls below the adiabatic average: Landau–Zener transitions at each passage interfere from cycle to cycle, the mechanism of Chapter 13 [100]. At $\Omega = 0.3$ the photon energy approaches the minimal gap; around $A \approx 1.6$ a resonance with S^* mixes the two singlets strongly (faded markers: less than half of the weight on S), and beyond it the dressed singlet lies above the adiabatic curve.

Since $E_S(\phi)$ is a smooth function with a minimum near $\phi = 0$, the average increases with A: a strong slow phase drive raises the time-averaged ground-state energy and reduces the time-averaged supercurrent. Expanding (16.2) to second order, $\varepsilon_S - E_S \simeq \frac{A^2}{4} E_S''(\phi_0)$, and the curvature E_S'' contains the second-order coupling to *all* excited states, including quasiparticle states up to the bandwidth. This calculation therefore uses the complete Fock space of a smaller bath; a truncated static basis misses these contributions (Chapter 15).

16.4 Continuum, multiphoton processes and experiments

At higher frequencies the replicas of the bound states enter the continuum (Chapter 15): for $\Omega > E_D + \Delta - E_S$ a photon can break the singlet into a doublet plus a quasiparticle, the process that limits Andreev spectroscopy and causes quasiparticle poisoning [45, 144, 148, 149].

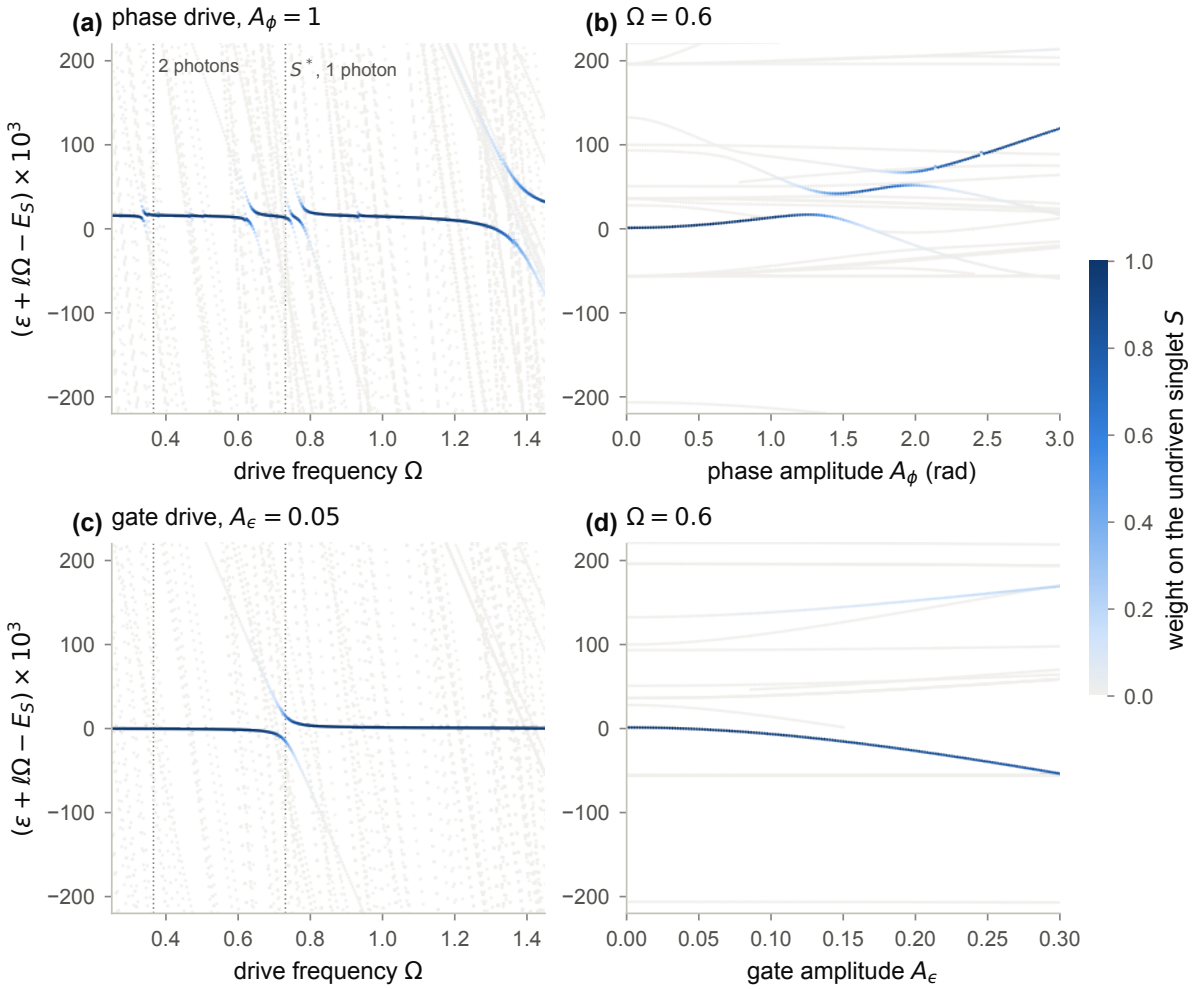


Figure 16.1: Floquet fan diagrams of the junction (two level pairs per lead, complete Fock space at QP cutoff 2, $M = 4$). Shown are all replicas $\varepsilon + \ell\Omega$ within ± 0.22 of the undriven singlet energy, coloured by their time-averaged weight on S. (a) Phase drive with $A_\phi = 1$ versus Ω; dotted lines mark the one- and two-photon S–S^* resonances. (b) Phase drive at $\Omega = 0.6$ versus amplitude. (c, d) The same for a gate drive with $A_\epsilon = 0.05$ and versus A_ϵ.

Two-photon transitions $S \to S^*$ at $\Omega \approx \omega_{SS^*}/2$ are mediated directly by the second harmonic of the phase drive (Section 9.3), which is proportional to the tunnelling operator rather than to the current, and in second order by the first harmonic through intermediate states. Floquet engineering of junctions by strong phase or voltage drives, including steady Floquet–Andreev states, is discussed in Refs. [46, 150–154].

In the code

```
static = solve(reference_model(**model), 2, Sector(0, 0), SolverOptions(method=
    "dense", eigenpairs=60))
periodic = PeriodicHamiltonian.from_parameters(reference_model, model,
    ParameterDrive.cosine("phi", 1.), 0.716)
```

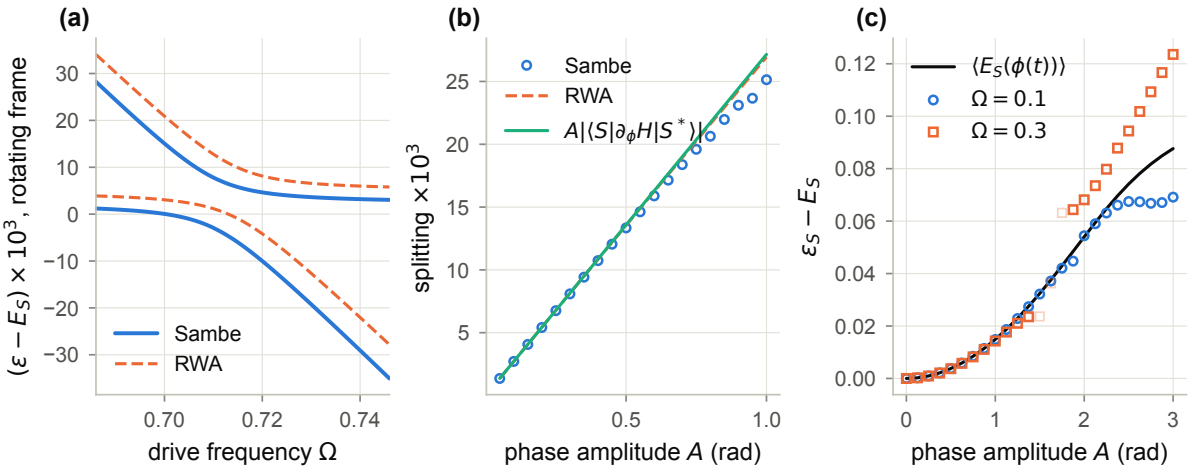


Figure 16.2: Phase-driven reference junction. (a) Rotating-frame quasienergies near the S–S^* resonance for $A = 0.4$, Sambe in the Fock space (solid) and RWA (dashed). (b) Splitting at the resonance versus amplitude, with (16.1) and the RWA $2|(H_1)_{SS^*}|$. (c) Quasienergy of the dressed singlet at low frequencies compared with the adiabatic average (16.2), in the complete Fock space of a bath with two level pairs per lead; faded markers denote states with less than half of their weight on S.

```
pair = solve_floquet(periodic, 2, Sector(0, 0), dict(floquet_cutoff=2, states
    =2), static=static)
rwa = rwa_model(periodic, [0, 1], [0, -1], 2, Sector(0, 0), static=static)
```

Passing `static` avoids recomputing the static eigenstates for every frequency of a scan.

User manual: *Floquet calculations* (`docs/floquet.md`).

Tutorial: *The phase-driven junction* (`examples/06_phase_drive`).

17 Example: the gate-driven junction

A microwave voltage on the gate electrode modulates the dot level, $\epsilon(t) = \epsilon_0 + A_\epsilon \cos \Omega t$. Gate driving is the standard way to probe charge transitions in quantum dots and is used for dispersive gate readout of Andreev and quantum-dot states [45, 113, 155, 156]. In the junction, gate and phase driving are complementary because their coupling operators obey different selection rules.

17.1 Complementary selection rules

To first order in the amplitude, the resonant splitting of the S–S^* transition is $A_\epsilon |\langle S|n_d|S^*\rangle|$ for the gate drive and $A_\phi |\langle S|\partial_\phi H|S^*\rangle|$ for the phase drive. Figure 17.1(a) shows both, computed by the Sambe solver at the undriven resonance frequency $\Omega = \omega_{SS^*}$, together with the static matrix elements, as functions of the detuning ϵ_0. Divided by A_ϵ, the gate-drive splitting agrees with $|\langle S|n_d|S^*\rangle|$ within 8×10^{-5}. Divided by A_ϕ, the phase-drive splitting agrees with $|\langle S|\partial_\phi H|S^*\rangle|$ within 9×10^{-4}, except at $\epsilon_0 = 0$ and at $\epsilon_0 = \pm 0.5$. At the latter detunings, levels of the discretized continuum lie close to the two-photon energy $E_S + 2\Omega$ and are coupled to S^* by the phase drive; this shifts the dressed states and changes the splitting per unit amplitude by 5×10^{-3}. The phase-drive matrix element vanishes exactly at the particle–hole-symmetric point and grows linearly away from it; the gate-drive matrix element is largest there. This is the eta-parity selection rule of Section 9.6: S and S^* have opposite eta parity, which only an eta-odd perturbation such as $n_d - 1$ can connect. The large-gap expressions (9.8), $\propto \sin\vartheta$ and $\propto \cos\vartheta$, reproduce the trend qualitatively. The small residual phase-drive splitting at $\epsilon_0 = 0$ arises from AC Stark detuning of the resonance while the coupling remains zero.

Physical picture

At particle–hole symmetry the singlets S and S^* are, to a good approximation, the bonding and antibonding combinations of the empty and doubly occupied dot. A phase drive modulates the strength of the pairing that binds them, shifting their energies while preserving their distinct eta parities. A gate drive tilts the balance between $|0\rangle$ and $|2\rangle$ and converts S into S^* directly.

17.2 The Floquet spectrum

Figure 16.1(c,d) is the gate-drive counterpart of the phase-drive fan diagram. Because the gate drive is linear in ϵ, it leaves the time-averaged Hamiltonian unchanged ($H_0 = H(\epsilon_0)$). Away from resonances the dressed singlet therefore stays close to E_S. The one-photon S–S^* avoided crossing is wide, reflecting the large charge matrix element. The two-photon crossing

is invisible at this amplitude, and the couplings to the continuum replicas are weak. At fixed $\Omega = 0.6 < \omega_{SS^*}$, panel (d), the dressed singlet is pushed down by the S^* replica above it. To second order, $\delta\varepsilon_S \simeq -\frac{A_\epsilon^2}{4}|\langle S|n_d|S^*\rangle|^2[(\omega_{SS^*} - \Omega)^{-1} + (\omega_{SS^*} + \Omega)^{-1}]$, the rotating and counter-rotating terms of Equation (8.10).

17.3 Two-photon transitions

At $\Omega \approx \omega_{SS^*}/2$ the pair transition is driven by two photons. Figure 17.1(b) compares the one- and two-photon splittings at their respective resonances. The one-photon splitting grows linearly with A_ϵ, the two-photon splitting quadratically, as a second-order process must. Two mechanisms contribute to the two-photon coupling: virtual transitions through other states, and the difference of the average charges of S and S^*, which modulates their splitting and acts like the Bessel-function mechanism of Chapter 13. Both resonances move with the drive amplitude, by AC Stark and Bloch–Siegert shifts; each resonance is located at the minimum of the quasienergy splitting as a function of Ω. At the largest amplitudes the one-photon splitting falls below the linear dependence as counter-rotating terms and coupling to other states become important.

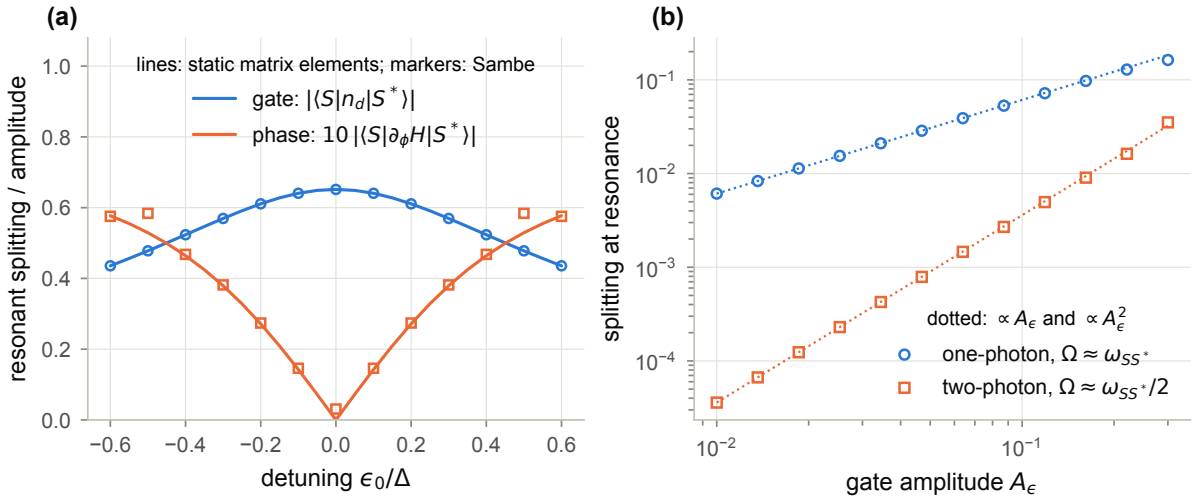


Figure 17.1: Gate-driven reference junction. (a) Resonant S–S^* splitting per unit amplitude for a gate drive ($A_\epsilon = 0.01$, circles) and a phase drive ($A_\phi = 0.1$, squares, scaled by 10), versus the detuning ϵ_0, compared with the static matrix elements (lines). (b) One- and two-photon splittings at their resonances versus the gate amplitude; dotted lines are $\propto A_\epsilon$ and $\propto A_\epsilon^2$.

In the code

```
gate = PeriodicHamiltonian.from_parameters(reference_model, model,
                                           ParameterDrive.cosine("detuning",
    .01), omega=.716)
states = solve_floquet(gate, 2, Sector(0, 0), dict(floquet_cutoff=2, states=2))
```

Since a linear gate drive has only $H_{\pm1}$, a few samples reproduce $H(t)$ exactly; the two-photon calculation needs $M \geq 2$ to contain the intermediate replica.

User manual: *Floquet calculations* (`docs/floquet.md`).

Tutorial: *The gate-driven junction* (`examples/07_gate_drive`).

18 Example: two-tone spectroscopy of the pair transition

In two-tone spectroscopy a strong pump drives one transition while a weak probe scans the spectrum. For superconducting qubits and Andreev levels this is the standard way to reveal dressed states [32, 34, 88]. We pump the S–S^* pair transition of the reference junction with the gate, $A_\epsilon = 0.03$, at $\Omega \approx \omega_{SS^*} = 0.716$, and probe it with a second gate tone (probe operator n_d). The Rabi splitting is $\delta = A_\epsilon |\langle S|n_d|S^*\rangle| = 0.0183$ (Chapter 17).

18.1 Dressed-state lines versus pump detuning

Figure 18.1(a) shows the probe lines from the dressed ground state as a function of the pump detuning $\Omega - \omega_{SS^*}$, for probe frequencies $|\omega|$ near the pump frequency. Three branches appear: the elastic line at Ω, and two lines that avoid each other and follow the rotating-wave prediction $\Omega \pm w$, with $w = \sqrt{(\Omega - \omega_{SS^*})^2 + \delta^2}$. Far from resonance the dressed state is nearly the bare singlet. The strong line then returns to the bare transition ω_{SS^*}, while the other sideband, associated with a three-photon process, loses intensity. The lighter lines represent transitions to other states, mostly the discretized continuum.

18.2 The Mollow triplet

At resonance, Figure 18.1(b), the probe spectrum of the dressed ground state shows the Mollow triplet of Section 11.5. The rate spectrum has lines at $\Omega - \delta$, Ω and $\Omega + \delta$. The RWA predicts a strength of $|\langle S|n_d|S^*\rangle|^2/4 = 0.093$ for each sideband and for each of the two elastic lines at $\pm\Omega$, which together form the central line. The computed strengths are 0.095 at $\Omega - \delta$, 0.094 for each elastic line and 0.092 at $\Omega + \delta$; the small asymmetry arises from counter-rotating terms and coupling to other states. The net spectrum distinguishes absorption at $\Omega + \delta$ from stimulated emission at $\Omega - \delta$; the elastic lines make no net contribution. Experiments on pumped superconducting qubits show the same pattern [134].

18.3 The Autler–Townes doublet

Panel (c) probes a spectator transition. Starting from the doublet D, a tunnelling probe removes a spin-up electron and connects D with the dressed singlets. Without the pump the removal spectrum has a single line at $E_D - E_S$. With the pump it splits into two lines separated by $\delta = 0.0183$, each with half of the static weight $|\langle S|d_\uparrow|D\rangle|^2$: the Autler–Townes doublet.

Observing it requires the initial state to lie outside the pumped pair. A junction in its doublet ground state, probed by tunnelling or by a transmon coupled to the parity, therefore shows the dressing of the singlet pair directly.

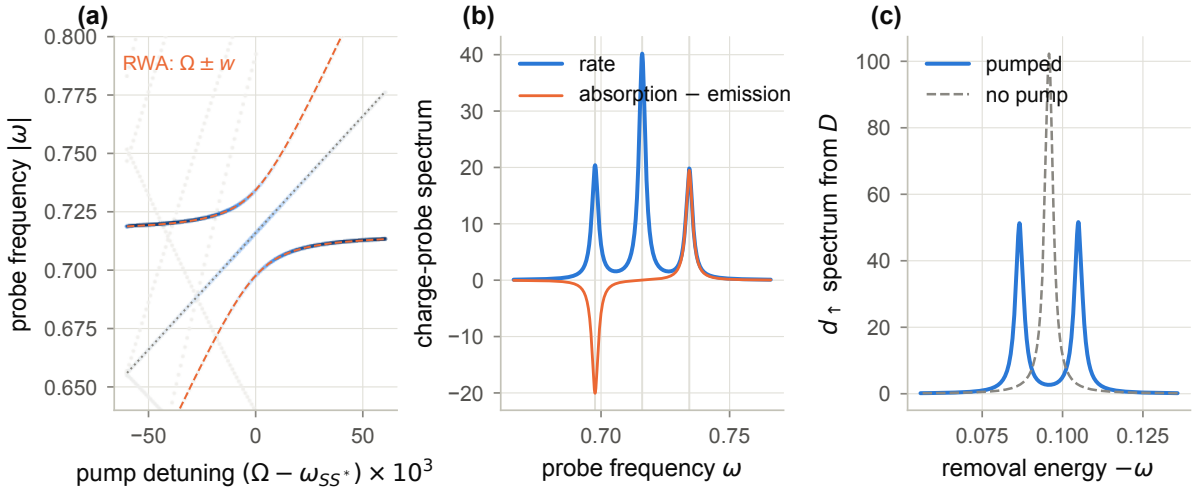


Figure 18.1: Two-tone spectroscopy of the reference junction with a gate pump $A_\epsilon = 0.03$ near $\omega_{SS^*} = 0.716$ (static basis $K = 43$, $M = 6$). (a) Gate-probe lines from the dressed ground state versus pump detuning; darker points are stronger lines, dashed lines the RWA $\Omega \pm w$, the dotted line the elastic line Ω. (b) Rate and net (absorption minus emission) spectra at resonance: the Mollow triplet. (c) Removal spectrum of $d_\uparrow$ from the doublet with and without the pump: the Autler–Townes doublet.

Caution

At resonance the label of the dressed ground state can switch between the two dressed states, which have equal weights on S. When spectra from one dressed state are compared across a resonance, include both dressed states with explicit initial weights, or use a spectator state. A current probe of the pair transition is weak at $\epsilon = 0.2$, $|\langle S|\partial_\phi H|S^*\rangle| = 0.027$. Its strongest lines are transitions into the discretized continuum near the gap edge, and a low-frequency line at δ between the two hybrids, with strength $\left[(\langle S|\partial_\phi H|S\rangle - \langle S^*|\partial_\phi H|S^*\rangle)/2\right]^2 = 0.0059$, set by the different supercurrents of S and S^*. The gate probe is the better choice for the Mollow pattern.

Tutorial: *Two-tone spectroscopy of the pair transition* (`examples/08_two_tone`).

19 Example: photon-assisted tunnelling into a driven junction

A weak tunnelling contact, such as a scanning-tunnelling tip or a normal lead, adds or removes single electrons and thereby measures transitions between the even and odd subgap states. Under a microwave gate drive each tunnelling line acquires sidebands at multiples of the drive frequency: photon-assisted tunnelling. It was described by Tien and Gordon for superconducting tunnel junctions [135], observed in quantum dots [111, 112], and recently used to probe Yu–Shiba–Rusinov states with a scanning tunnelling microscope [47–49].

19.1 Tien–Gordon and its generalization

For the decoupled dot, Chapter 12, the sideband weights are Bessel functions, $J_q^2(\Delta n\, A/\Omega)$, with Δn the charge difference between the final and the initial state. This result is exact, and the tests of qdjj_solver check that the code reproduces it to 10^{-10}. In the junction the subgap states have non-integer charges, $n_S = 0.740$ and $n_D = 0.970$ for the bath used here, so the simple Tien–Gordon formula with $\Delta n = 0.23$ provides a natural first approximation. It neglects two effects. The transition energy $E_D(\epsilon) - E_S(\epsilon)$ depends nonlinearly on the detuning, and so does the tunnelling matrix element $\langle D|d_\uparrow^\dagger|S\rangle$. For a slow drive both are captured by an adiabatic generalization, in which the sideband amplitudes are the Fourier coefficients of

$$F(t) = \mathcal{M}(\epsilon(t)) \exp\Big[\mathrm{i}\int_0^t (\Delta E(\epsilon(t')) - \overline{\Delta E})\mathrm{d}t'\Big], \tag{19.1}$$

with $\mathcal{M}(\epsilon) = \langle D(\epsilon)|d_\uparrow^\dagger|S(\epsilon)\rangle$ and $\Delta E = E_D - E_S$ from static calculations along the drive.

19.2 Results

In Figure 19.1 the gate of a junction with two bath level pairs per lead is driven at $\Omega = 0.05$, far below the excitation gaps within each parity sector (0.73 for the singlets, 1.31 above the doublet), and the addition spectrum of $d_\uparrow^\dagger$ is evaluated from the dressed singlet. Panel (a) shows the sidebands spreading out as the amplitude grows. Panel (b) compares the weights of the lines into the dressed doublet with the two formulas. The Floquet results follow the adiabatic generalization (19.1) closely, while the simple Tien–Gordon expression reproduces the overall envelope with symmetric weights for $q = +1$ and $q = -1$. The adiabatic expression captures the asymmetry through the detuning-dependent energy and matrix element. For $A = 0.4$, ΔE varies from 0.08 to 0.26 and $|\mathcal{M}|$ from 0.48 to 0.78 over the drive period. Evaluating (19.1) with a constant $\mathcal{M}$, or with a linearized ΔE, shows that the two dependences produce asymmetries

of opposite sign; the observed asymmetry is their net effect. The Floquet calculation retains nonadiabatic dynamics and extends the treatment to frequencies Ω approaching the internal gaps, beyond the regime of (19.1).

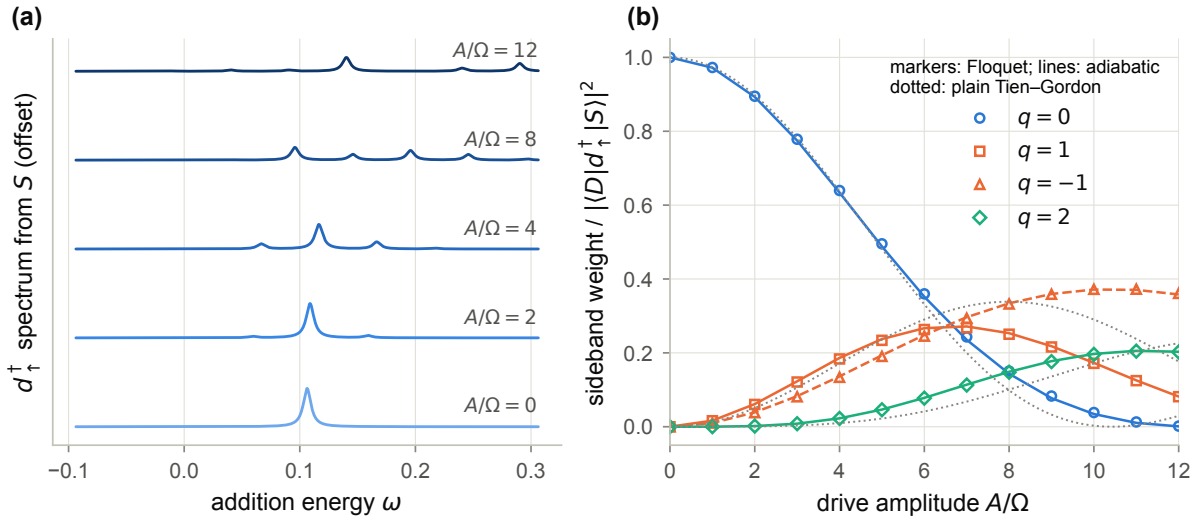


Figure 19.1: Photon-assisted tunnelling: gate drive at $\Omega = 0.05$ on a junction with two bath level pairs per lead ($U = 1$, $\Gamma = 0.5$, $\epsilon = 0.2$, $\phi = 0.8$). (a) Addition spectrum of $d^\dagger_\uparrow$ from the dressed singlet for several amplitudes, offset vertically (Lorentzian half width 0.004). (b) Weights of the sidebands into the dressed doublet, normalized to the static strength. Markers: Floquet; solid ($q \geq 0$) and dashed ($q < 0$) lines: adiabatic generalized Tien–Gordon (19.1); dotted lines: plain $J_q^2(\Delta n\, A/\Omega)$.

Caution

Microwaves applied to a tunnelling experiment also modulate the probe contact itself, which produces replicas of every line independently of any dressing of the junction. Separating the two requires the drive to act on the junction alone, or a model of the probe circuit [157].

Tutorial: *Photon-assisted tunnelling into a driven junction* (`examples/09_photon_assisted_tunnelling`).

20 Example: electron spin resonance of the doublet

In a static magnetic field the doublet splits into $D_\uparrow$ and $D_\downarrow$. A transverse ac field then drives spin flips between them: electron spin resonance (ESR) of the impurity spin, the mechanism behind spin qubits in quantum dots [116, 158, 159] and ESR-STM of single atoms [117, 118, 160]. In a superconducting junction the spin is partially screened by the coupling to the leads, and ESR probes the resulting reduction of the local spin response. This renormalization is also relevant to Andreev spin qubits, whose electrically driven transitions depend on spin–orbit coupling [37, 39, 40, 44, 161].

20.1 The model

The impurity carries a static Zeeman energy BS_d^z and a transverse drive,

$$H_d(t) = \frac{U}{2}(n_d - 1)^2 + \epsilon(n_d - 1) + B\,S_d^z + b\cos(\Omega t)\,S_d^x, \qquad S_d^x = \tfrac{1}{2}(d_\uparrow^\dagger d_\downarrow + d_\downarrow^\dagger d_\uparrow). \tag{20.1}$$

The field acts on the dot only, as for a g-factor that is large on the dot and small in the leads. The transverse term couples different S_z values, so the calculation is done in the odd sector with all spin projections, `Sector(1, None)`. A model constructor with a `transverse` parameter implements this drive:

```
from qdjj_solver import Impurity, annihilate, create, hermitian_pair, make_model

def esr_model(transverse=0., gamma=.3, u=1., detuning=0., field=.02, phi=.8):
    anderson = Impurity.anderson(u, detuning, field)
    operator = anderson.operator + hermitian_pair(.5*transverse*create(0)*
    annihilate(1))  # b S_x
    impurity = Impurity(1, operator, metadata=dict(kind="anderson-transverse"))
    t = np.sqrt(gamma/(np.pi*bath.rho*2))*np.eye(2)
    return make_model(impurity, [bath, bath], [t, t], phases=[-phi/2, phi/2],
                      phase_velocities=[-.5, .5])

esr = PeriodicHamiltonian.from_parameters(esr_model, dict(transverse=0., gamma=.3),
                                          ParameterDrive.cosine("transverse", .004)
    , omega=.0173)
```

20.2 Rabi splitting and the effective g-factor

For a free spin, the Zeeman splitting is B and the resonant Rabi splitting of the drive $b\cos(\Omega t)S^x$ is $b/2$. In the junction the doublet is a correlated state of the dot spin and the leads. Within

the doublet the impurity spin operator is proportional to the total spin, $\boldsymbol{S}_d = (g_{\mathrm{eff}}/g)\,\boldsymbol{S}$, by the Wigner–Eckart theorem, with

$$\frac{g_{\mathrm{eff}}}{g} = 2|\langle D_\downarrow|S_d^z|D_\downarrow\rangle| \le 1. \tag{20.2}$$

The relation is exact at zero field. In a field the polarizations of the two Zeeman levels differ at linear order in B; we quote that of the lower level $D_\downarrow$, and the transverse element $2|\langle D_\uparrow|S_d^x|D_\downarrow\rangle|$ equals their mean. Both the Zeeman splitting and the Rabi splitting are therefore renormalized by the same factor:

$$E_{D_\uparrow} - E_{D_\downarrow} \simeq \frac{g_{\mathrm{eff}}}{g}\,B, \qquad \delta_{\mathrm{Rabi}} = b\,|\langle D_\uparrow|S_d^x|D_\downarrow\rangle| = \frac{g_{\mathrm{eff}}}{g}\,\frac{b}{2}. \tag{20.3}$$

The reduction of the effective g-factor of a quantum-dot junction with increasing coupling is the impurity Knight shift [65].

Figure 20.1(a) shows the Autler–Townes splitting of the doublet at the ESR resonance for $\Gamma = 0.3$, where $g_{\mathrm{eff}}/g = 0.866$. Panel (b) compares three determinations of g_{eff}/g as functions of Γ: the static spin polarization (20.2), the Zeeman splitting divided by B, and the Floquet Rabi splitting divided by $b/2$. They agree within 2×10^{-3}, the size of the finite-field and Bloch–Siegert corrections, and decrease from 1 at $\Gamma = 0$ to 0.65 at $\Gamma = 1.2$.

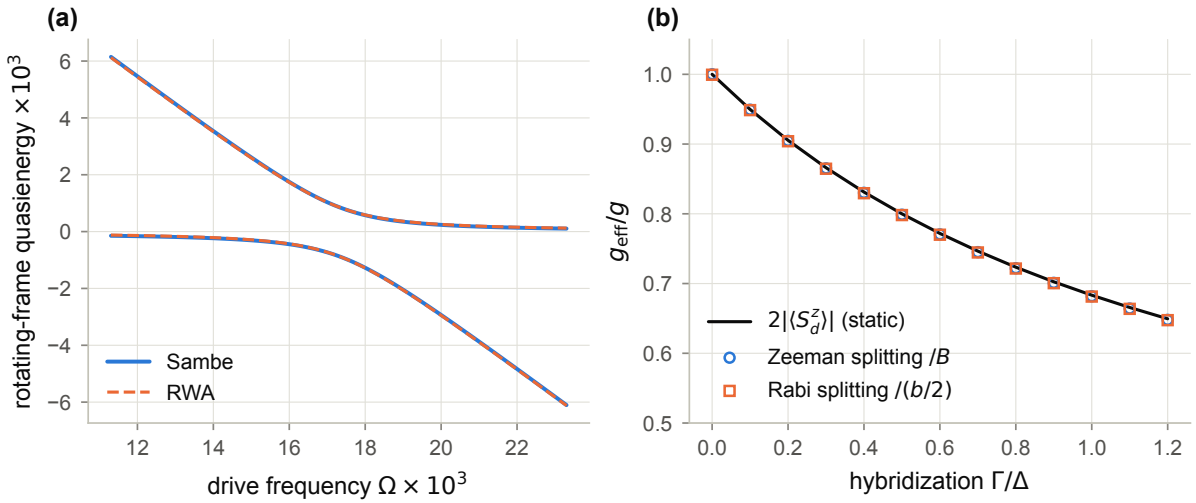


Figure 20.1: ESR of the doublet in the reference junction at $\epsilon = 0$, $U = 1$, $\phi = 0.8$, $B = 0.02$. (a) Rotating-frame quasienergies near the Zeeman resonance for $\Gamma = 0.3$ and $b = 0.004$, Sambe (solid) and RWA (dashed). (b) Effective g-factor from the static spin polarization, the Zeeman splitting and the Floquet Rabi splitting.

20.3 Probing the driven spin

The dressed doublet can be probed with a second, weak field (Chapter 11). A transverse probe S_d^x acts on the pumped transition itself, and a longitudinal probe S_d^z, a weak modulation of the static field, connects the two dressed states. Figure 20.2 shows both for $\Gamma = 0.3$, $b = 0.004$,

starting from the dressed continuation of the lower Zeeman level. The Zeeman splitting is $Z = 0.0173$ and the resonant Rabi splitting is $\delta = 0.00173 = 0.1\,Z$.

The transverse probe, panels (a) and (b), shows the Mollow pattern of Section 11.5: two lines that avoid each other at resonance and follow the rotating-wave prediction $\Omega \pm w$, with $w = \sqrt{(\Omega - Z)^2 + \delta^2}$, and the elastic line at Ω. By the Wigner–Eckart argument above, each of the four lines carries $|\langle D_\uparrow | S_d^x | D_\downarrow \rangle|^2/4 \simeq (g_{\mathrm{eff}}/g)^2/16 = 0.0468$ at resonance; the computed values are 0.049 and 0.045 for the sidebands and 0.047 for each elastic line. The asymmetry of the two sidebands is a counter-rotating effect of order δ/Z: it halves when b is halved.

The longitudinal probe, panel (c), shows a single line at the Rabi frequency, the transition between the two dressed states. Its strength, $\frac{1}{4}(\langle D_\uparrow | S_d^z | D_\uparrow \rangle - \langle D_\downarrow | S_d^z | D_\downarrow \rangle)^2 \simeq (g_{\mathrm{eff}}/g)^2/4 = 0.1871$ in the RWA (computed: 0.1865), measures the effective g-factor through a matrix element instead of a splitting.

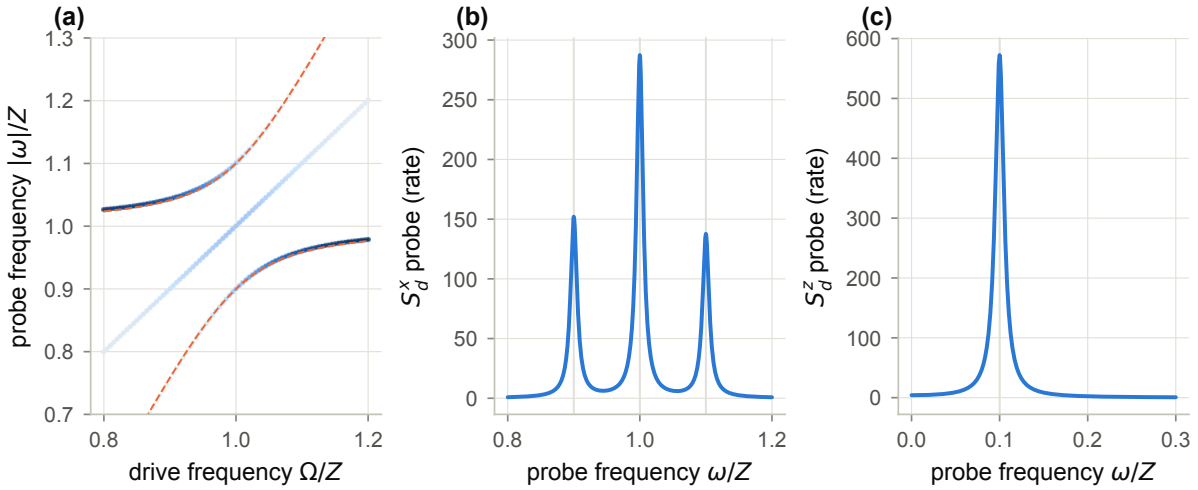


Figure 20.2: Probing the Rabi-driven doublet ($\Gamma = 0.3$, $b = 0.004$, $M = 8$, static basis $K = 24$). (a) Lines of a transverse probe S_d^x versus drive frequency, darker for stronger lines; dashed: RWA $\Omega \pm w$. (b) Rate spectrum of S_d^x at resonance: sidebands at $Z \pm \delta$ and the central elastic line. (c) Rate spectrum of S_d^z at resonance: the line at the Rabi frequency $\delta = 0.1\,Z$. Line half width $0.006\,Z$.

Caution

At resonance the replicas $|D_\downarrow, m\rangle$ and $|D_\uparrow, m-1\rangle$ form a resonant chain through the entire Sambe space. A small Floquet cutoff truncates this chain and creates unpaired edge states, which perturb the interior replicas at the order of the Rabi coupling. Even for weak drives, use a Floquet cutoff of several harmonics ($M \gtrsim 5$); the residual bound and the check that the tracked states are distinct Floquet states detect an insufficient cutoff.

Tutorial: *Electron spin resonance of the doublet* (`examples/10_spin_resonance`).

Part IV

From equations to code

21 From the equations to the code

This manual describes the physics; the user and developer manual describes how to run and extend the code. Table 21.1 connects the two: for each concept it identifies the equation or section of this manual, the corresponding code interfaces, and the user-manual page that explains their use. The complete lists of options, result fields, command-line arguments, observables and probes are generated from the code into the reference pages of the user manual, and the error messages with their remedies are collected on its troubleshooting page:

- User manual: *qdjj_solver documentation* (`docs/index.md`);
- User manual: *Option reference* (`docs/reference/options.md`), and the neighbouring reference pages;
- User manual: *Troubleshooting* (`docs/troubleshooting.md`).

Table 21.1: Concepts of this manual, their equations or sections, the corresponding names in the code, and the page of the user manual that explains their use.

Concept	Here	In the code	User manual
Superconducting Anderson impurity and reference junction	Equation (3.7)	`reference_model`, `Impurity.anderson`, `make_model`	Physical models and conventions; tutorial 01
Discretized superconducting reservoirs	Section 6.4	`cosh_grid`, `fit_surrogate`, `chain_expansion`, `DiscreteBath`	Choosing and refining superconducting reservoirs; tutorial 05
Symmetry sectors	Section 3.5	`Sector`	Physical models and conventions; tutorial 01
Canonical coordinates	Section 6.2	`Hamiltonian.physical_operator`, `Hamiltonian.coordinate_fingerprint`	Physical models and conventions
Quasiparticle expansion	Equation (6.1)	`qp_solver.solve`, `qp_solver.SolverOptions`	QP calculations and observable-specific convergence; tutorial 00
Density-matrix renormalization group	Section 6.5	`dmrg_solver.solve`, `dmrg_solver.SolverOptions`	DMRG states and bond-dimension refinement; tutorial 11
Checked calculations and saved results	Chapter 7	`solve`, `save_result`, `load_result`	Parameter scans, saved results and reproducible analysis; tutorial 01
Supercurrent	Equation (3.8)	`phase_derivative`	Physical models and conventions; tutorial 01

Concept	Here	In the code	User manual
Transition frequencies and static matrix elements	Equation (8.12)	`Eigenstates.matrix_elements`, `Hamiltonian.probe`	Using the solver and saving results; tutorial 06
Parameter drives and harmonics	Equation (9.1)	`ParameterDrive`, `Harmonic`, `PeriodicHamiltonian.from_parameters`	Floquet calculations; tutorial 06
Floquet states and quasienergies	Equation (8.2)	`FloquetStates.quasienergies`, `FloquetStates.modes`	Floquet calculations; tutorial 02
Mean energy	Equation (8.6)	`FloquetStates.mean_energies`	Floquet calculations; tutorial 02
Sambe matrix and Floquet cutoff	Equation (8.5)	`solve_floquet`, `FloquetOptions.floquet_cutoff`	Floquet calculations; tutorial 05
Static basis of size K	Section 10.2	`FloquetOptions.basis`, `FloquetOptions.basis_states`	Floquet calculations; tutorial 05
Replicas, branches and folded quasienergies	Section 10.2	`FloquetOptions.selection`, `FloquetOptions.branch`, `FloquetStates.folded`	Floquet calculations
Residual bound	Equation (10.2)	`FloquetStates.residuals`, `FloquetStates.fock_residuals`	Floquet calculations; tutorial 05
Gauge freedom and c-number terms	Section 8.5	`FloquetOptions.drop_scalar_harmonics`	Floquet calculations; tutorial 02
Fixed canonical coordinates	Section 9.5	`PeriodicHamiltonian.coordinate_fingerprint`	Floquet calculations
One-period propagator	Equation (10.3)	`floquet_propagator`, `FloquetOptions.steps`	Floquet calculations; tutorial 05
High-frequency expansion	Equation (10.4)	`PeriodicHamiltonian.van_vleck`	Floquet calculations; tutorial 04
Rotating-wave model	Equation (10.5)	`rwa_model`	Floquet calculations; tutorial 03
Floquet matrix elements	Equation (11.1)	`FloquetStates.matrix_elements`, `FloquetTransitions`	Floquet calculations; tutorial 08
Floquet golden rule and lines	Equation (11.2)	`FloquetTransitions.lines`, `SpectralLines.spectrum`, `line_shape`	Floquet calculations; tutorial 08
Sum rule	Equation (11.3)	`FloquetTransitions.completeness`	Floquet calculations; tutorial 02

21.1 Reproducing the figures and this manual

```
cd docs/manual
make data      # recompute data/*.json with the solver (tens of minutes)
make quoted    # numbers quoted in the text, from data/*.json
make figures   # render figures/*.pdf from data/*.json (requires matplotlib)
make pdf       # quoted values and figures, then latexmk (pdflatex + biber)
```

Each record in `data/` stores the script name, the code version and git commit, and the numerical environment. Figures and quoted numerical values are generated from the saved data without rerunning the solver, so the PDF can be rebuilt quickly. The figure scripts write the quoted values to `generated/quoted.tex`. Recomputing the data therefore updates the values in the text, and changes can be reviewed in the generated-file diff.

A Derivations

A.1 Harmonics of the phase drive

For the reference junction the tunnelling term of lead l is $\mathrm{e}^{\mathrm{i}s_l\phi(t)/4}X_l + \mathrm{h.c.}$, with $s_{L,R} = \mp 1$ and $X_l = t_l \sum_\sigma C_{l\sigma}^\dagger d_\sigma$. With $\phi(t) = \phi_0 + A\cos(\Omega t + \theta)$ and the Jacobi–Anger expansion $\mathrm{e}^{\mathrm{i}z\cos\vartheta} = \sum_n \mathrm{i}^n J_n(z)\mathrm{e}^{\mathrm{i}n\vartheta}$, together with $J_n(-z) = (-1)^n J_n(z)$, we obtain

$$\mathrm{e}^{\mathrm{i}s_l\phi(t)/4} = \mathrm{e}^{\mathrm{i}s_l\phi_0/4} \sum_k (\mathrm{i}s_l)^k J_k\Big(\tfrac{A}{4}\Big)\, \mathrm{e}^{\mathrm{i}k\theta}\mathrm{e}^{\mathrm{i}k\Omega t}. \tag{A.1}$$

The Hermitian conjugate contributes $\mathrm{e}^{-\mathrm{i}s_l\phi_0/4}(-\mathrm{i}s_l)^k J_k(A/4)\mathrm{e}^{\mathrm{i}k\theta}X_l^\dagger$ to the same harmonic k. For $k = 0$ both terms are multiplied by $J_0(A/4)$, which renormalizes $t_l \to t_l J_0(A/4)$ and hence $\Gamma \to \Gamma J_0(A/4)^2$. For even $k \neq 0$, $(\mathrm{i}s_l)^k = (-\mathrm{i}s_l)^k = (-1)^{k/2}$ and the harmonic is $(-1)^{k/2}J_k(A/4)\mathrm{e}^{\mathrm{i}k\theta}H_T(\phi_0)$. For odd k, $(\pm\mathrm{i}s_l)^k = \pm\mathrm{i}s_l(-1)^{(k-1)/2}$, which reproduces the derivative $\partial_\phi(\mathrm{e}^{\mathrm{i}s_l\phi/4}X_l + \mathrm{h.c.}) = \frac{\mathrm{i}s_l}{4}\mathrm{e}^{\mathrm{i}s_l\phi/4}X_l + \mathrm{h.c.}$ up to the factor $4(-1)^{(k-1)/2}J_k(A/4)\mathrm{e}^{\mathrm{i}k\theta}$. This gives Equations (9.4) and (9.5).

A.2 The residual bound

Let $\mathcal{Q}$ be the self-adjoint Sambe operator on the infinite extended space, v a normalized vector supported on the window $|m| \le M$, and λ real. The expansion of v in the spectral measure μ_v of $\mathcal{Q}$ gives $\|(\mathcal{Q}-\lambda)v\|^2 = \int|\varepsilon-\lambda|^2\mathrm{d}\mu_v(\varepsilon) \ge \mathrm{dist}(\lambda, \mathrm{spec}\,\mathcal{Q})^2$. The vector $(\mathcal{Q}-\lambda)v$ has the components $(Q_M-\lambda)v$ inside the window and $\sum_{m'} H_{m-m'}v_{m'}$ outside it, which are orthogonal. Hence

$$\mathrm{dist}(\lambda, \mathrm{spec}\,\mathcal{Q}) \le \sqrt{\|(Q_M-\lambda)v\|^2 + \sum_{|m|>M}\Big\|\sum_{|m'|\le M} H_{m-m'}v_{m'}\Big\|^2}, \tag{A.2}$$

which is Equation (10.2). Let v now be an eigenvector of Q_M, so that λ equals the expectation value of $\mathcal{Q}$ in v. If the exact eigenvalue ε nearest to λ is separated from the rest of the spectrum by a gap g, the Kato–Temple inequality improves the bound to $|\varepsilon-\lambda| \le \|(\mathcal{Q}-\lambda)v\|^2/g$. This explains the quadratic relation between bound and error observed in Figure 15.1(a).

A.3 The high-frequency expansion

In the Sambe space the diagonal blocks $m \neq 0$ are shifted by $m\Omega$ relative to the $m = 0$ block; for Ω larger than the spectral width of H_0 they are well separated. A unitary transformation $\mathrm{e}^{\mathrm{i}\mathcal{S}}$ that removes the couplings between blocks order by order, the Schrieffer–Wolff or van Vleck

construction [85, 162–164], leaves a block-diagonal operator whose $m = 0$ block is H_{eff}. To first order the generator is $\mathcal{S}_{m0} = -\mathrm{i}H_m/(m\Omega)$, and the second-order correction to the $m = 0$ block is

$$\sum_{m\neq 0} \frac{H_{-m}H_m}{0 - m\Omega} = \frac{1}{\Omega}\sum_{m\geq 1} \frac{[H_m, H_{-m}]}{m}, \tag{A.3}$$

the first-order term of Equation (10.4). The next order follows in the same way, including the dependence of the energy denominators on H_0; the result is the Ω^{-2} term of Equation (10.4). Because the transformation is periodic in time, H_{eff} is invariant under shifts of the time origin. The Floquet–Magnus Hamiltonian $H_F[t_0]$, defined by $U(t_0 + T, t_0) = \mathrm{e}^{-\mathrm{i}H_F[t_0]T}$, depends on t_0: it is related to H_{eff} by the t_0-dependent kick operator of Chapter 8, and only its exact spectrum is independent of t_0 [50, 51].

A.4 The commutator-free Magnus integrator

The fourth-order Magnus expansion over a step h uses the Gauss–Legendre nodes $c_{1,2} = \frac{1}{2} \mp \frac{\sqrt{3}}{6}$ and $H_i = H(t + c_i h)$. It approximates $U(t + h, t) \approx \mathrm{e}^{-\mathrm{i}\mathcal{M}_4}$ with

$$\mathcal{M}_4 = \frac{h}{2}(H_1 + H_2) - \mathrm{i}\frac{\sqrt{3}h^2}{12}[H_2, H_1]. \tag{A.4}$$

(We write $\mathcal{M}_4$ for the Magnus operator, usually called Ω_4, to avoid confusion with the drive frequency.) The commutator-free variant replaces $\mathrm{e}^{-\mathrm{i}\mathcal{M}_4}$ by two exponentials of linear combinations of H_1 and H_2 with the coefficients $\alpha_{1,2}$ of Equation (10.3). This reproduces $\mathcal{M}_4$ to fourth order without commutators and keeps every factor unitary [126, 127]. The global error over one period scales as h^4, so halving the time step reduces it by a factor of 16, and the Richardson estimate $|\varepsilon_h - \varepsilon_{h/2}|/15$ of Section 10.3 follows.

References

[1] P. W. Anderson, "Localized magnetic states in metals", Physical Review **124**, 41 (1961) 10.1103/PhysRev.124.41.

[2] L. Yu, "Bound state in superconductors with paramagnetic impurities", Acta Physica Sinica **21**, 75 (1965) 10.7498/aps.21.75.

[3] H. Shiba, "Classical spins in superconductors", Progress of Theoretical Physics **40**, 435 (1968) 10.1143/PTP.40.435.

[4] A. I. Rusinov, "Superconductivity near a paramagnetic impurity", JETP Letters **9**, 85 (1969), [Pis'ma Zh. Eksp. Teor. Fiz. **9**, 146 (1968)].

[5] A. V. Balatsky, I. Vekhter, and J.-X. Zhu, "Impurity-induced states in conventional and unconventional superconductors", Reviews of Modern Physics **78**, 373 (2006) 10.1103/RevModPhys.78.373, arXiv:cond-mat/0411318.

[6] L. I. Glazman and K. A. Matveev, "Resonant Josephson current through Kondo impurities in a tunnel barrier", JETP Letters **49**, 659 (1989), [Pis'ma Zh. Eksp. Teor. Fiz. **49**, 570 (1989)].

[7] B. I. Spivak and S. A. Kivelson, "Negative local superfluid densities: the difference between dirty superconductors and dirty Bose liquids", Physical Review B **43**, 3740 (1991) 10.1103/PhysRevB.43.3740.

[8] A. V. Rozhkov and D. P. Arovas, "Josephson coupling through a magnetic impurity", Physical Review Letters **82**, 2788 (1999) 10.1103/PhysRevLett.82.2788, arXiv:cond-mat/9812085.

[9] E. Vecino, A. Martín-Rodero, and A. Levy Yeyati, "Josephson current through a correlated quantum level: Andreev states and π junction behavior", Physical Review B **68**, 035105 (2003) 10.1103/PhysRevB.68.035105, arXiv:cond-mat/0212375.

[10] M.-S. Choi, M. Lee, K. Kang, and W. Belzig, "Kondo effect and Josephson current through a quantum dot between two superconductors", Physical Review B **70**, 020502 (2004) 10.1103/PhysRevB.70.020502, arXiv:cond-mat/0312271.

[11] F. Siano and R. Egger, "Josephson current through a nanoscale magnetic quantum dot", Physical Review Letters **93**, 047002 (2004) 10.1103/PhysRevLett.93.047002, arXiv:cond-mat/0405670.

[12] J. Bauer, A. Oguri, and A. C. Hewson, "Spectral properties of locally correlated electrons in a Bardeen–Cooper–Schrieffer superconductor", Journal of Physics: Condensed Matter **19**, 486211 (2007) 10.1088/0953-8984/19/48/486211, arXiv:0707.4368 [cond-mat.str-el].

[13] C. Karrasch, A. Oguri, and V. Meden, "Josephson current through a single Anderson impurity coupled to BCS leads", Physical Review B **77**, 024517 (2008) 10.1103/PhysRevB.77.024517, arXiv:0711.0671 [cond-mat.str-el].

[14] T. Meng, S. Florens, and P. Simon, "Self-consistent description of Andreev bound states in Josephson quantum dot devices", Physical Review B **79**, 224521 (2009) 10.1103/PhysRevB.79.224521, arXiv:0902.1111 [cond-mat.str-el].

[15] S. De Franceschi, L. Kouwenhoven, C. Schönenberger, and W. Wernsdorfer, "Hybrid superconductor–quantum dot devices", Nature Nanotechnology **5**, 703 (2010) 10.1038/nnano.2010.173.

[16] A. Martín-Rodero and A. Levy Yeyati, "Josephson and Andreev transport through quantum dots", Advances in Physics **60**, 899 (2011) 10.1080/00018732.2011.624266, arXiv:1111.4939 [cond-mat.mes-hall].

[17] V. Meden, "The Anderson–Josephson quantum dot—a theory perspective", Journal of Physics: Condensed Matter **31**, 163001 (2019) 10.1088/1361-648X/aafd6a, arXiv:1810.02181 [cond-mat.mes-hall].

[18] E. Prada, P. San-Jose, M. W. A. de Moor, et al., "From Andreev to Majorana bound states in hybrid superconductor–semiconductor nanowires", Nature Reviews Physics **2**, 575 (2020) 10.1038/s42254-020-0228-y, arXiv:1911.04512 [cond-mat.supr-con].

[19] J. A. van Dam, Y. V. Nazarov, E. P. A. M. Bakkers, et al., "Supercurrent reversal in quantum dots", Nature **442**, 667 (2006) 10.1038/nature05018, arXiv:cond-mat/0609723.

[20] J.-P. Cleuziou, W. Wernsdorfer, V. Bouchiat, et al., "Carbon nanotube superconducting quantum interference device", Nature Nanotechnology **1**, 53 (2006) 10.1038/nnano.2006.54.

[21] J.-D. Pillet, C. H. L. Quay, P. Morfin, et al., "Andreev bound states in supercurrent-carrying carbon nanotubes revealed", Nature Physics **6**, 965 (2010) 10.1038/nphys1811, arXiv:1005.0443 [cond-mat.mes-hall].

[22] R. S. Deacon, Y. Tanaka, A. Oiwa, et al., "Tunneling spectroscopy of Andreev energy levels in a quantum dot coupled to a superconductor", Physical Review Letters **104**, 076805 (2010) 10.1103/PhysRevLett.104.076805.

[23] E. J. H. Lee, X. Jiang, M. Houzet, et al., "Spin-resolved Andreev levels and parity crossings in hybrid superconductor–semiconductor nanostructures", Nature Nanotechnology **9**, 79 (2014) 10.1038/nnano.2013.267, arXiv:1302.2611 [cond-mat.mes-hall].

[24] R. Delagrange, D. J. Luitz, R. Weil, et al., "Manipulating the magnetic state of a carbon nanotube Josephson junction using the superconducting phase", Physical Review B **91**, 241401 (2015) 10.1103/PhysRevB.91.241401, arXiv:1501.03357 [cond-mat.mes-hall].

[25] A. Bargerbos, M. Pita-Vidal, R. Žitko, et al., "Singlet-doublet transitions of a quantum dot Josephson junction detected in a transmon circuit", PRX Quantum **3**, 030311 (2022) 10.1103/PRXQuantum.3.030311, arXiv:2202.12754 [cond-mat.mes-hall].

[26] A. Yazdani, B. A. Jones, C. P. Lutz, et al., "Probing the local effects of magnetic impurities on superconductivity", Science **275**, 1767 (1997) 10.1126/science.275.5307.1767.

[27] K. J. Franke, G. Schulze, and J. I. Pascual, "Competition of superconducting phenomena and Kondo screening at the nanoscale", Science **332**, 940 (2011) 10.1126/science.1202204.

[28] M. Ruby, F. Pientka, Y. Peng, et al., "Tunneling processes into localized subgap states in superconductors", Physical Review Letters **115**, 087001 (2015) 10.1103/PhysRevLett.115.087001, arXiv:1502.05048 [cond-mat.mes-hall].

[29] B. W. Heinrich, J. I. Pascual, and K. J. Franke, "Single magnetic adsorbates on *s*-wave superconductors", Progress in Surface Science **93**, 1 (2018) 10.1016/j.progsurf.2018.01.001, arXiv:1705.03672 [cond-mat.mes-hall].

[30] L. Bretheau, Ç. Ö. Girit, H. Pothier, et al., "Exciting Andreev pairs in a superconducting atomic contact", Nature **499**, 312 (2013) 10.1038/nature12315, arXiv:1305.4091 [cond-mat.mes-hall].

[31] L. Bretheau, Ç. Ö. Girit, C. Urbina, et al., "Supercurrent spectroscopy of Andreev states", Physical Review X **3**, 041034 (2013) 10.1103/PhysRevX.3.041034, arXiv:1311.3540 [cond-mat.mes-hall].

[32] C. Janvier, L. Tosi, L. Bretheau, et al., "Coherent manipulation of Andreev states in superconducting atomic contacts", Science **349**, 1199 (2015) 10.1126/science.aab2179, arXiv:1509.03961 [cond-mat.mes-hall].

[33] D. J. van Woerkom, A. Proutski, B. van Heck, et al., "Microwave spectroscopy of spinful Andreev bound states in ballistic semiconductor Josephson junctions", Nature Physics **13**, 876 (2017) 10.1038/nphys4150, arXiv:1609.00333 [cond-mat.mes-hall].

[34] M. Hays, G. de Lange, K. Serniak, et al., "Direct microwave measurement of Andreev-bound-state dynamics in a semiconductor-nanowire Josephson junction", Physical Review Letters **121**, 047001 (2018) 10.1103/PhysRevLett.121.047001, arXiv:1711.01645 [cond-mat.supr-con].

[35] M. A. Despósito and A. Levy Yeyati, "Controlled dephasing of Andreev states in superconducting quantum point contacts", Physical Review B **64**, 140511 (2001) 10.1103/PhysRevB.64.140511, arXiv:cond-mat/0108351.

[36] A. Zazunov, V. S. Shumeiko, E. N. Bratus', et al., "Andreev level qubit", Physical Review Letters **90**, 087003 (2003) 10.1103/PhysRevLett.90.087003, arXiv:cond-mat/0206342.

[37] N. M. Chtchelkatchev and Y. V. Nazarov, "Andreev quantum dots for spin manipulation", Physical Review Letters **90**, 226806 (2003) 10.1103/PhysRevLett.90.226806, arXiv:cond-mat/0207684.

[38] C. Padurariu and Y. V. Nazarov, "Theoretical proposal for superconducting spin qubits", Physical Review B **81**, 144519 (2010) 10.1103/PhysRevB.81.144519, arXiv:0912.3910 [cond-mat.mes-hall].

[39] M. Hays, V. Fatemi, D. Bouman, et al., "Coherent manipulation of an Andreev spin qubit", Science **373**, 430 (2021) 10.1126/science.abf0345, arXiv:2101.06701 [cond-mat.mes-hall].

[40] M. Pita-Vidal, A. Bargerbos, R. Žitko, et al., "Direct manipulation of a superconducting spin qubit strongly coupled to a transmon qubit", Nature Physics **19**, 1110 (2023) 10.1038/s41567-023-02071-x, arXiv:2208.10094 [quant-ph].

[41] L. Tosi, C. Metzger, M. F. Goffman, et al., "Spin-orbit splitting of Andreev states revealed by microwave spectroscopy", Physical Review X **9**, 011010 (2019) 10.1103/PhysRevX.9.011010, arXiv:1810.02591 [cond-mat.mes-hall].

[42] F. J. Matute-Cañadas, C. Metzger, S. Park, et al., "Signatures of interactions in the Andreev spectrum of nanowire Josephson junctions", Physical Review Letters **128**, 197702 (2022) 10.1103/PhysRevLett.128.197702, arXiv:2112.05625 [cond-mat.mes-hall].

[43] V. Fatemi, P. D. Kurilovich, M. Hays, et al., "Microwave susceptibility observation of interacting many-body Andreev states", Physical Review Letters **129**, 227701 (2022) 10.1103/PhysRevLett.129.227701, arXiv:2112.05624 [cond-mat.mes-hall].

[44] A. Bargerbos, M. Pita-Vidal, R. Žitko, et al., "Spectroscopy of spin-split Andreev levels in a quantum dot with superconducting leads", Physical Review Letters **131**, 097001 (2023) 10.1103/PhysRevLett.131.097001, arXiv:2208.09314 [cond-mat.mes-hall].

[45] J. J. Wesdorp, L. Grünhaupt, A. Vaartjes, et al., "Dynamical polarization of the fermion parity in a nanowire Josephson junction", Physical Review Letters **131**, 117001 (2023) 10.1103/PhysRevLett.131.117001, arXiv:2112.01936 [cond-mat.mes-hall].

[46] S. Park, W. Lee, S. Jang, et al., "Steady Floquet–Andreev states in graphene Josephson junctions", Nature **603**, 421 (2022) 10.1038/s41586-021-04364-8, arXiv:2105.00592 [cond-mat.mes-hall].

[47] P. Kot, R. Drost, M. Uhl, et al., "Microwave-assisted tunneling and interference effects in superconducting junctions under fast driving signals", Physical Review B **101**, 134507 (2020) 10.1103/PhysRevB.101.134507, arXiv:2001.08228 [cond-mat.supr-con].

[48] O. Peters, N. Bogdanoff, S. Acero González, et al., "Resonant Andreev reflections probed by photon-assisted tunnelling at the atomic scale", Nature Physics **16**, 1222 (2020) 10.1038/s41567-020-0972-z, arXiv:2001.09534 [cond-mat.mes-hall].

[49] S. A. González, L. Melischek, O. Peters, et al., "Photon-assisted resonant Andreev reflections: Yu-Shiba-Rusinov and Majorana states", Physical Review B **102**, 045413 (2020) 10.1103/PhysRevB.102.045413, arXiv:2102.04726 [cond-mat.mes-hall].

[50] N. Goldman and J. Dalibard, "Periodically driven quantum systems: effective Hamiltonians and engineered gauge fields", Physical Review X **4**, 031027 (2014) 10.1103/PhysRevX.4.031027, arXiv:1404.4373.

[51] M. Bukov, L. D'Alessio, and A. Polkovnikov, "Universal high-frequency behavior of periodically driven systems: from dynamical stabilization to Floquet engineering", Advances in Physics **64**, 139 (2015) 10.1080/00018732.2015.1055918, arXiv:1407.4803.

[52] A. Eckardt, "Colloquium: atomic quantum gases in periodically driven optical lattices", Reviews of Modern Physics **89**, 011004 (2017) 10.1103/RevModPhys.89.011004, arXiv:1606.08041.

[53] T. Oka and S. Kitamura, "Floquet engineering of quantum materials", Annual Review of Condensed Matter Physics **10**, 387 (2019) 10.1146/annurev-conmatphys-031218-013423, arXiv:1804.03212.

[54] M. S. Rudner and N. H. Lindner, "Band structure engineering and non-equilibrium dynamics in Floquet topological insulators", Nature Reviews Physics **2**, 229 (2020) 10.1038/s42254-020-0170-z, arXiv:1909.02008.

[55] C. W. J. Beenakker and H. van Houten, "Josephson current through a superconducting quantum point contact shorter than the coherence length", Physical Review Letters **66**, 3056 (1991) 10.1103/PhysRevLett.66.3056.

[56] C. W. J. Beenakker, "Universal limit of critical-current fluctuations in mesoscopic Josephson junctions", Physical Review Letters **67**, 3836 (1991) 10.1103/PhysRevLett.67.3836.

[57] R. Aguado, "A perspective on semiconductor-based superconducting qubits", Applied Physics Letters **117**, 240501 (2020) 10.1063/5.0024124, arXiv:2010.13775 [cond-mat.supr-con].

[58] L. I. Glazman and G. Catelani, "Bogoliubov quasiparticles in superconducting qubits", SciPost Physics Lecture Notes, 31 (2021) 10.21468/SciPostPhysLectNotes.31, arXiv:2003.04366.

[59] V. V. Baran, E. J. P. Frost, and J. Paaske, "Surrogate model solver for impurity-induced superconducting subgap states", Physical Review B **108**, L220506 (2023) 10.1103/PhysRevB.108.L220506, arXiv:2307.11646 [cond-mat.supr-con].

[60] D. Bobok, L. Frk, V. Pokorný, and M. Žonda, "Scalable effective models for superconducting nanostructures: applications to double, triple, and quadruple quantum dots", Physical Review B **112**, 205418 (2025) 10.1103/mxsl-fc96.

[61] M. Žonda, P. Zalom, T. Novotný, et al., "Generalized atomic limit of a double quantum dot coupled to superconducting leads", Physical Review B **107**, 115407 (2023) 10.1103/physrevb.107.115407.

[62] A. C. Hewson, *The Kondo problem to heavy fermions*, Cambridge Studies in Magnetism 2 (Cambridge University Press, Cambridge, 1993), 10.1017/CBO9780511470752.

[63] R. Bulla, T. A. Costi, and T. Pruschke, "Numerical renormalization group method for quantum impurity systems", Reviews of Modern Physics **80**, 395 (2008) 10.1103/RevModPhys.80.395, arXiv:cond-mat/0701105.

[64] R. Žitko, "Superconducting quantum dot and the sub-gap states", in Spintronics xi, Vol. 10732, Proceedings of SPIE (2018), 107321N, 10.1117/12.2322365, arXiv:1901.01039.

[65] L. Pavešić, M. Pita-Vidal, A. Bargerbos, and R. Žitko, "Impurity Knight shift in quantum dot Josephson junctions", SciPost Physics **15**, 070 (2023) 10.21468/SciPostPhys.15.2.070, arXiv:2212.07185 [cond-mat.mes-hall].

[66] C. Metzger, S. Park, L. Tosi, et al., "Circuit-QED with phase-biased Josephson weak links", Physical Review Research **3**, 013036 (2021) 10.1103/PhysRevResearch.3.013036, arXiv:2010.00430 [cond-mat.mes-hall].

[67] E. Scheer, N. Agraït, J. C. Cuevas, et al., "The signature of chemical valence in the electrical conduction through a single-atom contact", Nature **394**, 154 (1998) 10.1038/28112.

[68] V. Chidambaram, A. Kringhøj, L. Casparis, et al., "Microwave sensing of Andreev bound states in a gate-defined superconducting quantum point contact", Physical Review Research **4**, 023170 (2022) 10.1103/PhysRevResearch.4.023170, arXiv:2102.05206 [cond-mat.mes-hall].

[69] M. Hays, V. Fatemi, K. Serniak, et al., "Continuous monitoring of a trapped superconducting spin", Nature Physics **16**, 1103 (2020) 10.1038/s41567-020-0952-3, arXiv:1908.02800 [cond-mat.mes-hall].

[70] K. G. Wilson, "The renormalization group: critical phenomena and the Kondo problem", Reviews of Modern Physics **47**, 773 (1975) 10.1103/RevModPhys.47.773.

[71] E. Gull, A. J. Millis, A. I. Lichtenstein, et al., "Continuous-time Monte Carlo methods for quantum impurity models", Reviews of Modern Physics **83**, 349 (2011) 10.1103/RevModPhys.83.349, arXiv:1012.4474.

[72] T. Iličin and R. Žitko, "Variational solution of the superconducting Anderson impurity model and the band-edge singularity phenomena", SciPost Physics **19**, 006 (2025) 10.21468/SciPostPhys.19.1.006, arXiv:2503.18902 [cond-mat.supr-con].

[73] T. Iličin and R. Žitko, "Effects of electron-electron interaction and spin-orbit coupling on Andreev pair qubits in quantum dot Josephson junctions", SciPost Physics **20**, 147 (2026) 10.21468/SciPostPhys.20.5.147, arXiv:2512.23015 [cond-mat.mes-hall].

[74] S. R. White, "Density matrix formulation for quantum renormalization groups", Physical Review Letters **69**, 2863 (1992) 10.1103/physrevlett.69.2863.

[75] U. Schollwöck, "The density-matrix renormalization group in the age of matrix product states", Annals of Physics **326**, 96 (2011) 10.1016/j.aop.2010.09.012.

[76] J. Hauschild and F. Pollmann, "Efficient numerical simulations with Tensor Networks: Tensor network Python (TeNPy)", SciPost Physics Lecture Notes, 5 (2018) 10.21468/scipostphyslectnotes.5.

[77] M. Grifoni and P. Hänggi, "Driven quantum tunneling", Physics Reports **304**, 229 (1998) 10.1016/S0370-1573(98)00022-2.

[78] S. Kohler, J. Lehmann, and P. Hänggi, "Driven quantum transport on the nanoscale", Physics Reports **406**, 379 (2005) 10.1016/j.physrep.2004.11.002, arXiv:cond-mat/0409251.

[79] S.-I. Chu and D. A. Telnov, "Beyond the Floquet theorem: generalized Floquet formalisms and quasienergy methods for atomic and molecular multiphoton processes in intense laser fields", Physics Reports **390**, 1 (2004) 10.1016/j.physrep.2003.10.001.

[80] M. Holthaus, "Floquet engineering with quasienergy bands of periodically driven optical lattices", Journal of Physics B: Atomic, Molecular and Optical Physics **49**, 013001 (2016) 10.1088/0953-4075/49/1/013001, arXiv:1510.09042.

[81] G. Floquet, "Sur les équations différentielles linéaires à coefficients périodiques", Annales scientifiques de l'École Normale Supérieure **12**, 47 (1883) 10.24033/asens.220.

[82] J. H. Shirley, "Solution of the Schrödinger equation with a Hamiltonian periodic in time", Physical Review **138**, B979 (1965) 10.1103/PhysRev.138.B979.

[83] Ya. B. Zel'dovich, "The quasienergy of a quantum-mechanical system subjected to a periodic action", Soviet Physics JETP **24**, 1006 (1967), [Zh. Eksp. Teor. Fiz. **51**, 1492 (1966)].

[84] V. I. Ritus, "Shift and splitting of atomic energy levels by the field of an electromagnetic wave", Soviet Physics JETP **24**, 1041 (1967), [Zh. Eksp. Teor. Fiz. **51**, 1544 (1966)].

[85] A. Eckardt and E. Anisimovas, "High-frequency approximation for periodically driven quantum systems from a Floquet-space perspective", New Journal of Physics **17**, 093039 (2015) 10.1088/1367-2630/17/9/093039, arXiv:1502.06477.

[86] H. Sambe, "Steady states and quasienergies of a quantum-mechanical system in an oscillating field", Physical Review A **7**, 2203 (1973) 10.1103/PhysRevA.7.2203.

[87] C. Cohen-Tannoudji and S. Reynaud, "Dressed-atom description of resonance fluorescence and absorption spectra of a multi-level atom in an intense laser beam", Journal of Physics B: Atomic and Molecular Physics **10**, 345 (1977) 10.1088/0022-3700/10/3/005.

[88] C. Cohen-Tannoudji, J. Dupont-Roc, and G. Grynberg, *Atom–photon interactions, Basic processes and applications* (Wiley, New York, 1992), 10.1002/9783527617197, Paperback edition 1998.

[89] S. H. Autler and C. H. Townes, "Stark effect in rapidly varying fields", Physical Review **100**, 703 (1955) 10.1103/PhysRev.100.703.

[90] I. I. Rabi, "Space quantization in a gyrating magnetic field", Physical Review **51**, 652 (1937) 10.1103/PhysRev.51.652.

[91] F. Bloch and A. Siegert, "Magnetic resonance for nonrotating fields", Physical Review **57**, 522 (1940) 10.1103/PhysRev.57.522.

[92] H. P. Breuer and M. Holthaus, "Adiabatic processes in the ionization of highly excited hydrogen atoms", Zeitschrift für Physik D **11**, 1 (1989) 10.1007/bf01436579.

[93] K. Drese and M. Holthaus, "Floquet theory for short laser pulses", The European Physical Journal D **5**, 119 (1999) 10.1007/s100530050236.

[94] W. Magnus, "On the exponential solution of differential equations for a linear operator", Communications on Pure and Applied Mathematics **7**, 649 (1954) 10.1002/cpa.3160070404.

[95] M. M. Maricq, "Application of average Hamiltonian theory to the NMR of solids", Physical Review B **25**, 6622 (1982) 10.1103/PhysRevB.25.6622.

[96] S. Rahav, I. Gilary, and S. Fishman, "Effective Hamiltonians for periodically driven systems", Physical Review A **68**, 013820 (2003) 10.1103/PhysRevA.68.013820, arXiv:nlin/0301033.

[97] T. Mikami, S. Kitamura, K. Yasuda, et al., "Brillouin-Wigner theory for high-frequency expansion in periodically driven systems: application to Floquet topological insulators", Physical Review B **93**, 144307 (2016) 10.1103/PhysRevB.93.144307, arXiv:1511.00755.

[98] F. Grossmann, T. Dittrich, P. Jung, and P. Hänggi, "Coherent destruction of tunneling", Physical Review Letters **67**, 516 (1991) 10.1103/PhysRevLett.67.516.

[99] D. H. Dunlap and V. M. Kenkre, "Dynamic localization of a charged particle moving under the influence of an electric field", Physical Review B **34**, 3625 (1986) 10.1103/PhysRevB.34.3625.

[100] S. N. Shevchenko, S. Ashhab, and F. Nori, "Landau–Zener–Stückelberg interferometry", Physics Reports **492**, 1 (2010) 10.1016/j.physrep.2010.03.002, arXiv:0911.1917.

[101] W. D. Oliver, Y. Yu, J. C. Lee, et al., "Mach-Zehnder interferometry in a strongly driven superconducting qubit", Science **310**, 1653 (2005) 10.1126/science.1119678, arXiv:cond-mat/0512691.

[102] M. Sillanpää, T. Lehtinen, A. Paila, et al., "Continuous-time monitoring of Landau-Zener interference in a Cooper-pair box", Physical Review Letters **96**, 187002 (2006) 10.1103/PhysRevLett.96.187002, arXiv:cond-mat/0510559.

[103] O. V. Ivakhnenko, S. N. Shevchenko, and F. Nori, "Nonadiabatic Landau–Zener–Stückelberg–Majorana transitions, dynamics, and interference", Physics Reports **995**, 1 (2023) 10.1016/j.physrep.2022.10.002, arXiv:2203.16348.

[104] N. Moiseyev, *Non-Hermitian quantum mechanics* (Cambridge University Press, Cambridge, 2011), 10.1017/CBO9780511976186.

[105] D. W. Hone, R. Ketzmerick, and W. Kohn, "Time-dependent Floquet theory and absence of an adiabatic limit", Physical Review A **56**, 4045 (1997) 10.1103/PhysRevA.56.4045, arXiv:cond-mat/9706182.

[106] D. W. Hone, R. Ketzmerick, and W. Kohn, "Statistical mechanics of Floquet systems: the pervasive problem of near degeneracies", Physical Review E **79**, 051129 (2009) 10.1103/PhysRevE.79.051129, arXiv:0811.3243.

[107] R. Blümel, A. Buchleitner, R. Graham, et al., "Dynamical localization in the microwave interaction of Rydberg atoms: the influence of noise", Physical Review A **44**, 4521 (1991) 10.1103/PhysRevA.44.4521.

[108] S. Kohler, T. Dittrich, and P. Hänggi, "Floquet-Markovian description of the parametrically driven, dissipative harmonic quantum oscillator", Physical Review E **55**, 300 (1997) 10.1103/PhysRevE.55.300, arXiv:quant-ph/9809088.

[109] H.-P. Breuer and F. Petruccione, *The theory of open quantum systems* (Oxford University Press, Oxford, 2007), 10.1093/acprof:oso/9780199213900.001.0001, First published 2002.

[110] L. P. Kouwenhoven, S. Jauhar, K. McCormick, et al., "Photon-assisted tunneling through a quantum dot", Physical Review B **50**, 2019 (1994) 10.1103/PhysRevB.50.2019.

[111] L. P. Kouwenhoven, S. Jauhar, J. Orenstein, et al., "Observation of photon-assisted tunneling through a quantum dot", Physical Review Letters **73**, 3443 (1994) 10.1103/PhysRevLett.73.3443.

[112] T. H. Oosterkamp, T. Fujisawa, W. G. van der Wiel, et al., "Microwave spectroscopy of a quantum-dot molecule", Nature **395**, 873 (1998) 10.1038/27617.

[113] G. Platero and R. Aguado, "Photon-assisted transport in semiconductor nanostructures", Physics Reports **395**, 1 (2004) 10.1016/j.physrep.2004.01.004, arXiv:cond-mat/0311001.

[114] F. Kos, S. E. Nigg, and L. I. Glazman, "Frequency-dependent admittance of a short superconducting weak link", Physical Review B **87**, 174521 (2013) 10.1103/PhysRevB.87.174521, arXiv:1303.2918 [cond-mat.supr-con].

[115] A. G. Moghaddam, M. Governale, and J. König, "Driven superconducting proximity effect in interacting quantum dots", Physical Review B **85**, 094518 (2012) 10.1103/PhysRevB.85.094518, arXiv:1201.5032 [cond-mat.mes-hall].

[116] F. H. L. Koppens, C. Buizert, K. J. Tielrooij, et al., "Driven coherent oscillations of a single electron spin in a quantum dot", Nature **442**, 766 (2006) 10.1038/nature05065, arXiv:cond-mat/0608459.

[117] S. Baumann, W. Paul, T. Choi, et al., "Electron paramagnetic resonance of individual atoms on a surface", Science **350**, 417 (2015) 10.1126/science.aac8703.

[118] K. Yang, W. Paul, S.-H. Phark, et al., "Coherent spin manipulation of individual atoms on a surface", Science **366**, 509 (2019) 10.1126/science.aay6779.

[119] D. Averin and A. Bardas, "Ac Josephson effect in a single quantum channel", Physical Review Letters **75**, 1831 (1995) 10.1103/PhysRevLett.75.1831, arXiv:cond-mat/9505096.

[120] E. N. Bratus', V. S. Shumeiko, and G. Wendin, "Theory of subharmonic gap structure in superconducting mesoscopic tunnel contacts", Physical Review Letters **74**, 2110 (1995) 10.1103/PhysRevLett.74.2110.

[121] J. C. Cuevas, A. Martín-Rodero, and A. Levy Yeyati, "Hamiltonian approach to the transport properties of superconducting quantum point contacts", Physical Review B **54**, 7366 (1996) 10.1103/PhysRevB.54.7366, arXiv:cond-mat/9605023.

[122] J. C. Cuevas, J. Heurich, A. Martín-Rodero, et al., "Subharmonic Shapiro steps and assisted tunneling in superconducting point contacts", Physical Review Letters **88**, 157001 (2002) 10.1103/PhysRevLett.88.157001, arXiv:cond-mat/0109152.

[123] F. W. J. Olver, A. B. Olde Daalhuis, D. W. Lozier, et al., eds., *NIST digital library of mathematical functions*, version Release 1.2.8 of 2026-09-15, §10.12, Generating function and associated series (Jacobi–Anger expansion), Eq. 10.12.1, (2026) https://dlmf.nist.gov/10.12.

[124] R. B. Lehoucq, D. C. Sorensen, and C. Yang, *ARPACK users' guide, Solution of large-scale eigenvalue problems with implicitly restarted Arnoldi methods* (Society for Industrial and Applied Mathematics, Philadelphia, 1998), 10.1137/1.9780898719628.

[125] X. S. Li, "An overview of SuperLU", ACM Transactions on Mathematical Software **31**, 302 (2005) 10.1145/1089014.1089017.

[126] S. Blanes and P. C. Moan, "Fourth- and sixth-order commutator-free Magnus integrators for linear and non-linear dynamical systems", Applied Numerical Mathematics **56**, 1519 (2006) 10.1016/j.apnum.2005.11.004.

[127] A. Alvermann and H. Fehske, "High-order commutator-free exponential time-propagation of driven quantum systems", Journal of Computational Physics **230**, 5930 (2011) 10.1016/j.jcp.2011.04.006, arXiv:1102.5071.

[128] S. Blanes, F. Casas, J. A. Oteo, and J. Ros, "The Magnus expansion and some of its applications", Physics Reports **470**, 151 (2009) 10.1016/j.physrep.2008.11.001, arXiv:0810.5488.

[129] J. R. Johansson, P. D. Nation, and F. Nori, "QuTiP: an open-source Python framework for the dynamics of open quantum systems", Computer Physics Communications **183**, 1760 (2012) 10.1016/j.cpc.2012.02.021, arXiv:1110.0573.

[130] N. Lambert, E. Giguère, P. Menczel, et al., "QuTiP 5: the quantum toolbox in Python", Physics Reports **1153**, 1 (2026) 10.1016/j.physrep.2025.10.001, arXiv:2412.04705.

[131] B. R. Mollow, "Power spectrum of light scattered by two-level systems", Physical Review **188**, 1969 (1969) 10.1103/PhysRev.188.1969.

[132] B. R. Mollow, "Stimulated emission and absorption near resonance for driven systems", Physical Review A **5**, 2217 (1972) 10.1103/PhysRevA.5.2217.

[133] F. Y. Wu, S. Ezekiel, M. Ducloy, and B. R. Mollow, "Observation of amplification in a strongly driven two-level atomic system at optical frequencies", Physical Review Letters **38**, 1077 (1977) 10.1103/PhysRevLett.38.1077.

[134] M. Baur, S. Filipp, R. Bianchetti, et al., "Measurement of Autler-Townes and Mollow transitions in a strongly driven superconducting qubit", Physical Review Letters **102**, 243602 (2009) 10.1103/PhysRevLett.102.243602.

[135] P. K. Tien and J. P. Gordon, "Multiphoton process observed in the interaction of microwave fields with the tunneling between superconductor films", Physical Review **129**, 647 (1963) 10.1103/PhysRev.129.647.

[136] A. H. Dayem and R. J. Martin, "Quantum interaction of microwave radiation with tunneling between superconductors", Physical Review Letters **8**, 246 (1962) 10.1103/PhysRevLett.8.246.

[137] Y. Nakamura, Y. A. Pashkin, and J. S. Tsai, "Coherent control of macroscopic quantum states in a single-Cooper-pair box", Nature **398**, 786 (1999) 10.1038/19718, arXiv:cond-mat/9904003.

[138] Y. Nakamura, Yu. A. Pashkin, and J. S. Tsai, "Rabi oscillations in a Josephson-junction charge two-level system", Physical Review Letters **87**, 246601 (2001) 10.1103/PhysRevLett.87.246601.

[139] F. Großmann and P. Hänggi, "Localization in a driven two-level dynamics", Europhysics Letters **18**, 571 (1992) 10.1209/0295-5075/18/7/001.

[140] J. Stehlik, Y. Dovzhenko, J. R. Petta, et al., "Landau-Zener-Stückelberg interferometry of a single electron charge qubit", Physical Review B **86**, 121303 (2012) 10.1103/PhysRevB.86.121303, arXiv:1205.6173.

[141] M. Holthaus, "Collapse of minibands in far-infrared irradiated superlattices", Physical Review Letters **69**, 351 (1992) 10.1103/PhysRevLett.69.351.

[142] H. Lignier, C. Sias, D. Ciampini, et al., "Dynamical control of matter-wave tunneling in periodic potentials", Physical Review Letters **99**, 220403 (2007) 10.1103/PhysRevLett.99.220403, arXiv:0707.0403.

[143] Y. Kayanuma, "Role of phase coherence in the transition dynamics of a periodically driven two-level system", Physical Review A **50**, 843 (1994) 10.1103/PhysRevA.50.843.

[144] D. G. Olivares, A. Levy Yeyati, L. Bretheau, et al., "Dynamics of quasiparticle trapping in Andreev levels", Physical Review B **89**, 104504 (2014) 10.1103/PhysRevB.89.104504, arXiv:1309.7283 [cond-mat.mes-hall].

[145] S. Park, C. Metzger, L. Tosi, et al., "From adiabatic to dispersive readout of quantum circuits", Physical Review Letters **125**, 077701 (2020) 10.1103/PhysRevLett.125.077701, arXiv:2007.05030 [cond-mat.mes-hall].

[146] P. D. Kurilovich, V. D. Kurilovich, V. Fatemi, et al., "Microwave response of an Andreev bound state", Physical Review B **104**, 174517 (2021) 10.1103/PhysRevB.104.174517, arXiv:2106.00028 [cond-mat.mes-hall].

[147] C. Hermansen, A. Levy Yeyati, and J. Paaske, "Inductive microwave response of Yu-Shiba-Rusinov states", Physical Review B **105**, 054503 (2022) 10.1103/PhysRevB.105.054503, arXiv:2112.11261 [cond-mat.mes-hall].

[148] M. Zgirski, L. Bretheau, Q. Le Masne, et al., "Evidence for long-lived quasiparticles trapped in superconducting point contacts", Physical Review Letters **106**, 257003 (2011) 10.1103/PhysRevLett.106.257003, arXiv:1105.5039 [cond-mat.mes-hall].

[149] R.-P. Riwar, M. Houzet, J. S. Meyer, and Y. V. Nazarov, "Control of Andreev bound state population and related charge-imbalance effect", Journal of Physics: Condensed Matter **27**, 095701 (2015) 10.1088/0953-8984/27/9/095701, arXiv:1407.0534 [cond-mat.supr-con].

[150] L. Peralta Gavensky, G. Usaj, D. Feinberg, and C. A. Balseiro, "Berry curvature tomography and realization of topological Haldane model in driven three-terminal Josephson junctions", Physical Review B **97**, 220505 (2018) 10.1103/PhysRevB.97.220505, arXiv:1804.04755 [cond-mat.mes-hall].

[151] B. Venitucci, D. Feinberg, R. Mélin, and B. Douçot, "Nonadiabatic Josephson current pumping by chiral microwave irradiation", Physical Review B **97**, 195423 (2018) 10.1103/PhysRevB.97.195423, arXiv:1708.03262 [cond-mat.mes-hall].

[152] R. Mélin, R. Danneau, K. Yang, et al., "Engineering the Floquet spectrum of superconducting multiterminal quantum dots", Physical Review B **100**, 035450 (2019) 10.1103/PhysRevB.100.035450, arXiv:1903.04889 [cond-mat.mes-hall].

[153] A. Keliri and B. Douçot, "Driven Andreev molecule", Physical Review B **107**, 094505 (2023) 10.1103/PhysRevB.107.094505, arXiv:2208.11541 [cond-mat.mes-hall].

[154] C. Ortega-Taberner, A.-P. Jauho, and J. Paaske, "Anomalous Josephson current through a driven double quantum dot", Physical Review B **107**, 115165 (2023) 10.1103/PhysRevB.107.115165, arXiv:2207.06152 [cond-mat.mes-hall].

[155] J. R. Petta, A. C. Johnson, C. M. Marcus, et al., "Manipulation of a single charge in a double quantum dot", Physical Review Letters **93**, 186802 (2004) 10.1103/PhysRevLett.93.186802, arXiv:cond-mat/0408139.

[156] M. R. Sahu, F. J. Matute-Cañadas, M. Benito, et al., "Ground-state phase diagram and parity-flipping microwave transitions in a gate-tunable Josephson junction", Physical Review B **109**, 134506 (2024) 10.1103/PhysRevB.109.134506, arXiv:2312.12914 [cond-mat.mes-hall].

[157] D. Z. Haxell, M. Coraiola, D. Sabonis, et al., "Microwave-induced conductance replicas in hybrid Josephson junctions without Floquet–Andreev states", Nature Communications **14**, 6798 (2023) 10.1038/s41467-023-42357-5, arXiv:2212.03554 [cond-mat.mes-hall].

[158] K. C. Nowack, F. H. L. Koppens, Y. V. Nazarov, and L. M. K. Vandersypen, "Coherent control of a single electron spin with electric fields", Science **318**, 1430 (2007) 10.1126/science.1148092, arXiv:0707.3080 [cond-mat.mes-hall].

[159] V. N. Golovach, M. Borhani, and D. Loss, "Electric-dipole-induced spin resonance in quantum dots", Physical Review B **74**, 165319 (2006) 10.1103/PhysRevB.74.165319, arXiv:cond-mat/0601674.

[160] P. Willke, W. Paul, F. D. Natterer, et al., "Probing quantum coherence in single-atom electron spin resonance", Science Advances **4**, eaaq1543 (2018) 10.1126/sciadv.aaq1543.

[161] S. Park and A. Levy Yeyati, "Andreev spin qubits in multichannel Rashba nanowires", Physical Review B **96**, 125416 (2017) 10.1103/PhysRevB.96.125416, arXiv:1707.04273 [cond-mat.mes-hall].

[162] J. H. Van Vleck, "On σ-type doubling and electron spin in the spectra of diatomic molecules", Physical Review **33**, 467 (1929) 10.1103/PhysRev.33.467.

[163] I. Shavitt and L. T. Redmon, "Quasidegenerate perturbation theories. a canonical van Vleck formalism and its relationship to other approaches", The Journal of Chemical Physics **73**, 5711 (1980) 10.1063/1.440050.

[164] S. Bravyi, D. P. DiVincenzo, and D. Loss, "Schrieffer–Wolff transformation for quantum many-body systems", Annals of Physics **326**, 2793 (2011) 10.1016/j.aop.2011.06.004, arXiv:1105.0675.